universiteit hasselt
KNOWLEDGE IN ACTION

2015 | Faculty of Sciences

DOCTORAL DISSERTATION

Poly(3-alkylthiophene) nanofibers for optoelectronic applications: the case of poly(3-hexylthiophene) nanofiber phototransistors

Doctoral dissertation submitted to obtain the degree of
Doctor of Science: Physics, to be defended by

Wouter Dierckx

Promoter: Prof. Dr Jean Manca | UHasselt
Co-promoter: Prof. Dr Hans-Gerd Boyen | UHasselt

D/2015/2451/01

universiteit hasselt | imec
IMO - IMOMEC
INSTITUUT VOOR MATERIAALONDERZOEK

Chairman	Prof. dr. Karin Coninx, Universiteit Hasselt
Promoter	Prof. dr. Jean Manca, Universiteit Hasselt
Copromoter	Prof. dr. Hans-Gerd Boyen, Universiteit Hasselt
Members of the jury	Prof. dr. Jan D'Haen, Universiteit Hasselt
	Prof. dr. Milos Nesladek, Universiteit Hasselt
	Prof. dr. Wouter Maes, Universiteit Hasselt
	Dr. Wibren D. Oosterbaan
	Dr. Jean-Christophe Bolsée
	Dr. Olivier Douhéret, Materia Nova-Université de Mons

Dankwoord

Het is voorbij, c'est fini, è tutto finite, it's done, es ist vorbei,… en toch kan ik mij nog vlot mijn eerste kennismaking met het toenmalige LUC herinneren. Ik zat in het vijfde middelbaar en we moesten naar het LUC in Diepenbeek voor de fysica olympiade. Diepenbeek, waar ligt dat? Ik dacht dat het wel ergens rond Brussel zou liggen, maar eens we de autosnelweg richting Hasselt opreden, begon ik al sterk te twijfelen. Uiteindelijk eindigde onze autorit ergens in de velden tussen Diepenbeek en Hasselt, want daar bevond zich het LUC. Een kleine universiteit aan de rand van een al even kleine stad, maar met een gezellige aangename sfeer. Ik was meteen verkocht. Een jaar later bij het maken van mijn studiekeuze was er dan ook geen moment van twijfel over de plaats waar ik ging studeren. Terwijl de meesten van mijn klasgenoten naar Leuven trokken, waren er toch nog twee kameraden die ook verkocht waren aan het LUC. Samen hebben we de eerste drie jaar een ongelooflijke tijd beleefd, maar aan alles komt een einde en zodoende trok ik eerst naar Leuven en nadien naar Delft voor mijn masteropleiding. Wat ik echter nooit vergeten ben is hoe aangenaam "den tijd in Djoppenbeek" wel was geweest. Ik was dan ook enorm blij dat ik na mijn masteropleiding kon terugkeren om een doctoraat te beginnen aan het IMO. Hier kwam ik terug in contact met enkele kameraden en bekenden vanuit de bacheloropleiding zodat ik mij vanaf het eerste moment terug thuis voelde. Bedankt Jean om mij deze kans te geven. Thanks for bringing me back "home"!

Een van de eerste nieuwe gezichten die ik leerde kennen op het IMO was Jean-Christophe Bolsée, de AFM specialist. Jean-Christophe was één van de tofste en meest ervaren collega's op het IMO. Van stress en spanning was bij hem geen sprake, want voor elk probleem was er wel een of andere "MacGyver solution". Verder is mij ook altijd het opschrift: "No De-Wever voters!", op de deur van het AFM-lokaal bijgebleven. Jean-Christophe, jij bracht echt een aangename werksfeer op het IMO. Merci! Et aussi merci pour "les attaques de Phil" pendant les plusieurs randonnées à vélo de route que nous avons fait ensemble.

Toen ik ongeveer halfweg mijn doctoraat was, werd Tim Vangerven mijn nieuwe bureaugenoot. Tim is altijd goed gezind en gemotiveerd, en als de zon schijnt, hoor je regelmatig het woord "crèmeke" vallen. Ik kon mij dus geen betere bureaugenoot treffen.

Jeroen, Wim en Matthias, als vroegere bachelorgenoten brachten jullie de nostalgie van deze tijd weer naar boven. Mannen, merci! Tevens ook bedankt aan alle ander doctoraatstudenten, mensen van het secretariaat en het technische personeel om mij te helpen wanneer nodig en de aangename werksfeer er in te houden.

Aangezien ik nooit echt goed was in het schrijven, kon ik de hulp van Wouter Maes en Wibren Oosterbaan bij het nalezen van mijn manuscripten enorm appreciëren. Bedankt Wibren en Wouter, om telkens een snelle en heldere feedback te geven op mijn geschreven werk.

Als laatste wil ik mijn ouders en broer bedanken om mij de rust en ontspanning te geven in tijden van spanning en stress, zoals tijdens de weken dat ik aan het schrijven was. Willem, merci om de kalme helft van onze tweeling te zijn, merci om regelmatig die lont aan mijn kruidvat te doven, als ik weer eens te lang had liggen piekeren over een probleem. Ma en pa, merci om mij altijd te blijven steunen en in mij te geloven.

Wouter

Publications

W. Dierckx, W. D. Oosterbaan, J.-C. Bolsée, W. Maes, D. Vanderzande and J. Manca, *Poly(3-alkylthiophene) nanofibers for optoelectronic devices*, J. Mater. Chem. C, 2014, **2**, 5730.

W. Dierckx, W. D. Oosterbaan, W. Maes, J. C. Bolsée, I. Cardinaletti, J. D'Haen, M. Nesladek and J. Manca, *Organic phototransistors using poly(3-hexylthiophene) nanofibers*, (accepted Nanotechnology).

F. Ouhib, M. Tomassetti, W. Dierckx, P. Verstappen, A. Wisley, A.-S. Duwez, V. Lemaur, R. Lazzaroni, J. Manca, W. Maes, C. Jérôme and C. Detrembleur, *Linear and star-shaped fluoro-isoindigo based donor-acceptor small molecules for organic solar cells*, (submitted to Org. Electron.).

P. Robaeys, F. Bonaccorso, E. Bourgeois, J. D'Haen, W. Dierckx, W. Dexters, D. Spoltore, J. Drijkoningen, J. Liesenborgs, A. Lombardo, A. C. Ferrari, F. Van Reeth, K. Haenen, J. V. Manca and M. Nesladek. *Enhanced performance of polymer:fullerene bulk heterojunction solar cells upon graphene addition.* Appl. Phys. Lett., 2014, **105**, 083306.

T. Vangerven, P. Verstappen, J. Drijkoningen, W. Dierckx, M. Tomasetti, S. Himmelberger, A. Salleo, D. Vanderzande, W. Maes and J. V. Manca, *Effect of molecular weight distribution on trap states in PTB7:PC71BM solar cells*, (to be submitted to Journal of Physical Chemistry C).

Conference contributions

Oral presentations

Wouter Dierckx and Jean Manca, *Polythiophene nanofibers: 1-dimensional highways for electro-optical applications*, International Conference on Semiconducting Materials (ICSM) 2014, 30.06.2014 – 05.07.2014, Turku, Finland.

Table of contents

Nederlandse samenvatting

Ondanks het feit dat met de huidige state-of-the-art siliciumtechnologie erg performante elektronische componenten gefabriceerd kunnen worden, is er toch een stijgende vraag naar alternatieve materialen. Dit komt omdat de productie van silicium-gebaseerde componenten zeer kapitaalsintensief is door de vereisten van een hoog vacuüm en hoge productietemperatuur. Zodoende werd de onderzoekswereld de laatste decennia sterk gestimuleerd om te zoeken naar alternatieve materialen voor het fabriceren van elektronische componenten via goedkopere productiemethodes. Een valabel alternatief voor silicium werd gevonden in de halfgeleidende polymeren. Het voordeel van deze polymeren is dat de depositie ervan vanuit oplossing kan gebeuren via goedkope printtechnieken. Een ander voordeel is dat deze polymeren gecombineerd kunnen worden met lichte, flexibele substraten zodat volledig flexibele en robuste elektronische componenten gemaakt kunnen worden. Om gecommercialiseerd te worden moeten de prestaties van de organische elektronica echter nog fel verbeteren.

Eén van de punten waarop er nog veel verbetering nodig is, is de mobiliteit van de ladingsdragers in deze polymeren en om dit te bewerkstelligen moet de kristalliniteit van de actieve laag verhoogd worden. Dit kan bekomen worden via pre-depositie methodes, door het vormen van gestructureerde kristallijne nanodeeltjes in de polymeeroplossing. Een voorbeeld hiervan is het vormen van nanovezels in een oplossing van poly(3-hexylthiofeen) (P36T). Na depositie zijn deze P36T vezels overwegend parallel geörienteerd met het substraatoppervlak, zodat ze een hoog-kristallijn netwerk van baantjes vormen, ideaal voor het transport van elektrische ladingen in transistors, waarbij richting van de elektrische stroom parallel is aan het substraatoppervlak. Verder beschikken de kristallijne P36T nanovezels in vergelijking met amorf P36T ook nog over een verhoogde absorptie van (zon)licht. In dit onderzoekswerk is het nu de bedoeling om, gebruikmakende van de verhoogde ladingsmobiliteit en verbeterde lichtabsorptie, aan te tonen dat P36T nanovezels uitermate geschikt zijn voor de productie van goedkope

flexibele organische fototransistoren. Dit zijn organische transistoren waarbij de stroom zowel via een aangelegde spanning als via de absorptie van licht kan gecontroleerd worden.

Hoofdstuk 1 begint met de historische kadering van dit onderzoek, waarin de vraag van de huidige elektronica industrie naar goedkopere productiemethodes centraal staat. Verder wordt er een korte theoretische samenvatting gegeven over de oorsprong van de halfgeleider eigenschappen en het transport van ladingsdragers in P3AT. Afsluitend wordt de theorie over de generatie van ladingsdragers via lichtabsorptie in P3AT besproken.

In hoofdstuk 2 wordt een samenvatting gegeven van de belangrijkste methodes voor het produceren van nanovezels met als doel om ze te gebruiken in de actieve laag van organische elektronica. Daarnaast worden ook de verschillende huidige onderzoekstoepassingen van deze nanovezels belicht, hierbij wordt de nadruk gelegd op transistors en zonnecellen.

In hoofdstuk 3 komt eerst de productie en karakterisatie van P36T nanovezels in oplossing aan bod en vervolgens worden de nanovezeloplossingen gebruikt voor het maken van organische fototransistoren. Na depositie van de nanovezels op transistorsubstraten wordt de morfologie van de gevormde actieve lagen bepaald met een atomaire kracht microscoop. Daaropvolgend worden de transistorparameters opgemeten en wordt de responsiviteit en gevoeligheid onder invloed van licht bepaald. De analyse van de meetresultaten gebeurt aan de hand van de theorie die, samen met de schematische structuur van de fototransistoren, in het begin van het hoofdstuk gegeven wordt.

Hoofdstuk 4 omvat de conclusies van de bekomen meetresultaten en werpt ook een blik op de toekomst van het onderzoek in de organische elektronica.

Chapter 1

Introduction to organic optoelectronics

This chapter starts with a brief historical introduction to organic electronics and more in specific, organic transitors. Furthermore it situates the status of organic electronics on the market today and sets out its advantages as well as its current shortcomings, providing motivation for this thesis, of which also an outline is provided. Next, a structured theoretical introduction to charge carrier transport and charge carrier photogeneration in conjugated polymers is provided.

1.1 Motivation – Goal – Outline

1.1.1 The transistor, the basis of modern electronics

Looking back at the first half of the past century, one cannot ignore the awefull memory of death and destruction brought to us by WW I and II. Nevertheless, the wide spread of American army forces all over the world was a big driving force for improving long-range communication, largely stimulating investments in electronic research, especially in the domain of radio and telephone communication. Hence, it should be no surprise that probably the biggest electronic invention in this period was done in 1947 at Bell Laboratories when John Bardeen, Walter H. Brattain, and William Shockley invented the bipolar transistor.[1,2] It is without any doubt that they really did make the first working bipolar transistor, but the concept of a transistor was already described back in 1925 by Julius Edgar Lilienfeld, who patented his descriptions of both a bipolar and field-effect transistor in 1925 and 1928, respectively.[3] While in the first the current flowing between two electrodes was amplified by providing a control current through a third contact, in the second it was a voltage applied to a third contact that controlled the current flowing between the other two (Figure 1.1 (a) and (b)). Unfortunately, back then he was unable to test his discriptions in practice due to lack of high purity semiconductor material. In 1956 the Nobel Prize in Physics was awarded to John Bardeen, Walter H. Brattain and William Shockley for the invention of the biopolar transistor, which denoted the starting point of an electronics revolution, having tremendous impact on human society up to date. This is especially true during the last twenty to thirty years with the development and further improvement of computers, smartphones, gps systems…, all consisting of thousands of small transistors being part of the internal electronic circuits. However, the type of transistor dominating electronics these days is the Metal Oxide Semiconductor Field Effect Transistor (MOSFET). Introduced in 1959, this device amplifies the current flowing in the device channel between two contacts by applying a voltage to a third contact which is electrically isolated from the rest of the device via an insulating oxide layer.[4] A further

development of this MOSFET, called a Thin Film Transistor (TFT), is used in this thesis to study the optoelectronic properties of organic nanofibers (Figure 1.1 (c)).[5] While the operation of a MOSFET is based on the formation of an inversion layer to form a minority carrier conduction channel, the operation of a TFT is based on the formation of an accumulation layer to form a majority carrier conduction channel.

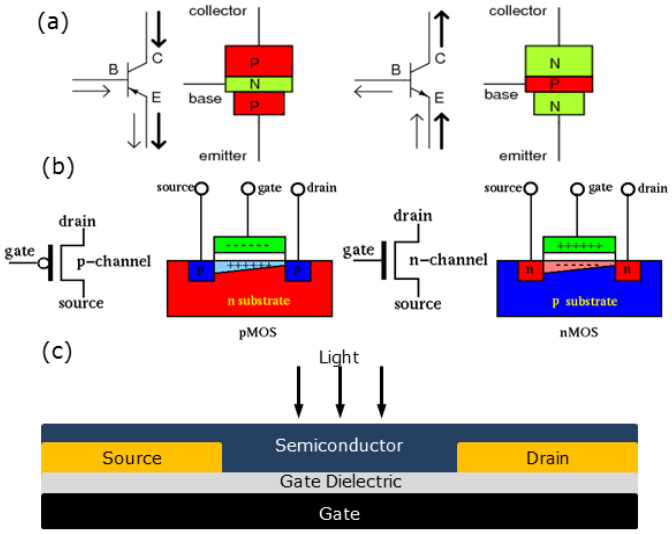

Figure 1.1 (a) Illustration of a pnp and an npn bipolar transistor. In the first an n-type material is sandwhiched between two p-type layers, while the opposite is true for the second. In both, a small current (thin arrow) flowing between base (B) and emitter (E) controls a large current (bolt arrow) flowing between collector (C) and emitter. (b) Illustration of a p-channel (pMOS) and an an n-channel (nMOS) MOSFET, for which a voltage applied to the gate controls the current flowing between source and drain. In the first the current is governed by holes, while in the second it is governed by electrons. (c) TFT phototransistor for which the current flowing between source and drain is controlled by a light pulse and/or a voltage applied to the gate.

Another key point in electronics history, relevant to this thesis, was the development of the phototransistor in 1948 by John N. Shive, also working at Bell Laboratories. However, besides being housed in a transparent casing such that a light beam instead of a voltage could be used to control the current flowing through the device, the overall device structure was not that much different from the normal bipolar transistor invented a year earlier.[6]

Referring to Figure 1.1 (c) again the TFTs studied here can actually be described as Thin Film Phototransistors having an organic semiconducting layer, such that they are also referred to as Organic Phototransistors (OPTs). In these OPT the charge carrier concentration in the channel region and therefore the current flowing between source and drain can be controlled by either a voltage applied to the gate or through the absorption of light impinging on the semiconducting layer from the top. However in many cases, both a voltage and light absorption are used to control the transistor current.

1.1.2 The organic revolution: Towards flexible electronics

Originally the material of choice for transistor fabrication was Ge, but it was very rapidly replaced with Si, having similar electronic properties but with the additional advantage of forming a stable oxide, necessary to make electrical insulations between distinct conducting parts of an integrated circuit (IC). Currently, the highest performances are reached with crystalline Si-based electronic devices, *e.g.* transistors, solar cells ... Despite their compatibility with current state-of-the-art mass production units, they require capital-intensive facilities encompassing a controlled environment for complex high temperature/vacuum processes.[7–11] As such, over the past twenty years, research is stimulated to look for cheaper alternatives and a viable one has been found in semiconducting polymers, due to their ability to be fully processed from solution via low-cost deposition techniques, *i.e.* spincoating, dropcasting, inkjet printing, roll-to-roll fabrication and bladecoating.[12–23] This would provide the industry with a way to effectively reduce the fabrication costs with the added benefit that also flexible plastic substrates could be used to make fully bendable, robust and light-weight electronic devices. Organic electronics are not expected to ever outperform crystalline silicon devices, having high computational powers, but their performance is expected to reach the level of amorphous silicon devices. Applications for organic electronics will therefore be in the range of low-cost microelectronics, *e.g.* radio-frequency identification tags, and devices which do not need fast switching speeds but do require large area coverage, *e.g.* active matrix displays.

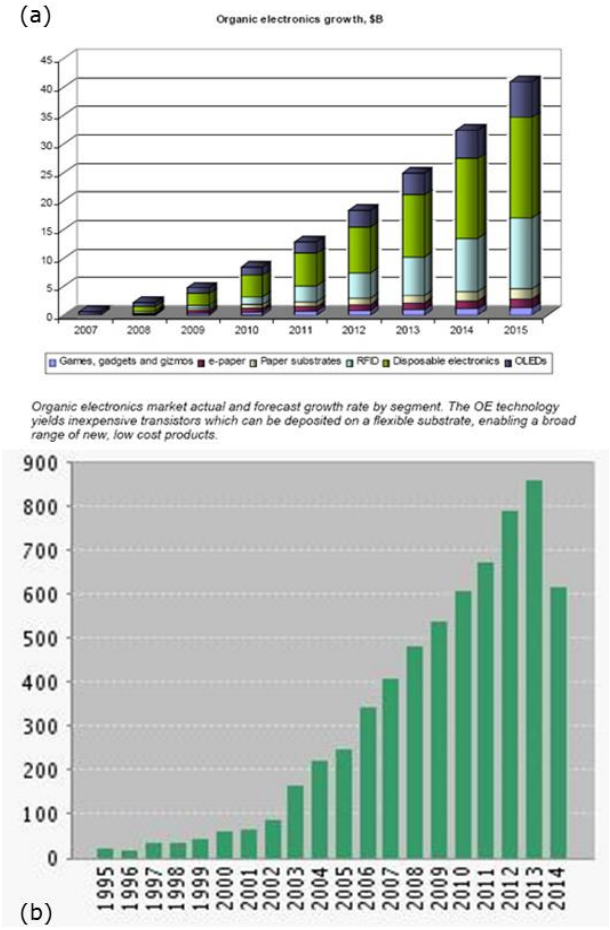

Figure 1.2. (a) Growth of the organic electronics market, source: Nanomarkets [2009]. (b) The number of research papers in the domain of organic and printable electronics continues to increase year after year, source: Web ofknowledge [September 2014].

Although the potential of organic materials constituting the active layer in electronic devices, and more specific organic field-effect transistors (OFETs), was already demonstrated in the 1960s,[24] it took until the 1980s before the OFET technology research was propelled with the demonstration of OFET capabilities in several distinct organic semiconductors.[25–27]

From an economical point of view, Figure 1.2 (a) illustrates that organic electronics awaits a bright future, as its market was predicted to increase by

more then 400% in five years time from less then $10 billion in 2010 to about $40 billion in 2015. Furthermore, also the number of research papers published yearly in the domain of organic electronics continues to rise year after year as illustrated by Figure 1.2 (b).

1.1.3 Goal of the thesis

Unfortunately, for organic electronics to compete with inorganic electronics, their ability to be fully fabricated via cheap solution coating techniques is not enough since they lack the high performance level associated with their inorganic counterparts. Part of this is due to their low level of active layer crystallinity. One possible way to tackle this is by incorporating preformed crystalline organic nanofibers in the active layer.[28–31] The aim of this work is to study the possibility of incorporating preformed poly(3-hexylthiophene) (P36T) nanofibers in the active layer of an OPT as a way to effectively increase the device performance, without the need of any post-production (thermal or solvent) or substrate surface treatment. One of the reasons why OPTs were chosen instead of any other organic electronic device is because upon deposition the nanofibers are lying parallel to the transistor/channel surface and therefore, directly provide an interconnected network along which the electrical current between source and drain can flow. Possible applications of OPT are light switches, light singal detectors, optical current amplifiers…, all which may benefit from the cheap mass production techniques available with organic nanofibers. It is shown that the nanofibers provide improved photoabsorption together with an increase in exciton diffusion length and charge carrier mobility, effectively boosting OPT performance relative to previously reported solution processed OPTs.[32–38] Furthermore, the OPTs show the possibility to straightforwardly adjust the photoresponsivity to the incident light by varying the applied gate bias.

1.1.4 Thesis outline

Starting off with a quick overview of transistor history and stating the advantages and disadvantages of organic electronics, chapter I provides a

structured introduction and explains the aim of this work. In the next part of this chapter the basic chemical structure and the origin of semiconducting properties in conjugated polymers is explained. The chapter is finalized by a short theoretical part concerning the transport and photogeneration of electrical charge carriers in conjugated polymers.

Chapter II starts by reviewing the different methods for the production of poly(3-alkylthiophene) (P3*A*T) nanofibers, with a clear focus on those methods which are most suited for practical applications, *i.e.* the cheap and straightforward production of organic electronic devices. For convenience, following the methods of production, the current research status of P3*A*T nanofiber applications in the active electronics layer is provided. Here, the applications are limited to the fabrication of transistors and solar cells.

Chapter III starts by introducing the current status of OPT research, followed by a theoretical part on the OPT device structure and its operation mechanisms. Next, the practical work of this thesis is introduced, starting with the fabrication and characterization of the different P36T fiber containing solutions and one well-dissolved P36T solution. Along the way, Atomic Force Microscopy (AFM) proved to be an important tool for the dimensional characterization of deposited nanofibers and the morphological characterization of OPT active layers fabricated using these solutions. Successively, the fabricated OPTs were characterized for their field-effect transistor (FET) operation, revealing a better operation of the fiber-based OPT with respect to the ones fabricated from the solution containing well-dissolved P36T. Additionally, a surface coverage dependent operation was found for the nanofiber-based OPT. Showing good FET operation, the OPTs were then subjected to an incident light beam directed perpendicularly on the uncovered top of the OPT. In this way, the incident light beam was not obstructed, such that its full potential could be used to generate charge carriers within the OPT active layer.

Chapter IV finally concludes this work by symmarizing the practical results

obtained from P36T nanofiber-based OPTs. In addition, it provides an outlook of the research on nanofiber-based electronics.

1.2 The name is bond… π−bond

This part deals with the asic chemical structure and origin of semiconducting properties in conjugated polymers, which can be brought back to presence of alternating single and double bonds along the polymer backbone.

A modern definition of a semiconductor states: "A semiconductor is a material that is an insulator at very low temperature, but which has a sizeable electrical conductivity at room temperature. The distinction between a semiconductor and an insulator is not very well-defined, but roughly, a semiconductor is an insulator with a band gap small enough that its conduction band is appreciably thermally populated at room temperature." In order to classifty conjugated polymers according to this definition as semiconductors, a lot of research work has been going on since their discovery during the second half of the twentieth century. A major breakthrough regarding the potential of conjugated polymers in electronic devices was made in 1977 when Heeger, MacDiarmid and Shirakawa discovered that the electrical conductivity of polyacetylene increased by eight orders of magnitude from 10^{-5} S cm^{-1} to 10^{3} S cm^{-1} when chemically doping it with either reducing or oxidizing agents.[39] Unfortunately, these conjugated polymers appeared to suffer from a low solubility, providing a second working point before they could be used in electronic devices. Nowadays, P3*A*Ts are the most studied conjugated polymers, possessing good solubility in various commonly used solvents in combination with good electrical conductivity.

From a chemical point of view, the backbone of conjugated polymers consists of carbon atoms connected via alternating double and single bonds (Figure 1.3, Middle left). This alternating structure originates from the sp^2 hybridization inherent to the atomic orbitals (AOs) of each carbon atom along the polymer backbone. In its ground state, the AOs are arranged in a $1s^2 2s^2 2p^2$ configuration around the carbon nucleus with four electrons (two s-

and two p-electrons) residing on the outer electron shell, such that four different chemical bonds can be formed with neighbouring atoms. However, depending on the number of neigbouring atoms, the AOs of the outer electron shell hybridize in sp, sp^2 or sp^3 orbitals in order to increase the bond stability. This is accomplished by redistributing the energy of the AOs involved over the newly hybridized ones. Since now each carbon atom along the polymer backbone has three nearest neigbour atoms, *i.e.* one hydrogen atom and two carbon atoms in the case of polyacetylene, three of its outer atomic orbitals (1 x 2s and 2 x 2p) will hybridize in three new sp^2 orbitals having an energy level somewhere in between that of a 2s- and a 2p-orbital and positioned in the same plane around the carbon atom with an angle of 120° between them. The remaining unhybridized 2p-orbital is positioned perpendicular to the plane of the sp^2 hybridized orbitals (Figure 1.3, Top left and right). In the case of polyacetylene, the three in-plane carbon sp^2-orbitals will overlap head-on with the 1s-orbital of the hydrogen atom or one of the sp^2-orbitals of a neigbouring carbon atom, forming a strong σ-bond. A weaker π-bond is formed via lateral overlap between the unhybridized 2p-orbitals of the carbon atoms along the backbone. As such, each carbon atom forms a single σ-bond with one neighbouring hydrogen atom and one neighbouring carbon atom, while forming both a σ-bond and a π-bond, *i.e.* a double bond, with the second neighbouring carbon atom (Figure 1.3, Top right). In this way an alternation of double and single bonds is obtained along the polymer backbone. Due to their nature, bond rotation is only possible for single bonds but not for double bonds, making conjugated polymers rather semiflexible than flexible. Additionally, the nature of alternating π-bonds, being formed due to a lateral overlap of p-orbitals, delocalizes the involved electrons along the polymer backbone such that they do not belong to a single atom anymore (Figure 1.3, Middle). Differently said, the alternation of π-bonds is responsible for charge carrier conduction along the polymer backbone.

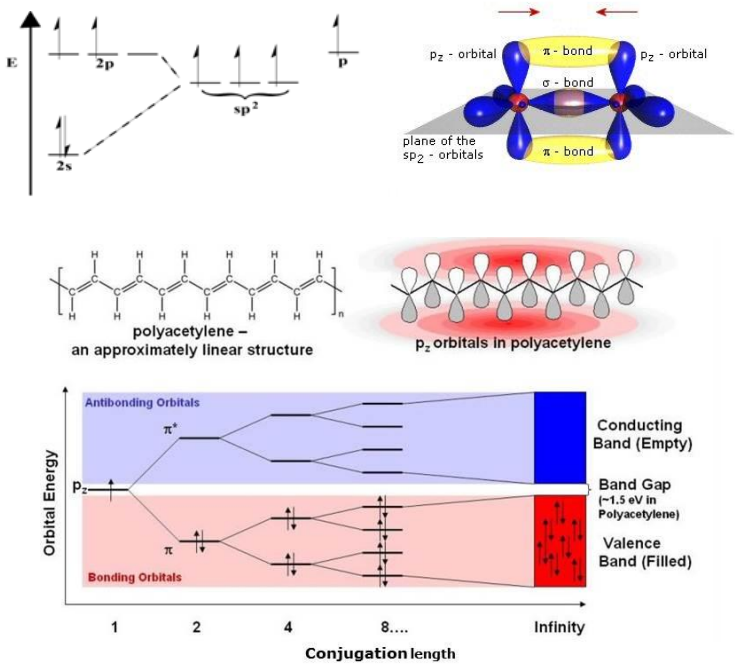

Figure 1.3. Top left: Illustration of the AO energy level redistribution inherent to the sp^2 hybridization of a carbon atom along the backbone of a conjugated polymer. Top right: Double bond formation between two carbon atoms (red balls) along the backbone of a conjugated polymer, source: Organic Semiconductor World. Middle left: Structure of the basic conjugated polymer, polyacetylene, showing the alternation of single and double bonds. Middle right: Lateral overlap of p_z-orbitals forms the basis for electron delocalization, giving the polymer its semiconducting property. Bottom: Decrease in either bonding or antibonding π-orbital energy level separation leading to the formation of respectively a valence band and conduction band with increasing conjugation length, source: Heroes Community.

The semiconducting nature of conjugated polymers originates from way in which AOs along the polymer backbone interact. This interaction can either be destructive or non-destructive. While the latter leads to the formation of bonding, low-energy molecular π-orbitals, the former results in the formation of antibonding, high-energy molecular π-orbitals. As such, the number of molecular orbitals (MOs) formed is equal to the number of interacting AOs and hence the number of interacting atoms. Just as with inorganic semiconductor, the more atoms are involved (increase in polymer conjugation length), the

more bonding and antibonding MOs will be created and the less they will be energetically separated. Eventually, the MOs will merge together, forming a valence band out of the bonding π-orbitals and a conduction band out of the antibonding π-orbitals (Figure 1.3 Bottom). As the electrons first fill the lowest possible energy levels, the highest occupied molecular orbital (HOMO) level is commonly defined as the upper edge of the valence band and the lowest unoccupied molecular orbital (LUMO) level as the lower edge of the conduction band. The bandgap is then related to the energy difference between HOMO and LUMO. However, as will be more elaborately explained in the next section, in practice it is hard to define a specific band edge level and an associated energy bandgap for organic semiconductors.

1.3 Charge carrier transport

In absence of an applied electric field, charge carriers move randomly under the influence of their thermal motion. Afterall, this random thermal motion averages out over time and no net movement of charge can be observed. However, when an external driving force is applied in the form of an electric field, charge carriers start to move in the direction of this field and a net movement of charge carriers is observed. As the electric field is applied continuously, the charge carriers will also be continuously accelerated, which in vacuum results in relativistic charge carrier velocities. Since here solid polymeric materials are studied, charge carriers will, besides being continuously accelerated by the applied electric field, also continuously be scattered around due to imperfections in the material and collisions with other charge carriers. In this way, charge carriers will reach a finite final velocity. The material parameter providing the link between the applied electric field and the charge carrier velocity, hence taking into account material related scattering events, is the charge carrier mobility μ, defined as $v = \mu \cdot E$, with v the speed of the electrical charge when an electric field E is applied across a piece of the considered material. Alternatively, the mobility can also be defined as $\mu = e \cdot \tau_{sc} / m^*$, with e the elementary

charge, τ_{sc} the time between different scattering events and m^* the effective mass of an electron. In the case of organic semiconductors, μ is a function of the applied electric field E, the temperature T and the charge carrier density n.

In the following part, two models describing the charge transport in organic semiconductors will be introduced. The first is more applicable to polycrystalline[‡] and amorphous organic materials and the second is more suited for semicrystalline organic materials, like P36T. Furthermore, when describing the charge carrier transport in organic materials, a clear distinction is made between the faster intramolecular transport along one polymer chain and the slower intermolecular transport from one polymer chain to the other.

1.3.1 Hopping transport

As already mentioned, the ideal case of well-defined band edges and energy bandgaps is never reached, especially not with polycrystalline and amorphous organic semiconductors for which disorder continuously interrupts the π-conjugated system along the polymer backbone. Disorder can be subdivided into two different types, positional disorder coming from local variations in polymer chain orientation and energetic disorder coming from differences in the local chemical environment. Nevertheless, the effect of both is same, the π-conjugated system is broken and becomes restricted to polymer chain segments of roughly 5 nm in length. As such, instead of being delocalized over the entire polymer chain, charges become localized in these short chain segments and long-range transport is only possible by hopping from one short segment to the other. For these materials, the concept of energy band transport with well-defined HOMO and LUMO breaks down. Instead, the short chain segments are regarded as localized transport sites with a Gaussian distribution centered on both the HOMO and LUMO level (Figure 1.4). Charge transport is then governed by hopping from an occupied state with energy E_i to an unoccupied state with energy E_j with a hopping rate v_{ij}, which has been modelled by Miller and Abrahams as:[40]

$$\nu_{ij} = \nu_0 \exp\left(-2\gamma\Delta R_{ij}\right) \begin{cases} \exp\left(-\frac{E_j - E_i}{k_B T}\right) & E_i < E_j \\ 1 & E_i > E_j \end{cases} \quad (1.1)$$

In the above relation ν_0 is a constant, γ^{-1} is the charge carrier localization length and ΔR_{ij} is the spatial distance between state E_i and state E_j. The first factor on the right is related to phonon-assisted tunneling, while the second is a Boltzmann factor representing thermally activated hopping whenever $E_i < E_j$. Hopping to a lower energy state is not thermally activated. The Miller-Abrahams relation for the hopping rate forms the basis of different models describing charge carrier transport in disordered amorphous and polycrystalline organic semiconductors. For example, Mott proposed the phonon-assisted tunneling mechanism as the basis for long-distance hopping between sites for which the energetic separation is high enough.[41–43] This concept is also referred to as variable range hopping (VRH). Assuming VRH with an exponential distribution of localized states and percolation, Vissenberg and Matters proposed a very reliable model to describe charge carrier transport in OFETs.[44]

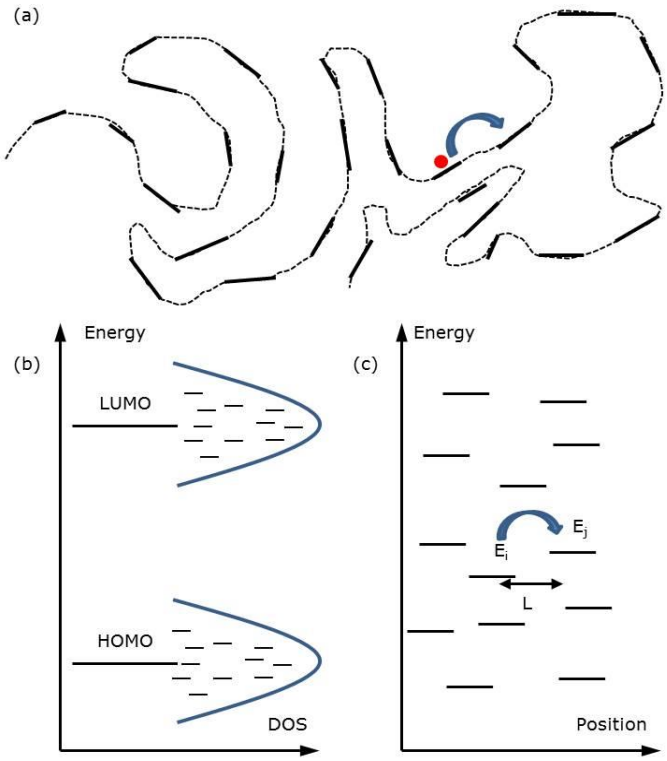

Figure 1.4. (a) Disordered semiconducting polymer chain with short conjugated chain segments indicated by the short black bars. The blue arrow indicates a hopping event for a charge carrier (red ball) from one localized segment to the other. (b) The DOS of the disordered polymer consists of two Gaussian distributions of localized energy states centered on both the HOMO and the LUMO level of the polymer. (c) Energy level langscape illustrating the phonon-assisted hopping mechanism between two spacially separated transport states with energies E_i and E_j and spatial separation L.

Although a variety of models has been described, basically they all predict the same behavior and in general the following relations hold:

$$\mu \sim \exp(\sqrt{E / E_0}) \tag{1.2a}$$

$$\mu \sim \exp(-E_a / k_B T) \tag{1.2b}$$

$$\mu \sim n^{\alpha} \tag{1.2c}$$

The first relation represents the Poole-Frenkel dependence with E the applied

electric field and E_0 a constant depending on the material permittivity. The second is related to thermally activated hopping from one localized chain segment to the other as determined by the Miller-Abrahams relation. Finally, the last relation is correlated with the Gaussian distribution of localized states and following this relation μ also depends on the gate voltage V_{GS} according to the same power law, for $n \sim V_{GS}$. The exponent a in this equation is temperature dependent, $a \sim 1/T$.

1.3.2 Mobility edge model

The mobility edge model[45,46] is derived from the multiple trapping and release model developed for amorphous hydrogenated silicon[47] and is applicable to semicrystalline polymers, like P3*A*Ts. As these are composed of well-ordered large crystalline domains separated by disordered amorphous grain boundaries, the charge carrier transport cannot be successfully described by hopping from one localized state to the next. Rather, due to the long-range order in the crystalline domains, meaning that the polymer chains possess a high level of conjugation, the charge carriers can move in delocalized energy bands within these domains. On the other hand, the amorphous grain boundary consists of localized trap states for which the mobility is zero. An illustration of this model is given in Figure 1.5. Nevertheless, trapped charges can escape from the grain boundary into the grain via a thermally activated hopping process. As such, the effective charge carrier mobility μ_{eff} is described in this model as:

$$\mu_{eff} = \mu_0 \frac{n_{free}}{n_{total}} \tag{1.3}$$

with $n_{total} = n_{free} + n_{trap}$ the total charge carrier concentration, while n_{free} and n_{trap} are the free and trapped charge carrier density and μ_0 is the constant grain mobility.

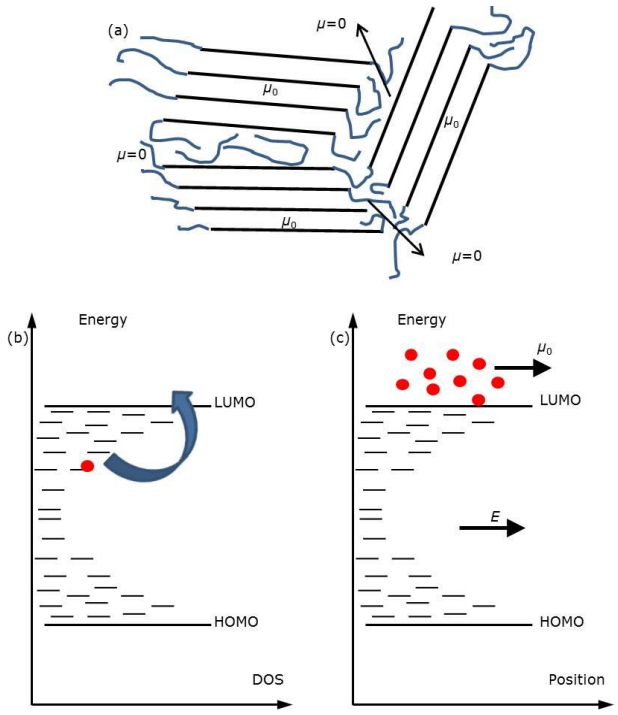

Figure 1.5 Illustration of the mobility edge model. (a) Semicrystalline conjugated polymer with long-range ordered grains in which the polymer chains possess a large conjugation length, as represented by the straight black lines. The ordered grains are separated by disordered grain boundaries designated by the blue lines. In the grains the charge carrier mobility is given by μ_0, while in the grain boundaries, the charge carriers are trapped and the mobility is zero. (b) Thermally assisted hopping as a way for a charge carrier to escape from a trap state into the conduction band. (c) Charge carriers move in the conduction band with a mobility μ_0 under the influence of an applied electric field.

Furthermore, the model stipulates that the mobility depends on the applied electric field E, the temperature T and the total charge carrier density n_{total} according to the following relations:

$$\mu_{eff} \sim \exp(\sqrt{E / E_0}) \tag{1.4a}$$

$$\mu_{eff} \sim \exp(-E_a / k_B T) \tag{1.4b}$$

$$\mu_{eff} \sim n_{total}^{a} \tag{1.4c}$$

The first relation represents the Poole-Frenkel dependence with E_0 a constant

depending on the material permittivity. The second is related to thermally activated hopping from a localized trap state and the third is correlated with the exponential distribution of localized trap states. The value of the exponent in this case is again temperature controlled.

1.4 Charge carrier photogeneration

Although conjugated polymers with a high absorption coefficient of approximately 10^5 cm^{-1} are able to efficiently absorb light at the maximum of their absorption spectrum,[48,49] the creation of free electron-hole pairs via photoabsorption in pristine organic semiconductors is not evident. The low dielectric constant of these materials, the electron-electron correlation and electron-phonon coupling inherent to them result in a much stronger coulombic interaction between electrons and holes. For this reason, following a photoabsorption event, the primarily generated excitation is a strongly bound electron-hole pair, also called an exciton, instead of a free electron-hole pair as for inorganic semiconductors.[50] To separate a photogenerated exciton, a certain amount of excess energy is needed to surmount the potential barrier separating the excitonic state form the free electron-hole pair state. The amount of excess energy needed equalizes the excitonic binding energy and can either be thermal, optical or electrical in origin. Figure 1.6 illustrates different possible routes for free charge carrier generation under the influence of an external applied electric field.[51–53] Photogeneration creates lowest and higher energy singlet exciton states, respectively denoted by S_1 and S_n, via processes denoted by 1 and 2, respectively.

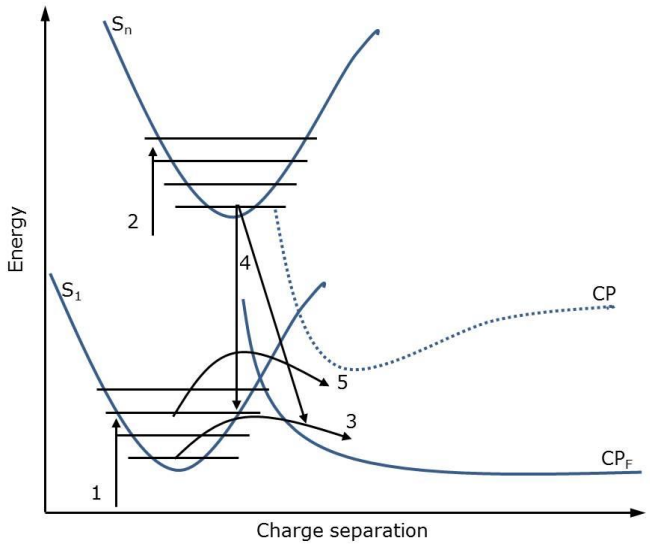

Figure 1.6. Illustration of free charge carrier generation in a pristine semiconducting polymer under the influence of an external applied electric field. S_1 and S_n indicate the lowest and a higher energy excitonic singlet state, which are entered via photoabsorption as indicated by arrows 1 and 2, respectively. CP and CP_F are the unmodified and the modified barrier charge pair state. Barrier modification is obtained by the external applied field. CP_F represents the state with free charge carriers. Arrow 3 illustrates free charge carrier generation from a thermalized singlet ground state. 4 illustrates that a higher energy singlet state can either relax into S_1 or split up into free charge carriers via autoionization. Arrow 5 illustrates free charge carrier generation out of vibrationally hot singlet state S_1.

Followingly, free charge carriers can be generated from the thermalized singlet sate S_1 via process 3, since the free charge barrier is lowered by the external applied field. Additionally, as proposed by Pope and Geacintov, excess photon energy can create a higher energy singlet exciton S_n, which can relax either to S_1 or autoionization may take place in which the singlet exciton is split up in free charge carriers during its relaxation to S_1 (process 4).[52] Yet, another possible route uses excess vibrational energy for free charge generation starting from a vibrationally hot singlet S_1 state to overcome the free charge barrier (process 5).[53]

An example where the excess energy comes from an optical source is given by the bulk heterojunction (BHJ) organic photovoltaics (OPV), illustrated in Figure 1.7.[54,55] Upon photoabsorption, the generated exciton diffuses to the donor-acceptor interface where it forms a charge transfer complex, with the electron transferring from the LUMO of the donor to the LUMO of the acceptor and the hole remaining on the HOMO of the donor. This is accomplished by the built-in potential difference resulting from the energy level difference between the LUMOs of the donor and acceptor material.[56,57] At this point, the Coulombic binding energy between the electrons and the holes is largely reduced and only a small amount of added excess energy via photoabsorption is enough to obtain separated free charge carriers.

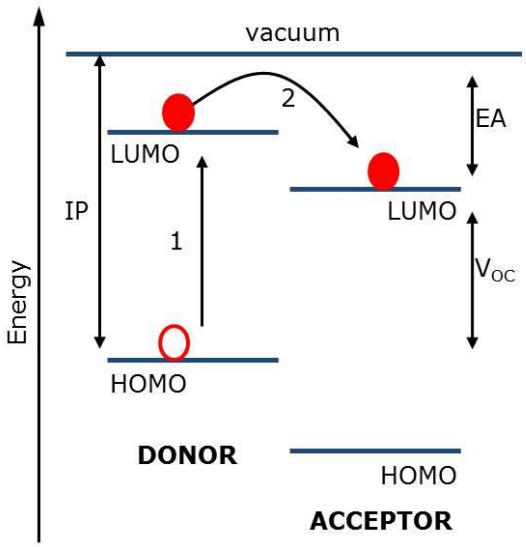

Figure 1.7. Schematic illustration of charge carrier generation in an organic BHJ solar cell. Arrow 1 indicates the process of photoabsorption in the donor material leading to the formation of an exciton. Process 2 illustrates the exciton splitting at the donor–acceptor interface, which is facilitated by the formation of a charge transfer complex. IP and EA denote the donor ionization potential and the acceptor electron affinity respectively. V_{oc} denotes the open-circuit voltage of the solar cell and is related to the difference between the HOMO of the donor and the LUMO of the acceptor.

For organic phototransistors, the BHJ concept is only limitedly applied[18] and therefore the active layer is mostly composed of just one type of material. In

this case, the exciton dissociation efficiency is largely controlled by the vertical and horizontal electric fields resulting from the applied gate and drain biases, respectively.[19–38] In addition, also the possibly present Schottky barrier between the metallic source/drain contacts and the organic semiconductor creates a band bending of which the associated electric field can assist in exciton dissociation in the neighbourhood of the metallic contacts.[58] However, the impact of this on the exciton dissociation efficiency is rather small as compared with that of the applied electric fields since it does not reach any further than a distance of 5−15 nm, the exciton diffusion length in organic semiconductors, from the metallic contacts.

1.5 Notes

‡ Polycrystalline materials are solids that are composed of many crystallites of varying size and orientation. Crystallites are also referred to as grains. They are small or even microscopic crystals and form during the cooling of many materials. Source: S. Allen and E. Thomas, *The Structure of Materials*, 1999, (New York: John Wiley & Sons, Inc.).

1.6 References

1 J. Bardeen and W. H. Brattain, *Phys. Rev.*, 1948, **74**, 230.

2 W. Shockley, *Bell Syst. Tech. J.*, 1949, **28**, 435.

3 J. E. Lilienfeld, *Method and apparatus for controlling electric current*, 1925 (US 1745175 first filed in Canada on 1925-10-22).
J. E. Lilienfeld, *Device for controlling electric current,* 1928 (US 1900018 filed on 1928-03-28).

4 D. Kahn, M. M. Atalla, in *IRE Solid-State Devices Research Conference*, Pittsburgh, PA, 1960, D. Kahng, US Patent 3, 102, 230, 1963.

5 P. K. Weimer, *Proc. IRE*, 1962, **50**, 1462.

6 J. N. Shive, *J. Opt. Soc. Am.*, 1953, **43**, 239.

7 N. Espinosa, M. Hosel, D. Angmo, F. C. Krebs, *Energy Environ. Sci.*, 2012, **5**, 5117.

8 N. M. Johnson and A. Chiang, *Appl. Phys. Lett.*, 1984, **45**, 1102.

9 Y. Kaneko, N. Koike, K. Tsutsui and T. Tsukada, *Appl. Phys. Lett.*, 1990, **56**, 650.

10 C. S. Choi, H. S. Kang, W. Y. Choi, H. Kim J, W. J. Choi, D. J. Kim, K. C. Jang and K. S. Seo, *IEEE Photon. Technol. Lett.*, 2003, **15**, 846.

11 H. S. Kang, C. S. Choi, W. Y. Choi, D. H. Kim and K.S. Seo, *Appl. Phys. Lett.*, 2004, **84**, 3780.

12 S. R. Forrest, *Nature*, 2004, **428**, 911.

13 A. J. Heeger, *Angew. Chem. Int. Ed.*, 2001, **40**, 2591.

14 A. Facchetti, M. H. Yoon and T. J. Marks, *Adv. Mater.*, 2005, **17**, 1705.

15 B. Crone, A. Dodabalapur, Y. Y. Lin, R. W. Filas, Z. Bao, A. LaDuca, R. Sarpeshkar, H. E. Katz and W. Li, *Nature*, 200, **403**, 521.

16 Z. Bao, *Semiconductive Polymers*, ed B. Hseih, Y. Wei and M. E. Galvin, 1999, (Washington, DC: American Chemical Society)

17 R. M. Meixner, H. Göbel, F. A. Yildirim, W. Bauhofer and W. Krautschneider, *Appl. Phys. Lett.*, 2006, **89**, 092110.

18 N. Marjanovic, Th. B. Singh, G. Dennler, S. Gunes, H. Neugebauer, N. S. Sariciftci, R. Schwödiauer and S. Bauer, *Org. Electron.*, 2006, **7**, 188.

19 J. A. Rogers, Z. N. Bao, A. Makhija and P. Braun, *Adv. Mater.*, 1999, **11**, 741.

20 Y. Xia and G. M. Whitesides, *Angew. Chem. Int. Ed.*, 1998, **37**, 550.

21 T. R. Hebner, C. C. Wu, D. Marcy, M. H. Lu and J. C. Sturm, *Appl. Phys. Lett.*, 1998, **72**, 519.

22 Y. Yang, S. C. Chang, J. Bharathan and J. Liu, *J. Matter. Sci. Mater. Electron.*, 2000, **11**, 89.

23 O. Yokoyama, *Optronics*, 2003, **254**, 119.

24 G. H. Heilmeier and L. A. Zanoni, *J. Phys. Chem. Solid*, 1964, **25**, 603.

25 F. Ebisawa, T. Kurokawa and S. Nara, *J. Appl. Phys.*, 1983, **54**, 3255.

26 A. Tsumura, H. Koezuka and T. Ando, *Appl. Phys. Lett.*, 1986, **49**, 1210.

27 G. Horowitz, D. Fichou, X. Peng, Z. Xu and F. Garnier, *Solid State Commun.*, 1989, **72**, 385.

28 S. Berson, R. De Bettignies, S. Bailly and S. Guillerez, *Adv. Funct. Mater.*, 2007, **17**, 1377.

29 W. D. Oosterbaan, J. C. Bolsée, A. Gadisa, V. Vrindts, S. Bertho, J. D'Haen, T. J. Cleij, L. Lutsen, C. R. McNeill, L. Thomsen, J. V. Manca and D. Vanderzande, *Adv. Funct. Mater.*, 2010, **20**, 792.

30 W. D. Oosterbaan, J. C. Bolsée, L. Wang, V. Vrindts, L. J. Lutsen, V. Lemaur, D. Beljonne, C. R. McNeill, L. Thomsen, J. V. Manca and D. J. M. Vanderzande, *Adv. Funct. Mater.*, 2014, **24**, 1994.

31 S. Bertho, W. D. Oosterbaan, V. Vrindts, J. C. Bolsée, F. Piersimoni, D. Spoltore, J. D'Haen, L. Lutsen, D. Vanderzande and J. V. Manca, *Adv. Mater. Res.*, 2011, **324**, 32.

32 K. S. Narayan and N. Kumar, *Appl. Phys. Lett.*, 2001, **79**, 1891.

33 M. C. Hamilton, S. Martin and J. Kanicki, *IEEE Trans. Electron Devices*, 2004, **51**, 877.

34 M. C. Hamilton and J. Kanicki, *IEEE J. Sel. Top. Quantum Electron.*, 2004, **10**, 840.

35 Y. Xu, P. R.Berger, J. N. Wilson and U. H. F.Bunz, *Appl. Phys. Lett.*, 2004, **85**, 4219.

36 M. Deen and M. H. Kazemeini, *Proc. IEEE.*, 2005, **93**, 7.

37 H. Dong, H. Li, E. Wang, H. Nakashima, K. Torimitsu and W. Hu, *J. Phys. Chem. C*, 2008, **112**, 19690.

38 T. Pal, M. Arif and S. I. Khondaker, *Nanotechnology*, 2010, **21**, 325201.

39 H. Shirakawa, E. J. Louis, A. G. MacDiarmid, C. K. Chiang, A. J. Heeger, *J. Chem. Soc., Chem. Commun.*, 1977, **16**, 578.

40 A. Miller and E. Abrahams, *Phys. Rev.*, 1960, **120**, 745.

41 N. F. Mott, *Canadian J. Phys.*, 1956, **103**, 51.

42 N. F. Mott, *J. Non-Cryst. Solids*, 1968, **1**,1.

43 N. F. Mott and E. A. Davies, Electronic processes in non-crystalline materials, 2nd edition, Oxford University Press, London, 1979.

44 M. C. J. M. Vissenberg and M. Matters, *Phys. Rev. B*, 1998, **57**, 12964.

45 A. Salleo, T. W. Chen, A. R. Volkel, Y. Wu, P. Liu, B. S. Ong and R. A. Street, *Phys. Rev. B*, 2004, **70**, 115311.

46 R. A. Street, J. E. Northrup and A. Salleo, *Phys. Rev. B*, 2005, **71**, 165202.

47 G. Horowitz, R. Hajlaoui and P. Delannoy, *J.Phys. III France*, 1995, **5**, 355.

48 H. Hoppe, N. Arnold, N. S. Sariciftci and D. Meissner, *Sol. Energy Mater. Sol. Cells*, 2003, **80**, 105.

49 U. Zhokhavets, T. Erbs, G. Gobsch, M. Al-Ibrahim and O. Ambacher, *Chem. Phys. Lett.*, 2006, **418**, 347.

50 K. J. Baeg, M. Binda, D. Natali, M. Caironi and Y. Y. Noh, *Adv. Mater.*, 2013, **25**, 4267.

51 I. G. Scheblykin, A. Yartsev, T. Pullerits, V. Gulbinas and V. Sundström, *J. Phys. Chem. B*, 2007, **111** , 6303.

52 N. Geacintov and M. Pope, *J. Chem. Phys.*, 1967, **47**, 1194.

53 V. I. Arkhipov, E. V. Emelianova and H. Bässler, *Phys. Rev. Lett.*, 1999, **82**, 1321.

54 M. A. Ruderer and P. Muller-Buschbaum, *Soft Matter*, 2011, **7**, 5482.

55 M. A. Brady, G. M. Su and M. L. Chabinyc, *Soft Matter*, 2011, **7**, 11065.

56 G. Yu, J. Gao, J. C. Hummelen, F. Wudl and A. J. Heeger, *Science*, 1995, **270**, 1789.

57 A. C. Mayer, S. R. Scully, B. E. Hardin, M. W. Rowell and M. D. McGehee, *Mater. Today*, 2007, **10**, 28.

58 H. Hoppe and N. S. Sariciftci, *J. Mater. Res.*, 2004, **19**, 1924.

Chapter 2

Poly(3-alkylthiophene) nanofibers for optoelectronic applications

Semiconducting poly(3-alkylthiophene) nanofibers show remarkable optical and electrical properties, and because of their high aspect ratio they are perfectly suited to serve as organic quasi one-dimensional charge carriers. Hence, they offer interesting perspectives for next generation printable optoelectronic applications. This chapter provides an overview of the current state of the art regarding the preparation and characterization of poly(3-alkylthiophene) nanofibers, and a discussion on nanofiber-based optoelectronic applications, *i.e.* organic field-effect transistors and bulk heterojunction organic solar cells.

2.1 Fabrication methods

Among the various existing conjugated polymer semiconductors, poly(3-alkylthiophenes) or P3*A*Ts, as depicted in Figure 2.1, have received considerable attention because of their good processability, favourable optoelectronic properties and ability to form crystalline structures, *e.g.* self-assembled nanofibers, from solution via strong π-π interactions along their longitudinal axis. As such, they have become model systems in the field of organic electronics. An important milestone in this development was provided by Ihn *et al.*,[1] who demonstrated that, in poor solvents, P3*A*T may crystallize into nanofibers, forming a stable dispersion.

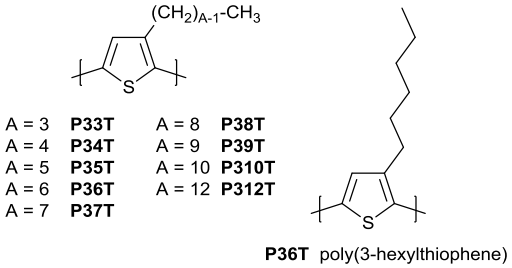

Figure 2.1. Chemical structure of poly(3-alkylthiophene)s (with A representing the number of carbon atoms in the alkyl side chain).

Conjugated polymer nanofiber dispersions can be fabricated according to various different methods via self-assembly in solution. Herein, the solution self-assembly methods are subdivided in three different approaches, i.e. the 'marginal' solvent approach, the mixed solvent approach and the good solvent approach. In addition, also electrospinning is mentioned as a technique capable of producing continuous, long nanofibers which can be directly captured and directed onto a substrate of choice.

2.1.1 Solution self-assembly

Marginal solvent approach. From an industrial point of view this approach is most appealing because of its low cost and potential for

mass production. In a first step, a certain amount of P3*A*T material is dissolved in a 'marginal' solvent - good enough to dissolve the polymer at elevated temperature but poor enough to initiate polymer aggregation at room temperature - while stirring at elevated temperature (50–80 °C for P36T). The polythiophene material is completely dissolved when an orange transparent solution is obtained. The temperature at which this happens depends on different solution parameters and should be determined first by a stepwise heating protocol. In the next step, the solution is cooled down to room temperature, mostly at a rate of about 20–25 °C/h, to decrease the solubility of the polymer and hence induce aggregation, *i.e.* nanofiber formation, observed as a transition from an orange to a dark red or purple solution.[1–8] As illustrated in Figure 2.2, fiber formation can be confirmed by the evolution of the UV-Vis absorption spectrum after cooling the solution to room temperature. Immediately after cooling, one single absorption band around λ = 450 nm is observed, typical for the π-π* transition of well-dissolved polythiophene chains. After 4 hours of storage, in the absence of ambient air and light, a red-shifted absorption band with a vibrational finestructure having additional absorption peaks, typically at λ = 525, 550 and 610 nm, can be seen. These vibrational features are related to the presence of crystalline nanofibers.[2–8] The intensity decrease of the absorption band at 450 nm after 4 hours of storage was used to estimate the nanofiber yield in solution.[2] However, fitting the UV-Vis spectrum of the pristine polymer solution with the spectra obtained from the pure fiber fraction and the well-dissolved polymer fraction provides a more reliable way of determining the fiber yield.[4] For a 1 wt% solution of P36T in *p*-xylene the spectrum stops evolving after 48 hours of storage and is reported to remain the same for more than a month without the formation of precipitates. As a result, fiber formation was concluded to be complete and, more importantly, the fibers were found highly stable.[2] A similar solution stability was observed by Oosterbaan *et al.*,[4] but the

stabilization process was seen to extend with elongating alkyl side chain length.

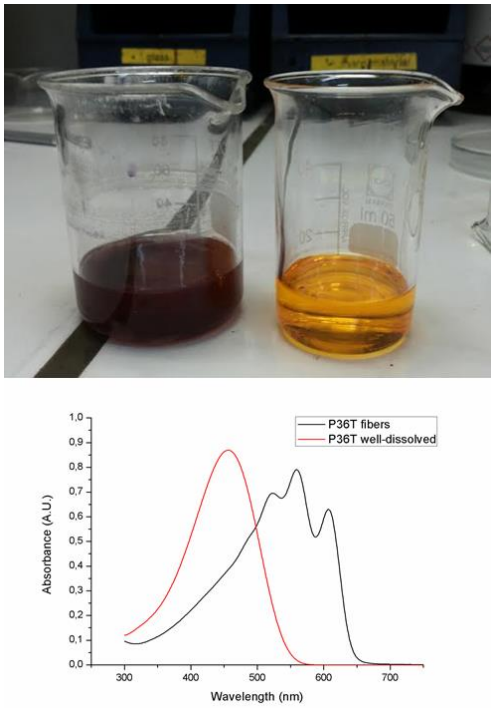

Figure 2.2. Top: *p*-xylene solutions containing P36T nanofibers at room temperature (left) and well-dissolved P36T (right). Bottom: UV-Vis absorption spectra of a dispersion of isolated P36T fibers in *p*-xylene at r.t., and of the same solution but recorded after dissolving the fibers at high temperature followed by quickly cooling to r.t., *i.e.* a solution of well-dissolved P36T (Reproduced with data from Ref. 4).

The mechanism behind the fiber formation was reported to follow a two-step process, consisting of a coil-to-rod transformation of the polymer chains followed by crystallization of the polymer backbones and the alkyl side chains. In order for this process to occur, the loss of conformational entropy suffered by the polymer chains has to be energetically compensated by the cooperation of the π-π interactions along the polymer backbones and the Van der Waals interactions of the alkyl side chains.[9–11] With the main driving force for solution self-assembly provided by the π-π interactions, the fibers grow quasi one-

dimensionally, with their longitudinal axis along the π-π stacking direction and the alkyl chains perpendicular to this axis.[1] A schematic illustration of the internal fiber structure is given in Figure 2.3[12]. The nanofiber production process is evidently strongly affected by the P3*A*T alkyl chain length and parameters such as solvent quality, cooling rate, polymer concentration, regioregularity, and molecular weight.[2–8] Separation of the nanofibers from the well-dissolved polymer by centrifugation and subsequent determination of the molecular weight distribution by gel permeation chromatography (GPC) revealed some extent of fractionation, with the higher molecular weight chains incorporated in the nanofibers and the lower molecular weight species being well-dissolved.[2–4] Fractionation likely occurs due to the fact that for smaller polymer chains, the cooperative interactions are not large enough to overcome the entropic energy loss, thus preventing crystallization. The lower molecular weight boundary for P3*A*T nanofiber formation was estimated to correspond to ~60–70 monomer units, roughly the length an extended polymer chain needs to possess to span the width of a nanofiber.[3] Schwarz *et al.*[13] modelled a 0.05 wt% solution of P36T in anisole, similar to the one prepared by Samitsu *et al.*,[3] at a temperature of 293 K to study the dynamics of fiber formation in a stepwise fashion using coarse-grained simulations. In a first step, diffusive motion of the polymer chain segments is needed to bring them close enough to interact with each other. A stable nanofiber nucleus is formed whenever the number of monomers within the interacting chain segments exceeds the critical number of ~80 and polymer chain aggregation, *i.e.* nanofiber formation, can proceed. If, however, less than roughly 80 monomers interact with each other, the chain segments are ripped apart again by thermal motion.

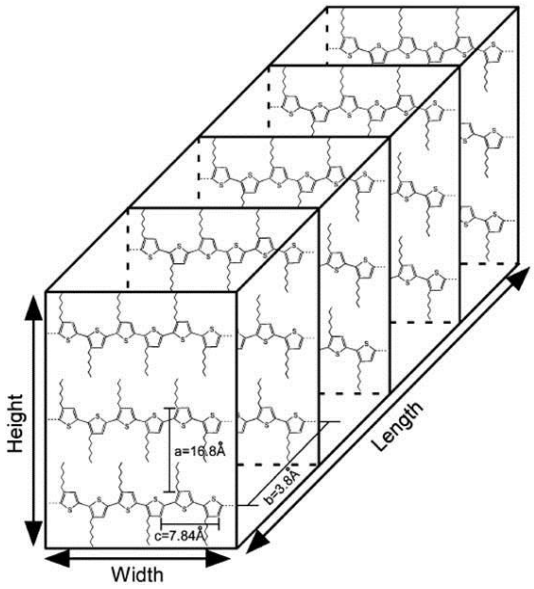

Figure 2.3. Internal polymer chain organization within a P36T nanofiber (Reproduced from Ref. 12, Copyright © 2013 WILEY-VCH Verlag GmbH & Co. KGaA, Weinheim). a, b and c represent the crystalline unit cell dimensions. The fiber height is 4 nm, which is equal to two to three lamellar stacks. The width of about 24 nm corresponds to 60 – 70 monomer units. The length of the fibers is a few micrometers. The polymer chain direction is along the fiber width, while the π-π stacking direction is along the fiber length.

The model therefore revealed a critical aggregate width of ~80 monomers for stable nanofiber formation, consistent with the experimentally determined lower molecular weight boundary. Furthermore, the model confirmed the predominant nanofiber growth along the π-π stacking direction and enabled to determine the inter-lamellar spacing, the π-π stacking distance and the nanofiber width, taking into account a reasonable statistical error. Besides confirming experimentally accessible structural features, the model also provided information that could not be resolved experimentally. Individual polymer chains were found to loop back within the same lamellar plane such that segments of the same polymer chain lie within the same lamella. Because of a certain bending rigidity, they do not enter adjacent π-π stacking planes. Modelling also resolved a certain degree of internal

nanofiber disorder in the form of internal polymer chain loops. Ideally, these loops would only be present at the edges of a nanofiber.

When preparing P36T nanofiber dispersions for the active layer of organic solar cells, the choice/quality of solvent appears to have a large influence on solution stability, as polymer/fiber precipitation was identified for concentrations above 0.05 wt% in cyclohexanone, while this was not the case in *p*-xylene.[2] To use these solutions reliably for OPV active layers, polymer/fiber precipitation should be avoided in the concentration range of 0.5–3 wt%, as otherwise the required active layer thickness of ~100 nm cannot be achieved consistently. As a result, *p*-xylene is preferred as the fiber production solvent.[2]

Although solvent choice is crucial for nanofiber formation, finding one single solvent that suits nanofiber formation for a whole range of P3*A*T seemed rather impossible. Nevertheless, anisole was proven to be suitable for the fiber formation of P3*A*T with *A* = 4, 6, 8 and 10, allowing systematic investigation of the effect of alkyl side-chain length (A) on the formation of nanofibers and their morphological, optical and electrical properties.[3] Regarding the P34T solution, it has to be pointed out that partial polymer precipitation occurred, even at temperatures above 70 °C, due to the limited solubility offered by the shorter side chains. Therefore, the solution had to be filtered, reducing the original polymer concentration. The marginal difference between the Hildebrand solubility parameters $\delta^{\ddagger}$ of each of the polymers and the solvent was in this case held responsible for the compatibility of anisole with fiber formation in solution.[14,15] Although a cooling rate of 25 °C/h was consistently maintained, no tremendous change in nanofiber characteristics was observed when the cooling rate was (drastically) increased. The same holds for varying the polymer concentration, *i.e.* no significant changes were observed within the range of 0.005–0.5 wt%. On the other hand, the polymer regioregularity[‡‡] did influence the fiber formation significantly, as regiorandom P36T failed to form nanofibers.

This was explained by the fact that the random orientation of the alkyl side chains effectively prevents crystallization of the polymer backbones and side chains.[3]

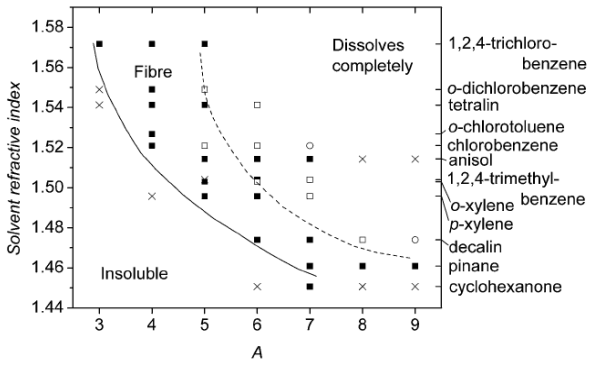

Figure 2.4. Fiber formation in P3*A*Ts (*A* = 3–7) in function of solvent refractive index for 0.3–1 wt% polymer solutions, as observed at room temperature. Indicated are: (x) polymer-solvent combinations that (in the 0.3–1 wt% concentration range), besides fibers, also gave larger precipitates, as observed by UV-Vis; (·) polymer-solvent combinations that gave over 50% fiber formation, and (□) less than 50% fiber formation; (○) combinations that afforded no fibers at all, or less than 5% fibers. Indicated are the approximate solubility limit at room temperature (solid line; 100% fiber formation) and the line of approximately 50% fiber formation (dashed line) (Reproduced from Ref. 4).

Looking beyond nanofiber production, to their integration in the active layers of optoelectronic devices, specific solvent requirements nevertheless have to be taken into account. In view of device preparation, Oosterbaan *et al.* tested fiber formation of P3*A*T in several solvents.[4] They were aiming for a fiber yield of over 50% in the concentration range of 0.3–1 wt% to obtain sufficiently thick active layers, *i.e.* >20 nm, and this without the occurrence of gelation or polymer precipitation. Secondly, for the preparation of solar cells the solvent has to be a good solvent for the fullerene acceptor as well.[16–18] The limited availability of δ values for P3*A*T in the range of A = 3–9 (and even for some solvents) limited the usability of the Hildebrand solubility parameter. It was, however, found that the solvent refractive index, related to the dispersive term δ_D in the Hansen solubility parameter

concept and known for all solvents, could aid in the solvent selection process (Figure 2.4).[4]

During a recent study dedicated to controlling the microstructure of P36T nanofibers, the large impact of solvent quality on the final nanofiber crystalline quality was stressed once again and ascribed to three separate effects.[8] The first effect is polymer fractionation. For a better solvent, only longer (higher molecular weight) chains, which can fold back on themselves upon crystallizing in the (100) direction of the fiber, are incorporated in the nanofibers. As such, the number of chains and chain ends that need to be incorporated to reach the equilibrium fiber thickness of about 5 nm is reduced.[1] The second effect is the increase in the radius of gyration R_g. When using a better solvent, the polymer chains have more freedom to move and find their lowest energy conformation during nanofiber formation, as in this case their interaction with the solvent molecules is more favoured. The third effect controlled by solvent quality is the formation kinetics. The favourable interactions between polymer chains and solvent molecules in a good solvent slow down the polymer chain aggregation kinetics, giving the chains more time to find the lowest possible energy position. The overall result is a decrease in the number of incorporated defects and hence an increase in crystalline quality. Within this study, toluene afforded the highest crystalline quality for a solution containing 0.1 wt% of P36T.[8]

Using toluene as a solvent, P36T nanofibers possessing a high level of intrachain order have been prepared by Niles *et al.*[19] Their internal structure was characterized as being J-type, having side chains adopting an edge-on packing (type I), minimizing the amount of torsional backbone disorder. Photoluminescence (PL) spectroscopy measurements on these J-type fibers revealed a link between temperature and pressure-induced chain repacking and a change in electronic coupling.[20] By increasing the pressure or decreasing the temperature, the hexyl side chains change their packing from edge-on (type I) to interdigitating

(type II) Figure 2.5. This forces the thiophene rings in the polymer backbone to loose their planar conformation and hence increases the amount of torsional and intrachain disorder. Furthermore, the internal fiber structure becomes more H-type[‡‡‡]. This structural reorganization was linked to a red-shifted PL of the well-dispersed nanofibers and a decrease in 0−0/0−1 PL ratio. The transition is, however, reversible since the system returns to its original state whenever the pressure is decreased or the temperature is increased to its initial value. Additionally, using transient absorption spectroscopy (TAS) the ultrafast excited state relaxation and recombination of both excitonic and polaronic species was studied. An order of magnitude difference in relative interchain charge transfer between H and J-type nanofibers was inferred from the ratio of the initial formation of intrachain species, *i.e.* polaron-pairs, to interchain species, *i.e.* delocalized polarons. This effect was solely attributed to a change in intrachain order, which could uniquely be induced in native J-type P36T nanofibers via a temperature or pressure-controlled switch.

Tapping mode AFM measurements were performed to determine the morphology of P3*A*T nanofibers after solution deposition on a SiO_2/Si substrate.[3–7] Fiber lengths were always found to be in the micrometer range, while the cross section of the fibers showed nanometer-sized dimensions. Moreover, for P3*A*T (*A* = 4, 6, 8, 10) fibers produced from anisole, the width and height were found to increase slightly with increasing alkyl chain length (*A*),[3] although another study performed on P3*A*T (*A* = 3–9) nanofibers produced with different solvents could not confirm this correlation.[4] However, quantitatively, the measured values did not really differ much, since in the former study average heights and widths were 3–4 and 24–27 nm, respectively, while in the latter study they were found to be 2–10 and 20 ± 5 nm, respectively.

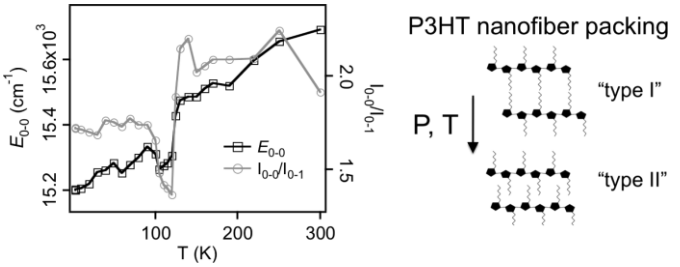

Figure 2.5. Illustration of reversible pressure and temperature-induced changes in the PL spectrum of J-type P36T fibers (left) caused by a change in the side chain packing from type I to type II (right) (Reprinted with permission from Ref. 20; Copyright 2012 American Chemical Society.).

To rule out the possibility that the nanofibers present on the SiO_2/Si substrate only formed during deposition from anisole solution and hence were not present before in solution, UV-Vis absorption measurements were conducted on the heated solutions, on the solutions cooled down to room temperature before and after passing through a 0.20 µm polytetrafluoroethylene (PTFE) filter, and on a thin film of P3*A*T nanofibers deposited on a SiO_2/Si substrate.[3] The absorption spectra of the heated (orange transparent) solutions and that of the filtrate were both similar to the absorption spectra of P3*A*T in chloroform, a good solvent for alkylated polythiophenes. Hence, both the heated solution and the filtrate contained well-dissolved P3*A*T. The spectrum of a thin film of P3*A*T nanofibers resembled that of the cooled solution before filtering. This led to the conclusion that the fibers in the thin films as observed by AFM were already present in solution and did not just form upon solution deposition.[3] Berson *et al.*[2] came to a similar conclusion when comparing the absorption spectra obtained from a film containing P36T nanofibers with the spectrum of a stable P36T nanofiber solution in *p*-xylene.[2]

Information on the crystalline structures of P3*A*T nanofibers was obtained from X-ray diffraction (XRD) patterns and selected area electron diffraction (SAED), revealing a type I crystallographic structure with extended polymer backbones along the c-axis, forming stacks along the

fiber axis or b-axis, and the alkyl chains oriented mainly along the a-axis (Figure 2.3). An exception to the type I structure was found in the structure of P37T, with a small contraction in the a-direction and a small expansion in the b-direction (type I').[4] With the help of the Scherrer equation:

$$\mathrm{FWHM}(2\theta) = \frac{0.9\lambda}{\xi}\cos(\theta) \qquad (2.1)$$

λ is the wavelength of irradiation, ξ the crystallite size, and θ the incidence angle), the coherent domain size or crystallite size along the direction of the fiber lenght, ξ_{010}, and in the fiber height, ξ_{100}, could be extracted from the full width at half maximum (FWHM) of their corresponding peaks in the XRD spectra. For both parameters, an increase was observed with increasing alkyl side chain length *A*, pointing to the importance of the alkyl side chains for stabilization of the nanofibers as to form crystalline structures.[3,4] Concerning the crystalline unit cell dimensions, given in Figure 2.3 for a P36T fiber, *c* = 0.78 nm, as determined by the thiophene ring interspacing, did evidently not change with increasing *A*.[3,4] The same was true for *b* = 0.38 nm, which is the π−stacking distance. A small exception to this was observed in the case of P37T for which *b* = 0.40 nm, correlated with a slightly different crystalline structure for which the alkyl chains become interdigitated, while for the other P3*A*Ts (*A* = 3, 4, 5, 6, 8, 9) the alkyl chains were not interdigitated, as illustrated in Figure 2.3 for a P36T fiber.[4,12] Nevertheless, a linearly increasing *a* with increasing *A* was observed by Samitsu *et al.*[3] as well as Oosterbaan *et al.*[4]

High molecular weight P3*A*T nanofibers coexist in solution with entangled polymer chains, for which a coil-to-rod transformation is hindered. In an attempt to overcome these entanglements, ultrasonication of fiber solutions prior to film deposition was introduced and tested for different molecular weights and sonication times using P36T nanofiber solutions in

p-xylene.[5] After ultrasonication, both the crystalline content of the solution and the crystallinity of its corresponding thin film increased, and large scale amorphous aggregates were no longer present in the films. However, it was most effective for large molecular weight P36T, because of the higher degree of entanglements. Importantly, it did not damage the polymer, as the original nanofiber solution could be re-obtained after re-dissolving and re-formation of the polymer fiber solution. The optimal oscillation time appeared to be 4 minutes, presenting a trade-off between the reduction of chain entanglements and aggregates on the one hand and nanofiber scission, as observed from AFM measurements, on the other hand.

Mixed solvent approach. In the mixed solvent approach a certain amount of a 'bad' solvent is added to a well-dissolved solution of P3*A*T to induce polymer chain aggregation.[21–25] This approach was used by Li *et al.* to improve crystallinity in pure P36T as well as composite P36T:[6,6]-phenyl-C61-butyric acid methyl ester (PCBM) (1:1, w/w) films by forming ordered fiber precursors in solution prior to thin film deposition.[26] They started off with a well-dissolved solution of pure P36T (8.0 mg/mL), either in *o*-dichlorobenzene (ODCB) or chloroform, to which *n*-hexane, a bad solvent for P36T, was slowly added via titration (~ 0.2 mL/min per 1 mL ODCB or chloroform) while gently stirring the solution to avoid local high concentrations of hexane. The optimal hexane:ODCB (v/v) ratio to reach homogeneous thin films during device fabrication appeared to be 1:2. Subsequently, the solutions were aged and only after the desired ageing time PCBM was added and the solution was stirred for another 3 hours to fully dissolve PCBM. Adding hexane induced a colour change of the solution from yellow brown to dark brown accompanied by the appearance of a vibrational structure in the UV-Vis spectrum, related to the formation of P36T nanofiber precursors. The vibrational features became more pronounced with ageing time and stabilized after 18 hours. At this point, precursor formation in solution was considered to be complete and the solution reached an equilibrium

state. Nevertheless, for homogeneous film formation, the ageing time was set at 16 hours. Transmission electron microscopy (TEM) and SAED on thin films spun from aged solutions confirmed the presence of nanofibers with micrometer length and nanometer cross section, enhancing the film crystallinity as compared to the films deposited from solutions without hexane. Although the difference in crystallinity upon adding hexane was much larger when using chloroform as a starting solvent, a significant increase in film crystallinity could still be obtained, even for a slowly evaporating starting solvent as ODCB. This observation was done both for pure P36T as wel as for its composite system with PCBM. For the composite system, the increased crystallinity was additionally confirmed with XRD, revealing an increased (100) diffraction intensity for the films deposited from the aged composite hexane-ODCB solution as compared to the unannealed and annealed (150 °C for 15 min) films from the unaged composite ODCB solution. Therefore, they concluded that their approach was effective in increasing the crystallinity of pure P36T and composite P36T:PCBM films. Adding PCBM only after P36T aggregation was induced, prevented interference of the small PCBM molecules with the self-crystallization of P36T. To test the relevance of this approach for electronic applications, the pure P36T film conductivity was measured using a 2-probe method. Setting out the film conductivity as a function of the solution ageing time revealed a clear increasing trend with an order of magnitude difference between the film spun from a 16 hours aged hexane-ODCB solution and the one from an unaged pure ODCB solution.

The mixed sovent approach was also applied to a well-dissolved P36T solution in chloroform with an initial polymer concentration of 0.0005 wt%. Different solvents were tested, but the non-solvent acetonitrile (MeCN) appeared to be most effective in inducing P36T nanofiber formation. Only 30 vol% of MeCN was sufficient to obtain a strongly red-shifted UV-Vis spectrum with a clear vibrational structure.[27] Grazing incidence X-ray diffraction (GIXRD) measurements on spin-coated films

provided a second confirmation with an increasing (100) and decreasing (010) diffraction intensity. While the former points to a better lamellar stacking, the latter points to more in-plane oriented thiophene rings. The minimum amount of MeCN necessary for fiber formation depends on the polymer concentration and increases when the P36T concentration increases from 0.5 to 1.0 wt%. Nevertheless, adding more than 5 vol% is not beneficial as AFM showed the dominance of large aggregates in the film structure. The optimal amount appeared to be around 3.3 vol% MeCN added to a solution of 0.5, 0.7 or 1.0 wt% P36T. The nanofibers grow larger during long-term storage of the solution (ageing) after adding the non-solvent.

In another case, this approach was applied to produce P36T nanofibers in a P36T:PCBM (1:1) solution at a concentration of 25 mg/mL with the intention of directly using it to form the nanostructured active layer of organic BHJ solar cells.[28] To this end, P36T and PCBM were first dissolved in chlorobenzene (CB) (1 mL) upon stirring for 14 hours under nitrogen atmosphere. Next, cyclohexanone (500 µL) was added to the CB solution and this mixture was aged for 2 hours while stirring. UV-Vis absorption measurements confirmed the formation of nanofibers in solution in the presence of PCBM, while from GIXRD it was deduced that the nanofibers in thin films grew further under mild thermal annealing (for 5 min at 80–100 °C).

Only recently, an excitonic coupling analysis[‡‡‡‡] was conducted on a whole range of P36T aggregates formed in binary solvent mixtures to assess the correlations between the structural order within the P36T aggregates formed and the identity of the poor solvent used to induce aggregation.[29] The authors concluded that an analysis based on the Hansen solubility parameters could not reliably predict the amount of structural order, related to the excitonic coupling, present in the P36T aggregates formed in each binay solvent mixture. To formulate their conclusions on the aggregation processes involved, they had to fall back

on a basic thermodynamic and kinetic analysis of the interactions between the solvent on the one hand and the P36T backbone and side chains on the other hand. The different steps in the aggregation process revealed to be consistent with previously reported theoretical simulations, *i.e.* planarization of the backbone in a first step followed by π−π stacking of the polymer chains to form crystal nuclei.[11] As a final step, the hexyl side chains reorganize. Furthermore, it is pointed out that additional investigations using more rigorous analysis methods are underway to correlate P36T aggregation, excitonic coupling and solvent properties.

Good solvent approach. Under mild conditions and slight oversaturation P36T nanofibers have been shown to grow in solution (0,01 wt% P36T dissolved in refluxing chloroform while stirring).[30,31] The solution was aged in the dark at 20 ± 2 °C for 1 week. Fiber formation in solution was again inferred from a yellow to red colour transition and the appearance of a vibrational structure in the UV-Vis absorption spectrum. Nanofiber dimensions were determined by AFM after deposition on a Si wafer by dipping the wafer in the solution for 1 min followed by dipping in pure chloroform for another minute. This last step ensured that only ordered nanofibers adsorbed from solution were visualized and that well-dissolved P36T, otherwise forming a disordered top layer, is washed away. The nanofiber length was found to be more than 10 µm, whereas their width and height were around 40 and 1.6 nm, respectively. The latter matches the lamellar spacing in P3*A*T nanofibers as measured by Samitsu *et al.*[3] and Oosterbaan *et al.*,[4] confirming that the nanofibers are of monolayer thickness. The whole process of monolayer fiber formation was related to a small oversaturation of the high molecular weight fraction under mild conditions, inducing a slow crystallization process of this fraction, while the lower molecular weight fraction remained well-dissolved. In this way, the slow crystallization rate of the high molecular weight fraction enabled the polymer chains to take on the energetically most favourable position as to obtain thermodynamic stability. The van der Waals interactions between the side chains are in this case not strong enough to overcome the

favourable interactions of the side chains with the chloroform molecules, and consequently fiber growth in the side chain direction does not occur and the fibers remain of monolayer thickness. These monolayered fibers provide an efficient route to study the interplay between the (modified) dielectric surface and the edge-on oriented P36T polymer chains in nanofiber structures, which is observed to be an important factor determining the corresponding FET properties.[31–33]

2.1.2 Electrospinning

In this method, an electric field is applied between a polymer solution and a collector electrode to pull the polymer solution through a micrometer-sized nozzle, forming an elongated solution jet travelling to the collector electrode (Figure 2.6). On its way towards the electrode the solvent evaporates, forcing the polymer chains to pack together, forming a fiber of which the diameter and cross-sectional uniformity depend on the polymer molecular weight and concentration and the electrical conductivity of the solution.[34] A prerequisite for a polymer to be electrospun is that it needs to form enough chain interconnections in solution to make it sufficiently viscous. Without this, it is impossible to form a uniform solution jet upon electrospinning.[34] As a result, studies on regioregular P3*A*T nanofibers produced via electrospinning have been scarce, since its relatively rigid conjugated backbone and the steric hindrance from the alkyl side chains make it somewhat less flexible as compared to *e.g.* polystyrene (PS) and poly(methylmethacrylate) (PMMA) (although persistence lengths are not that different), and therefore somewhat hinder chain interconnection.[35–37] Nevertheless, the lack of viscosity could be compensated for by the fast crystallization inherent to P3*A*T. Unfortunately, fast crystallization appeared to be problematic as well, as it led to frequent blocking of the nozzle during the spinning process, disturbing the uniform solution jet and resulting in the formation of beads along the fibers. This problem was surmounted using a coaxial nozzle to electrospin a concentrated solution (11–13 wt%) of

high molecular weight regioregular P36T (87 kg/mol, 95% regioregularity) dissolved in chloroform at 50 °C.[38] The polymer solution was supplied through the inner nozzle and an additional small amount of chloroform was added through the outer nozzle. As such, the crystallization of P36T could be delayed and this prevented the nozzle from being blocked during the process. With the coaxial nozzle, a continuous solution jet was guaranteed and uniform fibers with average diameters of 500 nm were formed, as revealed by scanning electron microscopy (SEM) images.

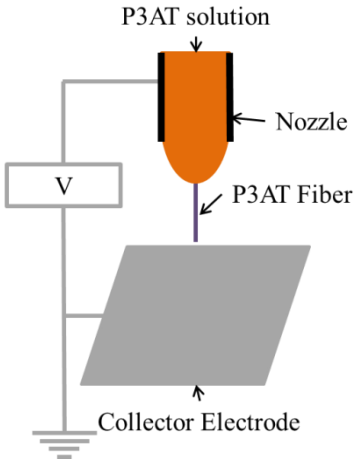

Figure 2.6. Schematic illustration of electrospinning.

Blending P36T with high molecular weight poly(ε-caprolactone) (PCL), which is highly viscous, in various ratios, allowed to produce uniform nanofibers without the use of a coaxial nozzle.[38] Afterwards, PCL could be removed from the fibers by selectively dissolving it with trifluoroethylene (TFE). In this way, connectivity of the P36T phase throughout the nanofibers was revealed. The reason for this is that during electrospinning the isolated P36T domains, originally present in the polymer blend of PCL and P36T, are elongated by the strong shear forces resulting from the high electric field applied, forming short P36T fibrils. Coming out of the nozzle, solvent evaporation drives these fibrils

together, forming an interconnected P36T phase within the mixed-polymer fiber. As an additional advantage, the nanofiber diameter could be further reduced to about 30 nm by selectively removing PCL. Unfortunately, the P36T phase did not retain the same uniformity as the pristine mixed-polymer fiber. So far, for some unspecified reasons, the authors were unsuccessful in their attempts to study the crystalline structure of the fibers using high-resolution transmission electron microscopy (HR-TEM).

The internal structure of the electrospun P36T fibers has, however, been successfully studied using a 10–12 wt% P36T solution in chloroform.[35] The solution was stirred at a temperature of 60 °C to dissolve the polymer completely, followed by 30–45 minutes of resting to initiate gelation, as seen by a colour transformation from red-orange to opaque dark red. Due to this gelation the viscosity becomes high enough to form fibers by electrospinning. Structural analysis with polarized Fourier transform infrared spectroscopy (FT-IR) revealed the polymer chains to be oriented parallel to the fiber axis. During the electrospinning process, the collector electrode was rotated and this was seen to result in a red-shift in the PL spectrum, attributed to a denser packing of the polymer chains due to the added stretching force on the fibers. Polarized PL provided additional proof for the alignment of the polymer chains parallel to the fiber axis, opposite to the fibers produced from self-assembly, where the polymer chains are oriented perpendicular to the fiber axis, as shown in Figure 2.3.

2.2 Current research status and applications

In the context of this work, it is important to highlight that the presence of crystalline P3*A*T nanofibers in the active layer of organic optoelectronic devices has been found critical to reach high performance levels.[39–41] As such the production of P3*A*T nanofibers in a simple and straightforward way via one of the previously mentioned methods opened the way for alternative processing

methods to achieve high crystallinity in optoelectronic devices without (thermal) post-treatment processes. Next, the application of single and discrete sets of nanofibers as well as films of nanofibers, in some cases blended with PCBM, to form the active layer of OFETs and OPV are discussed.

2.2.1 Nanofiber-based organic field-effect transistors

Field-effect transistors based on discrete solution self-assembled P3*A*T nanofibers. Since these type of transistors are hard to make due to a lack of control over the number of deposited nanofibers, the aim of their fabrication was not to commercialize them but rather to study electrical properties of individual nanofibers. Having this said, one of the initial reports on FET structures used for electrical characterization of single and discrete sets of P36T nanofibers was made by Merlo and Frisbie in 2003.[42] For a single P36T nanofiber they found a longitudinal mobility μ_L = 0.06 cm²/Vs and a current modulation I_{on}/I_{off} = 10³. The onset voltage largely increased from -26 to -73 V for successive voltage sweeps, indicative of pronounced interface trap effects associated with a large surface-to-volume ratio. Samitsu *et al.* later on studied the effect of alkyl chain length on the longitudinal mobility of individual P3*A*T (*A* = 4, 6, 8, 10) nanofibers using dilute (0.01 wt%) solutions in an anisole/chloroform (4:1 v%) mixture spun on a SiO_2/Si bottom-gate-bottom-contact (BGBC) FET substrate.[43] The narrow gap of 250 nm between the drain and source electrode was easily bridged by individual nanofibers to form the transistor channel. Values for single P3*A*T fibers varied between μ_L = 0.033 and 0.064 cm²/Vs, comparable to the values obtained by Merlo *et al.*[42] and Bolsée *et al.*[44] Most importantly, μ_L was found to be independent of the alkyl chain length, in accordance with the similar π-π stacking along the longitudinal fiber axis, as outlined in section 2.1.1.[43]

The longitudinal mobility along a P34T nanofiber prepared according to the method developed by Oosterbaan *et al.*[4] was extracted using a conducting atomic force microscope (C-AFM) based transistor setup of which a schematic illustration can be found in Figure 2.7.[44,45] In this

approach, nanofibers were drop-casted from a dilute (0.001 wt%) solution in *p*-xylene onto a SiO_2/Si substrate prepatterned with a 10 nm platinum drain electrode on top of a 2 nm titanium adhesion layer and passivated with a self-assembled monolayer of hexamethyldisilazane (HMDS). The electrode was kept as thin as possible to prevent nanofiber disruption. The $PtIr_5$ tip of the C-AFM was used as a mobile source electrode, allowing careful selection of a single nanofiber having one of its ends in contact with the drain electrode, while the other end lies free on the substrate surface. The free end is then contacted with the C-AFM tip.

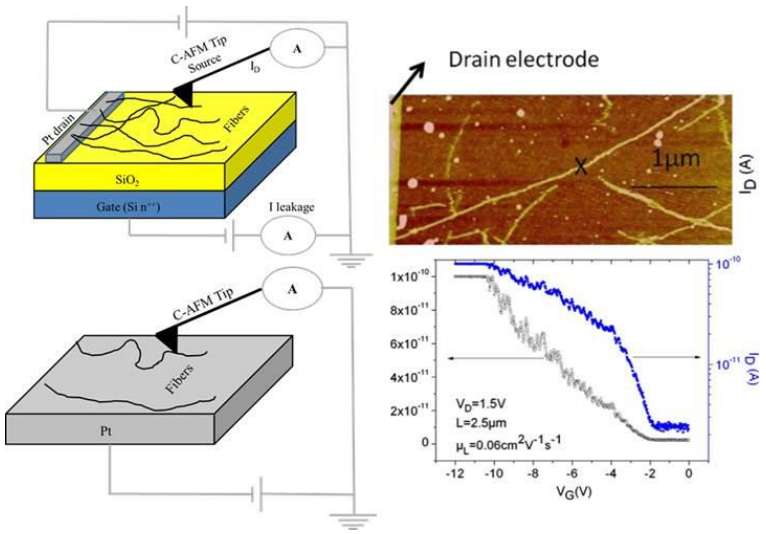

Figure 2.7. Top left: Schematic overview of the C-AFM-based transistor setup. Bottom left: Schematic overview of the sandwich structure used to measure transversal mobility (Reproduced from Ref. 45, Copyright © 2013 WILEY-VCH Verlag GmbH & Co. KGaA, Weinheim. Reprinted from Ref. 44, Copyright 2011, with permission from Elsevier). Right: Topographic image of a P34T nanofiber touching the drain electrode at the left extremity of the image and the transfer characteristic taken with C-AFM at point X from which μ_L is fitted (Reprinted from Ref. 44, Copyright 2011, with permission from Elsevier).

With the C-AFM operating in the spectroscopy mode, the AFM tip remains stationary on the free end of the nanofiber such that transfer and output characteristics of a single P34T nanofiber FET can be measured (Figure 2.7). From the transfer characteristics, the average

longitudinal mobility appeared to be μ_L = 0.07 ± 0.03 cm²/Vs. The similarity with μ_L = 0.06 cm²/Vs obtained by Merlo *et al.*[42] for a single P36T fiber suggested that the longitudinal mobility of P3*A*T nanofibers is independent of the alkyl chain length.[44] This conclusion was consistent with the findings of Samitsu *et al.*[43] The threshold voltage, V_T, was close to zero, so no severe electron or hole trapping took place, indicative of a highly crystalline internal fiber structure.[46] Importantly, this setup allowed to determine the maximum current density the nanowires can withstand, J_{max} = 20 kA/cm².[44,45]

Moving the conducting AFM tip to a position where the nanofiber was on top of the Pt/Ti electrode, a nanofiber sandwich structure was obtained with the tip as the top electrode and the Pt/Ti as the bottom electrode (Figure 2.7). With this sandwich structure current-voltage characteristics in the direction perpendicular to the fiber axis were measured. Fitting these curves with the Mott-Gurney law for space-charge-limited-current (SCLC) transport, the transversal mobility, $\mu_{T,}$ was estimated to be in the range of 10^{-5}–10^{-6} cm²/Vs. Unfortunately, due to a lack of control over the contact force and contact diameter, a better accuracy than one order of magnitude could not be achieved. μ_T decreased with increasing alkyl chain length, which could be related to a reduced charge hopping efficiency from one polymer chain to the other.[44] The thickness of the fiber was independent of the alkyl chain length, ruling out a possible thickness-related decrease of μ_T.[7] Comparing μ_T and μ_L, a large mobility anisotropy was seen with μ_T being 3–4 orders of magnitude smaller than μ_L and depending on the alkyl chain length, whereas μ_L appeared to be alkyl-chain-length independent.[44]

Electrospun discrete nanofiber field-effect transistors. Compared with solution self-assemby methods, electrospinning allowed a much easier selection of a discrete set of nanofibers and therefore this method can be used to produce transistors with an active layer that contains only a discrete set of fibers both for commercial as for research targets. P36T nanofibers produced

via electrospinning have, for example, been used to fabricate single nanofiber FETs with a BGBC[38,47] or a bottom-gate-top-contact (BGTC)[48] configuration (Figure 2.8). The nanofiber FETs presented clear p-channel behaviour under negative gate bias. Device parameters such as field-effect mobility, μ_{FET}, threshold voltage, V_T, and current modulation, I_{on}/I_{off}, were subsequently extracted from the transfer characteristics in saturation. Liu *et al.*[47] found values μ_{FET} = 0.03 cm²/Vs, V_T = 5.5 V and I_{on}/I_{off} = 10^3 in vacuum, while González *et al.*[48] obtained μ_{FET} = 0.0004 cm²/Vs, V_T = 12 V and I_{on}/I_{off} = 7 in vacuum, and Lee *et al.*[38] got μ_{FET} = 0.017 cm²/Vs, V_T = 12 V and I_{on}/I_{off} = 10^2 for devices characterized in air. All of these results are inferior as compared to the best values obtained from P36T thin film FETs, *i.e.* μ_{FET} = 0.1 cm²/Vs and $I_{on}/I_{off} \geq 10^5$.[39,49] The large surface-to-volume ratio facilitates the take-up of oxygen and moisture during electrospinning under ambient conditions, resulting in unintentional doping of the fibers, causing a high I_{off} and positive V_T. The number of interface defects acting as hole scattering sites increases as well and effectively limits the hole mobility.[38,47,48] Nevertheless, devices were fabricated in a straightforward way and the mobility measured by Liu *et al.*[47] approached the μ_L obtained by Samitsu *et al.*[43] and Bolsée *et al.*[44] At this point one may, however, wonder whether the comparison with solution self-assembled nanofibers is justified, since there are indications that the internal structure of both types of nanofibers is different and as such also the optical and electrical properties can be expected to differ.[1,35] For a better understanding and comparison of the optoelectrical properties of electrospun nanofibers, a detailed systematic study on their internal nanostructure like the one in ref. 1 is required.

Single nanofiber-based FETs have also been produced with nanofibers originating from the electrospinning of P36T blended with PCL in different ratios (80:20 and 50:50).[38] All FETs demonstrated clear p-channel behaviour, but their performance degraded with increasing PCL content in the blend. Performance parameters in saturation were μ_{FET} = 0.0012 cm²/Vs, V_T = 16 V, I_{on}/I_{off} = 10 and μ_{FET} = 0.00047 cm²/Vs, V_T = 30 V, I_{on}/I_{off} = 40 for a PCL content of 20 and 50%, respectively. Device

parameters were inferior as compared to pure P36T thin film FETs due to unintentional oxygen doping and uptake of moisture during electrospinning. Furthermore, a higher PCL content in the electrospinning blend interferes more with the crystallization of P36T into large elongated domains, effectively reducing the device performance of the 50% PCL blend. With respect to pure P36T fibers, the incorporation of PCL also introduces an additional interface, accompanied by extra defects within the device.

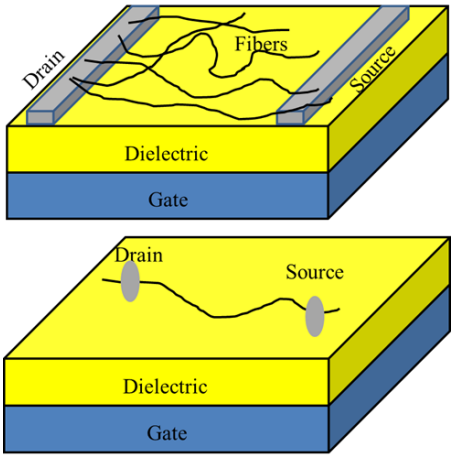

Figure 2.8. Top: Illustration of a BGBC FET for which discrete numbers of fibers are deposited on a pre-patterned substrate. Bottom: BGTC FET setup for single fiber characterization. The fiber is first deposited on the substrate and then the source and drain contacts are applied.

The mixed P36T:PCL fibers were incorporated in a truly flexible FET device fabricated on a gold-patterned methacrylated poly(ethylene terephthalate) (PET) film with a UV-cross-linked hydrogel gate dielectric and a Poly(3,4-ethylenedioxythiophene):poly(styrene sulfonate) (PEDOT:PSS) gate electrode.[50] The number of fibers in the channel could be controlled reasonably well, with a maximum deviation of 2, enabling to extract a linear relationship between the maximum on-current flowing through the device and the number of fibers forming the channel. Under saturation conditions, the average device parameters were $\mu_{FET,Sat}$ = 2

cm²/Vs and I_{on}/I_{off} = 10^5 for devices operating in air. Most importantly, the devices remained stable after a few days of storage under ambient conditions. The improvement in device parameters could only partially be attributed to the large capacitance of the hydrogel gate dielectric. Also here, extra information concerning the internal crystalline structure of the nanofibers would be desirable for further clarification.

Regarding the fabrication of flexible electronic devices, electrospun nanofibers based on blends of P36T/P310T (89/11%, w/w) have shown to be highly compatible with the corresponding roll-to-roll production processes of bendable, rollable or wearable devices that need to withstand multiple stress cycles.[51] Fully flexible FETs were fabricated in an inert atmosphere by depositing a single electrospun nanofiber between gold electrodes on a prepatterned PET substrate, followed by doctor blading of a 1.3 µm thick PMMA gate dielectric and drop casting of a PEDOT:PSS gate electrode. AFM images confirmed that one single nanofiber, with a submicrometer diameter and a smooth homogeneous surface, bridged the gap between the source and drain electrode. By bending the flexible substrate with a bending radius R_b = 5 mm, 28 different FET structures were subjected to a repeated tensile strain in the direction of the charge carrier flow, *i.e.* parallel to the nanofiber longitudinal axis. The magnitude of the tensile strain ε was calculated to be 1.7%, using:

$$\varepsilon = \frac{D}{2R_b} \tag{2.2}$$

with D the substrate thickness. Devices were then characterized before, during and after bending. Neither in the output characteristics, nor in V_T, were significant changes detected. Additional confirmation of device stability could be inferred from the charge carrier saturation mobility in unstressed conditions, showing a slight initial decrease after the first few bending cycles and stabilization after about 100 cycles. Furthermore, the

devices could withstand up to 1000 repeated cycles of bending and relaxing. The observed change in mobility during the first few bending cycles was ascribed to a rearrangement of the conjugated polymer and the PMMA dielectric layer, resulting in a better contacting of the fiber and an improved channel-dielectric interface under influence of the applied tensile stress.

Thin film field-effect transistors. This part deals with transistors that are produced via different solution deposition techniques and which constitute a layer of closely-packed nanofibers, instead of a discrete set. This type of devices can be used both for research as for commercial applications. A large difference between μ_{FET} of nanofiber films and films of well-dissolved P3*A*Ts (*A* = 4–9) has been observed and this has been related to a change in molecular ordering and orientation at the polymer-dielectric interface.[52] On the one hand, μ_{FET} is independent of alkyl chain length for P3*A*T nanofiber (NF- P3*A*T) films, while it decreases with increasing alkyl chain length for films of well-dissolved P3*A*Ts in chlorobenzene (CB- P3*A*T). However, UV-Vis spectroscopy did not reveal any variation in photophysical aggregation, *i.e.* competition of inter- and intrachain exciton interactions, of CB-P3*A*T thin films for various alkyl chain lengths, just as it did not show any difference for NF-P3*A*T thin films.[53] Nevertheless, the crystallinity was generally found to be higher in the NF-P3*A*T films as compared to the corresponding CB-P3*A*T films, except for P34T, for which both layers were found to possess more or less the same crystallinity. The bulk information they obtained from TEM and SAED supported their UV-Vis observations on the similar crystalline structure in all NF-P3AT films. On the other hand, for CB-P3*A*T films, the perpendicular orientation of the thiophene rings relative to the substrate was seen to disappear with increasing alkyl chain length. Polymer orientation at the dielectric-polymer interface was further investigated using near edge X-ray absorption fine structure spectroscopy (NEXAFS), a technique able to determine the average thiophene tilt angle at the interface. For the NF-P3*A*T films, the thiophene rings along the P3*A*T backbone took on a more or less perpendicular (edge-on) orientation relative to the interface, again

independent of the alkyl chain length. This preferred orientation was also present in a CB-P34T film, but it disappeared with increasing alkyl chain length for the other CB-P3*A*T films. Summarizing the results, μ_{FET} was clearly correlated with bulk and interface orientation of the polymer chains, with the latter being largely influenced by the alkyl chain length. Therefore, the connection between alkyl chain length and μ_{FET} seems not to occur through the intrinsic mobility, but rather through an influence of the alkyl chain length on the polymer chain interface orientation.[52] μ_{FET} of NF- P3*A*Ts is insensitive to the alkyl chain length because the well-organized stable internal microstructure is already formed in solution prior to deposition. In a preceding study, the interfacial influence on μ_{FET} was studied by comparing a NF-P3*A*T/SiO_2 interface with an NF- P3*A*T/air interface.[54] Here, the conclusion was that only a small fraction (1.8 to 5%) of wrongly oriented, *i.e.* face-on, P3*A*T chains could still significantly reduce μ_{FET}. In the case of P35T, μ_{FET} was seen to go down one order of magnitude when switching from an air to a SiO_2 interface. These results highlight the importance of interfacial interactions in obtaining high performance P3*A*T FETs.

The effect of alkyl chain length on the FET parameters has also been studied for single layers consisting of interconnected P3*A*T (A = 4–10) nanofibers, having a film thickness comparable to the nanofiber thickness of 3–4 nm.[43] Device parameters were found to be μ_{FET} = 0.01 cm²/Vs, $V_T \sim$ 10 V and I_{on}/I_{off} = 2 x 10^4, for different P3*A*T nanofiber networks, independent of the alkyl side chain length.[3] In comparison with FETs from solutions of well-dissolved P3*A*Ts, μ_{FET} was larger for the nanofiber networks and the difference between the well-dissolved films and the network films increased with increasing side chain length. Hence, the results were consistent with the findings of Oosterbaan *et al.*[52] and indicative of a similar well-ordered internal nanofiber structure with very little defects incorporated. Furthermore, μ_{FET} of a nanofiber network appeared to be 3 to 6 times smaller than μ_L of a single nanofiber FET, suggesting the existence of a transport barrier between the different nanofibers.[43] A higher mobility activation energy E_a for the

fiber network supported this reasoning. E_a was extracted from the Arrhenius behaviour of the mobility versus temperature plots. The alkyl side chains between the different nanofibers are possibly acting as an insulating barrier for the charge carrier transport within a nanofiber network.[43]

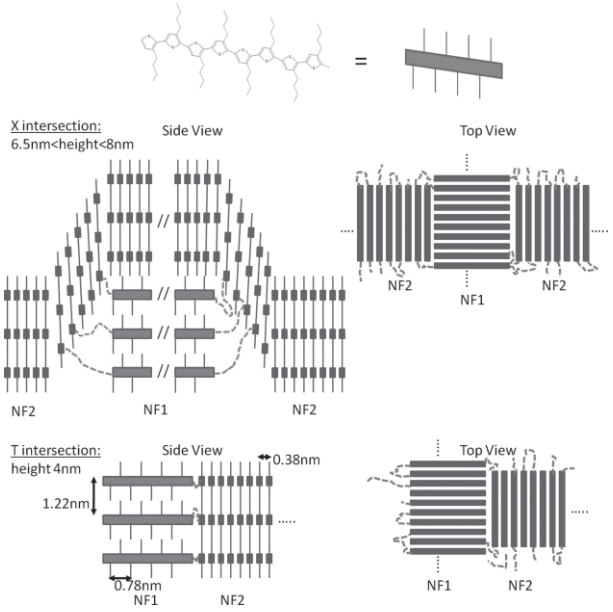

Figure 2.9. Schematics showing the structure of nanofiber bridging points and illustrating the presence of tie-molecules. Dashed lines refer to tie-molecules (Reproduced from Ref. 45, Copyright © 2013 WILEY-VCH Verlag GmbH & Co. KGaA, Weinheim).

The above mentioned μ_{FET} difference between networks and single nanofibers was not observed by Bolsée *et al.*[45] They reported a μ_L = 0.07 ± 0.03 cm²/Vs for a single P34T nanofiber and μ_{FET} = 0.05 ± 0.01 cm²/Vs for a network of P34T nanofibers. Their results were supported by the relation $R_{bp} < 0.1\ R_{nf}$, found between the intrinsic length-dependent nanofiber resistance R_{nf} and the resistance R_{bp} related to an intersection of nanofibers, referred to as a bridging point. This qualitative relation was obtained after numerous C-AFM-based (Figure 2.7) measurements on FETs containing just one bridging point within their channel. Conclusively, R_{bp} was neglected with respect to R_{nf} and the

presence of 'tie-molecules' at nanofiber intersections was held responsible for this (Figure 2.9). These tie-molecules are polymer chains that physically and electrically interconnect different crystalline domains and hence different nanofibers in the case of intersections.[45,54] The following two arguments were in favour of the presence of tie-molecules.[45] First of all, the polydispersity of the polymer used was 2.1, such that a broad range of polymer lengths were present with the longest polymers forming the tie-molecules. Second, the molecular weight of the polymer was higher than the minimum value required for chain folding to occur, such that the polymer chains incorporated in the fibers are either folded or partially extending out of the fiber with the possibility of forming an interconnection with a neighbouring fiber.

Modification of the dielectric surface with a self-assembled monolayer (SAM) of either octyltrichlorosilane (OTS) or HMDS did not improve the performance of nanofiber-based FETs, like it did for FETs of well-dissolved P3*A*Ts.[32,33,56,57] Once more, this results from the stable internal P3*A*T nanofiber structure prior to deposition. Nevertheless, one kept looking for a suitable surface treatment and recently a self-assembled monolayer of perfluorodecyltrimethoxysilane (FAS) effectively improved the performance of P36T nanofiber FETs.[58] With an additional dodecylthiol treatment of the electrode surface, the μ_{FET} of individual nanofibers went up one order of magnitude from 0.056 cm²/Vs to 0.68 cm²/Vs. While the FAS treatment neutralizes charge traps resulting from impurities on the insulator surface and damage generated during sputter deposition, the electrode surface modification leads to a better contact between the Pt electrodes and the nanofibers. To understand the molecular origin of the SAM influence on FET performance, Guo *et al.*[31] deposited their monolayer nanofibers on three different types of modified Si/SiO_2 substrates using the dip-coating procedure. The first substrate possessed a bare SiO_2 surface, while the other two were treated with HMDS and trichloro(1*H*,1*H*,2*H*,2*H*-perfluorooctyl)silane (C_6F_{13}). AFM topography images confirmed the presence of nanofibers on

the C_6F_{13} and SiO_2 surfaces, while they were absent on the HMDS surface. The nanofibers were, however, more abundant on the C_6F_{13} surface. Consequently an increasing attractive interaction between the nanofibers and the surface was observed in the order HMDS, SiO_2 and C_6F_{13}. With the surface energy decreasing in the order SiO_2, HMDS and C_6F_{13}, the observed trend could not be correlated with a decreasing surface energy. Instead, the increased attractive interaction was attributed to the increasing electron-withdrawing ability (in the same order), as confirmed by Raman spectroscopy. This technique showed the presence of a P36T related signal with an intensity going down in the same order as the amount of adsorbed fibers was observed to go down by AFM. Additionally, it uncovered an electron transfer for C_6F_{13}, but not for SiO_2, proposing a stronger attractive interaction for the former. Due to the monolayer thickness of the deposited nanofibers, this technique could now directly assess the interfacial layer between the nanofibers and the FET dielectric and determine its structure and interactions. Since the structure of the interfacial layer is expected to be independent of the nanofiber thickness, the obtained results can be generalized to multi-layered nanofibers.

Regarding the deposition techniques employed to fabricate nanofiber-based OFETs, Bielecka *et al.*[59] compared spincoating with spray-coating and concluded that spray-coated OFET films were inferior as compared to spin-coated films. Their conclusion was based on two observations. First, by examining the UV-Vis spectra and the AFM data of the FET films, a lower crystallinity and shorter fiber length were observed for spray-coated films. Second, hole mobility measurements revealed a certain degree of fiber orientation in the spin-coated films, due to the centrifugal force acting on the nanofibers. As a result, the hole mobility increased whenever the fibers were oriented parallel to the FET channel direction. Fiber orientation was inferred from a bimodal distribution in the mobility histogram extracted from measurements performed on different spin-coated FETs. The lower mobility peak corresponded to a

perpendicular average nanofiber orientation with respect to the FET channel, while the higher mobility peak corresponded to a parallel average orientation. For the spray-coated samples only one peak in the mobility histogram was observed and correlated with no orientational preference.

Kim and co-workers blended preformed P34T nanofibers with different amounts of PS, an insulating polymer possessing excellent mechanical properties.[60] Inherent to their high aspect ratio, the nanofibers only had to make up 0.5 wt% of the total amount of polymer, *i.e.* P34T and PS, to obtain a measurable conductivity in the active FET layer. Below this concentration, the nanofibers were unable to form percolating pathways throughout the PS matrix. An optimal value of 20 wt% of P34T relative to the total polymer amount was found and related to a trade-off between minimizing interfiber boundaries limiting the charge transport and maximizing the number of nanofibers forming the FET channel. However, probably the most important result was the observed increase in environmental stability coming from the protection against unintentional oxygen doping offered by the PS matrix to the incorporated P34T nanofibers. This was seen as a reduction in V_T.

Lu *et al.* studied blends of preformed P34T nanofibers with different amounts of flexbile insulating polymers (PS and PMMA).[61] Particularly focusing on the electrical conductivity of the blend films, they found an 5–8 times improvement in electrical conductivity, from 3×10^{-4}–6×10^{-4} S/cm for pure P34T fiber films to 2×10^{-3}–3×10^{-3} S/cm for P34T-fiber:PS (40:60, w/w) films. Upon increasing the fraction of PS, the conductivity of the blend film became comparable to the pure P34T fiber film at a concentration of 10 wt% P34T. Similar results were observed for fiber blends with PMMA. Since the charge carrier concentration in the fibers was not altered, the increased electrical conductivity could solely be inferred from an increase in charge carrier mobility. Upon increasing the amount of PS in the blend, the dipolar moment of the surrounding environment of each nanofiber decreases and

therefore the charge carrier mobility within the blend increases.[61]

2.2.2 Nanofiber-based organic solar cells

After standard solution deposition via techniques such as spincoating, dip-coating or drop-casting, the active layer blend nanomorphology in an organic photovoltaic cell is often, as in the case of P36T:PCBM active layers, not sufficiently phase-separated and crystalline,[39,63,64] and post-deposition techniques like solvent and thermal annealing have to be applied to improve these features.[65–68] These post-deposition treatments increase the device production costs and complexity and are not always compatible with industrial demands. Thermal annealing, for example, is typically performed at ~140 °C and therefore incompatible with flexible substrates like PET, having a glass transition temperature of ~75 °C. On the other hand, solvent annealing applied on an industrial scale involves risks of intoxication and explosion. These drawbacks can be circumvented by using preformed crystalline organic building blocks, *e.g.* P3*A*T nanofibers. In addition, the P3*A*T nanofibers produced by solution self-assembly possess a diameter comparable to the exciton diffusion length (10–20 nm) in P36T, a low percolation threshold concentration and a high surface-to-volume ratio, making them even more suitable as electron donor materials for the active layer of BHJ OPV. These require an active layer containing one-dimensional charge carrier highways together with a large nanometer-scale donor-acceptor interface. Blends of preformed P36T nanofibers and PCBM were found to be easily processable as active layers, affording a reasonable improvement in PCE without the need for post-deposition annealing. This is a direct consequence of the fibers being already preformed in solution.[2,6,69] A pictorial view of a nanofiber-based BHJ OPV is provided in Figure 2.10.

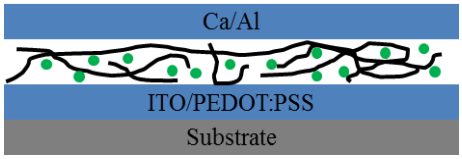

Figure 2.10. Structure of nanofiber-based BHJ OPV with an active layer containing a mixture of P3*A*T nanofibers and PCBM. ITO/PEDOT:PSS serves as a transparant bottom electrode, while Ca/Al serves as a metal top electrode.

From AFM topography and phase images, the addition of PCBM to a P36T fiber solution in *p*-xylene was seen to fill up the gaps present in pristine nanofiber films after deposition on glass. The film root mean square (rms) roughness therefore approached the 11 Å rms roughness of an annealed amorphous P36T:PCBM film. The impact of polymer concentration, P36T-nanofiber:PCBM ratio and percentage of fiber content in solution on OPV performance was systematically investigated by changing one of these parameters at the time.[2] Device performance, as characterized by the J_{SC}, V_{OC}, FF and PCE, was averaged over six different devices. The best performing solar cells were obtained from a 1 wt% solution of P36T-nanofiber:PCBM (1:1.1) in *p*-xylene with a 75% fiber content relative to the total amount of P36T, giving an active layer thickness of around 80 nm. The related six solar cells had an average PCE of 3.6%, much higher than the 0.65% for a (non-annealed) amorphous P36T:PCBM solar cell using the same starting material. Since the V_{OC} did not change much, the improvement could mainly be attributed to an improved J_{SC} due to the presence of nanofibers forming one-dimensional hole pathways and providing a large interface for efficient exciton dissociation. This was confirmed by Douhéret *et al.*[70], who electrically characterized a nanofiber P36T:PCBM blend using high-resolution C-AFM and used it to estimate the local hole mobility in the blend. A small amount of amorphous P36T (25%) nevertheless appeared to be necessary to intimately mix the crystalline nanofibers and the fullerene. The ratio of amorphous versus nanofibrillar P36T in solution was controlled by mixing different amounts of well-dissolved low molecular weight P36T with pure fibers.[2] In another approach, the

temperature dependence of the P36T solubility in a marginal solvent was employed to change the ratio of well-dissolved versus nanofibrillar P36T in solution.[69] In contrast to the method reported by Berson *et al.*,[2] this protocol does not alter the overall molecular weight distribution of the polymer in the final blend, thus eliminating any molecular weight dependence of the OPV performance.[71] Fiber solutions were prepared by dissolving 0.7 wt% of P36T in *p*-xylene at an elevated temperature of 70 °C for 30 min, followed by cooling down to room temperature according to the method proposed by Oosterbaan *et al.*[4] Subsequently, PCBM was added in a 1:1 ratio and the solution was stirred for 48 hours at room temperature to get a good mixing. The solution was heated in a stepwise manner to different temperatures between 37 and 50 °C and left to stabilize at each temperature for 30 min, after which it was spun to form the BHJ OPV devices. The *I*-*V* characteristics were compared at different temperatures and correlated with varying solution nanofiber content via UV-Vis spectroscopy[69], previously confirmed to be a reliable route for fiber content determination in solution.[4] The solution fiber content was seen to change drastically from 60 to 14% when the temperature went up from 37 to 50 °C. However, the PCE followed a rather parabolic trend with a peak at 45 °C, corresponding to a fiber content of 42%. The same trend was observed for J_{SC}, while the V_{OC} increased with temperature and the FF did not show to follow a clear trend as a function of temperature.[68] Using TEM and SAED, the observed trends were correlated with the active layer nanomorphology. At lower temperatures, up to 41 °C, PCBM needles were observed in the active layer and under the influence of Ostwald ripening the larger needles grew at the expense of the smaller ones with increasing solution temperature. With increasing temperature, also an increasing small amount of well-dissolved PCBM was observed in the regions between the P36T fiber needles. Above 41 °C, no needles were observed anymore and a better intermixing of PCBM with the P36T nanofibers was obtained. The improved intermixing leads to more efficient charge carrier separation and hence increased J_{SC} and

PCE. Nonetheless, the decrease in fiber content and the related P36T crystallinity resulted in a J_{SC} and PCE going down above 45 °C because of a reduction in hole mobility. The optimal temperature of 45 °C can therefore be seen as a trade-off between intimate mixing of the active layer components and a good charge carrier transport resulting from sufficient fiber content.[69]

The increase in V_{OC} with decreasing fiber content observed by Bertho *et al.*[69] was further investigated by Vandewal *et al.*[72] and correlated with an increase in the E_{CT} in the P36T-nanofiber:PCBM solar cells. FTPS data were fitted in their low energy part following a procedure developed before by the same group.[73] A mathematical relation between E_{CT} and the P3*A*T fiber mass fraction *f* relative to the total amount of P3*A*T in the blend was found for A = 4, 5 and 6:

$$E_{CT} = E_{CT}^{0} - 0.2f \tag{2.3}$$

valid for $0.1 < f < 0.9$. In addition, V_{OC} correlated with E_{CT} according to:

$$V_{OC} = E_{CT} / q \; - \; 0.6V \tag{2.4}$$

The relation was explained by the shift of the HOMO level of P3*A*T towards the LUMO level of PCBM, which is known to occur with increasing fraction of crystalline P3*A*T in the active layer. Since E_{CT} is directly related to the energy difference between the P3*A*T HOMO level and the PCBM LUMO level, increasing *f* decreases E_{CT} and consequently also V_{OC}.[72]

A different approach was introduced by Li *et al.*, who used the mixed solvent approach to induce P36T nanofiber precursor formation in a composite P36T:PCBM solution in ODCB before the addition of PCBM (as pointed out in section 2.1).[26] The resulting phase segregation in the corresponding thin films took on nanometer dimensions, instead of the micrometer dimensions often observed after post-deposition annealing of

films deposited directly from well-dissolved P36T:PCBM solutions in ODCB. The improved phase segregation control, increased electrical conductivity and increased light absorption were held responsible for the increase in J_{SC} (from 1.47 to 6.00 mA/cm²), FF (from 0.46 to 0.52) and PCE (from 1.08 up to 3.9%) of solar cells fabricated from aged solutions. To verify the reproducibility of their approach, they conducted OPV performance measurements on multiple devices and reported an average PCE of 3.3%. In comparison, a 15 min thermal anneal at 150 °C of devices fabricated using well-dissolved P36T:PCBM solutions in ODCB only yielded an average PCE of 3.1%.

A more or less similar approach towards well-controlled microstructural order in a P36T-nanofiber:PCBM active layer film was proposed by Kim *et al.*[74]. For solvent or thermal annealing after spincoating from a well-dissolved P36T:PCBM solution, it was hard to reach an optimal nanoscale BHJ morphology since P36T crystallization interferes with PCBM aggregation and *vice versa*.[65–68] Therefore, Kim and co-workers introduced a two-step process to separate the fiber formation from PCBM diffusion. This approach effectively prevented interference of the two distinct processes such that each one of them could be effectively directed to reach the optimal final state. The mixed-solvent method was used to directly produce P36T nanofibers in a 2.5 wt% solution of P36T:PCBM (1:1) in chlorobenzene upon adding cyclohexanone. However, nanofiber formation was not yet complete in solution and an additional mild annealing step (after spincoating) was needed to obtain fully developed stable P36T nanofibers. Different temperatures were tested and from GIXRD no further increase in film crystallinity was observed for temperatures above 120 °C. Moreover, even a decomposition of P36T crystalline domains was seen at higher temperatures. TEM confirmed that the additional mild annealing was necessary to obtain well-developed PCBM domains within the nanofiber matrix. More importantly, TEM also confirmed the importance of the two-step process as a whole, since neither the preformed nanofibers nor the

mild thermal annealing could on its own induce sufficient nanoscale phase separation in the P36T:PCBM thin films. The two-step process applied to OPV devices resulted in an increased performance with a PCE going up from 0.79%, for P36T and PCBM well dissolved in chlorobenzene, to 3.76% and 4.04% for the two-step process with mild annealing at 80 and 100 °C, respectively. The OPV performance improvement came mainly from an increase in J_{SC} due to an increase in photoabsorption and a balanced charge transport. The charge transport balance originated from the crystalline P36T:PCBM nanomorphology in the active layer and was confirmed by measuring the hole and electron mobility via the SCLC method (on hole-only and electron-only devices). Due to the presence of charge carrier percolation pathways throughout the active layer, the device layer thickness could be increased from 150 up to 300 nm without compromising the charge carrier collection efficiency.

P36T-fiber:PCBM	Solvent	Thickness (nm)	J_{SC} (mA/cm²)	V_{OC} (V)	FF	PCE (%)	Ref.
1:1.1	*p*-xylene	80	10.0	0.59	0.58	3.4	2
10:8	anisole + 10% CB	110 ± 5	10.13	0.53	0.42	2.29	6
1:1	*p*-xylene	90	9.67	0.61	0.55	3.15	69
1:1	DCM	81	9.51	0.59	0.58	3.23	74
1:1	Tet:Xyl (1:1, v/v)	100 – 120	10.82	0.6	0.52	3.37	76

Table 2.1 Summary of P36T nanofiber-based OPV performance parameters.

As outlined above, after dissolving P3*A*T at elevated temperature in a marginal solvent, nanofiber growth is induced by cooling down the solution to room temperature. After the solution has reached room temperature, it is aged such that nanofiber growth can still proceed. The influence of ageing on OPV performance was studied by Kim *et al.*[74] Blend solutions of P36T nanofibers and well-dissolved PCBM molecules were prepared in dichloromethane (DCM). DCM is a marginal solvent, providing limited solubility for P36T at room temperature, while maintaining a relatively high solubility for PCBM. The solution was aged for different periods of 12–72 hours for which the extent of fiber formation and hence the crystallinity was seen to increase according to a more pronounced vibrational structure and increased absorption in the UV-Vis spectrum. The influence of the ageing time on the photovoltaic performance was then investigated and an optimal period of 60 hours was found. The increase in PCE was correlated with a similar increase in J_{SC}, which on its turn was related to a higher photoabsorption, a more balanced charge carrier transport and higher exciton dissociation efficiency. The increase in photoabsorption could be attributed to the red-shifted enhanced vibrational structure and larger absorption intensity relative to amorphous P36T. Therefore, a better spectral overlap with the solar emission spectrum is obtained. The balance in charge carrier transport, as observed from hole and electron mobility measurements using the SCLC method, was attributed to an increased hole mobility due to a larger degree of π-π stacking and hence a higher level of hole delocalization, inherent to nanofiber formation. Although for an ageing time of 72 hours the nanofibers became even bigger, solar cell performance became worse, explained by an overgrowth of the nanofibers.

In view of the investigation of the relation between the solvent used for nanofiber fabrication and the corresponding solar cell performance, *p*-xylene was compared with anisole, a solvent known to afford highly reproducible results concerning nanofiber fabrication (see section

2.1.1).[6] Although an improvement in crystallinity was observed when switching to anisole, the PCE decreased from 2 to 1.5%. The improved crystallinity resulted in a higher J_{SC} because of a better photoabsorption and higher hole mobility. Unfortunately, however, it also caused a reduction of both the FF and V_{OC}. The former was caused by an imbalance in hole and electron transport, making charge transport space-charge-limited, whereas the latter resulted from a shift of the HOMO level of P36T closer to the LUMO level of PCBM. Despite the lower PCE, the high reproducibility of the results for fibers produced from anisole solutions stimulated further attempts to balance the hole and electron transport. Different small amounts of CB were added to the anisole solution to control the ratio of well-dissolved P36T relative to P36T fibers.[6] The optimal amount of CB was found to be around 10%, as this resulted in the highest crystallinity and also the highest PCE of 2.3%. Adding CB was seen to favourably influence both the J_{SC} and V_{OC} relative to the pure anisole system. The improvement of J_{SC} resulted from a better photoabsorption and hole mobility due to a further increase in crystallinity, while the higher V_{OC} was proposed to result from a better organization of PCBM at the interface with the nanofibers.

Since it was reported that PCBM can easily diffuse to form micrometer-sized aggregates at temperatures well within the operation window of outdoor OPV, research has also focused on the thermal stability of the active layer nanomorphology.[75] In view of this, Li *et al.*[76] applied nanofibers in P36T:PCBM solar cells to obtain a nanoscale phase separation which could withstand a high level of thermal stress. Regioregular P36T was used in a 1:1 ratio with PCBM to obtain a 0.7 wt% solution in a solvent mixture of tetraline (Tet) and xylene (Xyl) in a 1:1 volume ratio. The marginal solvent approach was then applied to obtain P36T fibers thoroughly mixed with well-dissolved PCBM in solution after 5 days of solution ageing. Wide angle x-ray diffraction (WAXD) experiments, UV-Vis absorption spectra and AFM measurements all confirmed the presence of well-developed P36T nanofibers both in

solution and in films. PCBM filled up the gaps in between of the nanofibers in the latter. Compared to films spun from solutions containing well-dissolved P36T:PCBM in either Tet:Xyl (1:1) heated to 70 °C, ODCB or CF, the nanofibers gave (as expected) a higher crystallinity and a larger hole mobility. All samples were then subjected to a thermal annealing at 150 °C for 15 hours to investigate their thermal stability, as deduced from the diffusion of PCBM into micrometer-sized clusters via optical microscopy images. The most stable sample is then the one showing the least and smallest PCBM clusters. Remarkably, the thermal stability appeared to be closely related to the crystallinity of the pristine films prior to annealing. The films prepared from the Tet:Xyl mixture showed the highest stability, inherent to their high crystallinity. Additional confirmation came from comparison of the UV-Vis spectra before and after annealing for 15 hours at 150 °C. The spectra for the films prepared from CF, ODCB and heated Tet:Xyl all showed strong evolution towards a more phase separated structure, *i.e.* P36T crystallization and PCBM aggregation. On the contrary, films prepared from Tet:Xyl solution containing preformed P36T nanofibers did not show any evolution in their UV-Vis spectra, as they were able to retain their internal structure. Inherent to their reduced diffusional mobility, the nanofibers can effectively form a network that can withstand high temperature annealing and confine the PCBM diffusion. Concerning the OPV performance, the P36T nanofiber sample gave a larger PCE of 3.37% as compared to PCEs of 0.51 and 0.98% for the CF and ODCB samples, respectively. In addition, it possessed a higher thermal stability with a PCE decrease to 80% of its initial value after 160 hours at 150 °C. At the same time, the PCEs of the CF and ODCB samples were already strongly degraded to less than 50% of their initial value. Table 2.1 provides an overview of the performance of the P36T nanofiber-based OPV mentioned in this section.

2.3 Notes

‡ The Hildebrand solubility parameter is defined as:

$$\delta = \sqrt{c} = \sqrt{\frac{\Delta H - \mathrm{R}T}{V_{\mathrm{m}}}} \tag{2.5}$$

with c the cohesive energy density determined by the heat of vaporization ΔH, the gas constant R, the temperature T and the molar volume V_m. Since ΔH is the energy needed to vaporize a liquid, c is the amount of energy needed to bring unit volume of molecules from close interaction with neighbouring molecules to infinite separation. This is done by breaking the Van der Waals interactions, when adding energy. The analogy between mixing two liquids and vaporizing a liquid lies in the fact that also upon mixing intermolecular Van der Waals interactions between molecules from one liquid are broken and they are separated from each other by molecules from the other liquid. According to this analogy, mixing between materials will likely occur when the energy needed to separate molecules of both materials is more or less the same. If one of the materials is a liquid, the Hildebrand solubility parameter can be a good indication of the solubility of the other material in the liquid. As such, a polymer and a particular solvent are miscible, whenever their δ values are similar. Following this definition, a solvent will be termed a marginal solvent for a particular polymer whenever there is a small difference in their δ.

‡‡ A regioregular polymer is one in which the monomers are all coupled together in the same head-to-tail manner. How regioregular a polymer is, is expressed by its regioregularity, given as a percentage.

‡‡‡ The difference between the H-type and J-type internal nanofiber structure comes from the way in which the P3*A*T monomers interact with each other. When they interact strongly face-to-face, the internal fiber structure is termed H-type, but when their interaction is strongly head-tail, it is termed J-type (Figure 2.11).

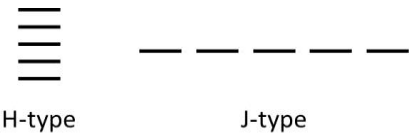

Figure 2.11. Schematic illustration of H-type and J-type monomer aggregation. The black bar represent individual monomers.

‡‡‡‡ An excitonic coupling analysis comes down to determining the excitonic coupling term *J* from the free exciton bandwidth *W* of the P36T aggregates, according to $W = 4J$ and with *W* related to the first and second vibronic transition, A_1 and A_2, in the absorption spectrum of the dispersion containing P36T aggregates according to:[29]

$$\frac{A_1}{A_2} \approx \left(\frac{1 - 0.24 W/E_p}{1 + 0.073 W/E_p} \right)^2 \qquad (2.6)$$

To obtain this relation, the refractive index ratio n_1/n_2 was set equal to 1, just as the Huang-Rhys factor *S* which was also set equal to 1. For P36T the phonon energy of the main intramolecular vibration coupled to the electronic transfer E_p can be set to 0.18 eV. Following this analysis, *J* is positive for $A_1 < A_2$ and the aggregates are called H-type, having a larger degree of internal disorder with respect to the J-type aggregates for which *J* is negative and hence $A_1 > A_2$.

2.4 References

1 K. J. Ihn, J. Moulton and P. Smith, *J. Polym. Sci., Part B: Polym. Phys.,* 1993, **31**, 735.

2 S. Berson, R. De Bettignies, S. Bailly and S. Guillerez, *Adv. Funct. Mater.*, 2007, **17**, 1377.

3 S. Samitsu, T. Shimomura, S. Heike, T. Hashizume and K. Ito, *Macromolecules*, 2008, **41**, 8000.

4 W. D. Oosterbaan, V. Vrindts, S. Berson, S. Guillerez, O. Douhéret, B. Ruttens, J. D'Haen, P. Adriaensens, J. Manca, L. Lutsen and D. Vanderzande, *J. Mater. Chem.*, 2009, **19**, 5424.

5 K. Zhao, L. Xue, J. Liu, X. Gao, S. Wu, Y. Han and Y. Geng, *Langmuir*, 2010, **26**, 471.

6 S. Sun, T. Salim, L. H. Wong, Y. L. Foo, F. Boey and Y. M. Lam, *J. Mater. Chem.*, 2011, **21**, 377.

7 Y. D. Park, S. G. Lee, H. S. Lee, D. Kwak, D. H. Lee and K. Cho, *J. Mater. Chem.*, 2011, **21**, 2338.

8 J. D. Roehling, I. Arslan and A. J. Moulé, *J. Mater. Chem.*, 2012, **22**, 2498.

9 S. Malik, T. Jana and A. K. Nandi, *Macromolecules*, 2001, **34**, 275.

10 S. Malik and A. K. Nandi, *J. Appl. Polym. Sci.*, 2007, **103**, 2528.

11 Y. Takizawa, T. Shimomura and T. Miura, *J. Phys. Chem. B*, 2013, **117**, 6282.

12 J. A. Merlo and C. D. Frisbie, *J. Phys. Chem. B*, 2004, **108**, 19169.

13 K. N. Schwarz, T. W. Kee and D. M. Huang, *Nanoscale*, 2013, **5**, 2017.

14 A. F. M. Barton, in *CRC Handbook of Solubility Parameters and Other Cohesion Parameters*, CRC Press, Boca Raton, 1991.

15 C. M. Hansen, in *Hansen solubility parameters: a user's handbook*, CRC Press, Boca Raton, 2000.

16 R. G. Makitra, R. E. Pristanskii and R. I. Flyunt, *Russ. J. Gen. Chem.*, 2001, **7**, 1229.

17 S. Bertho, W. D. Oosterbaan, V. Vrindts, J. C. Bolsée, F. Piersimoni, D. Spoltore, J. D'Haen, L. Lutsen, D. Vanderzande and J. V. Manca, *Adv. Mater. Res.*, 2011, **324**, 32.

18 M. T. Dang, L. Hirsch, G. Wantz and J. D. Wuest, *Chem. Rev.*, 2013, **113**, 3734.

19 E. T. Niles, J. D. Roehling, H. Yamagata, A. J. Wise, F. C. Spano, A. J. Moulé and J. K. Grey, *J. Phys. Chem. Lett.*, 2012, **3**, 259.

20 T. P. Martin, A. J. Wise, E. Busby, J. Gao, J. D. Roehling, M. J. Ford, D. S. Larsen, A. J. Moulé and J. K. Grey, *J. Phys. Chem. B*, 2013, **117**, 4478.

21 S. D. D. V. Rughooputh, S. Hotta, A. J. Heeger and F. Wudl, *J. Polym. Sci. B: Polym. Phys.*, 1987, **25**, 1071.

22 O. Inganäs, W. R. Salaneck, J.-E. Österholm and J. Laakso, *Synth. Met.*, 1988, **22**, 395.

23 M. M. Bouman, E. E. Havinga, R. A. J. Janssen and E. W. Meijer, *Mol. Cryst. Liq. Cryst.*, 1994, **256**, 439.

24 N. Kiriy, E. Jähne, H.-J. Adler, M. Schneider, A. Kiriy, G. Gorodyska, S. Minko, D. Jehnichen, P. Simon, A. A. Fokin and M. Stamm, *Nano Lett.*, 2003, **3**, 707.

25 A. J. Moulé and K. Meerholz, *Adv. Mater.*, 2008, **20**, 240.

26 L. Li, G. Lu and X. Yang, *J. Mater. Chem.*, 2008, **18**, 1984.

27 Y. D. Park, H. S. Lee, Y. J. Choi, D. Kwak, J. H. Cho, S. Lee and K. Cho, *Adv. Funct. Mater.*, 2009, **19**, 1200.

28 J-H. Kim, J. H. Park, J. H. Lee, J. S. Kim, M. Sim, C. Shim and K. Cho, *J. Mater. Chem.*, 2010, **20**, 7398.

29 C. E. Johnson and D. S. Boucher, *J. Polym. Sci. B: Polym. Phys.*, 2014, **52**, 526.

30 Y. Guo, L. Jiang, X. Ma, W. Hu and Z. Su, *Polym. Chem.*, 2013, **4**, 4308.

31 Y. Guo, X. Ma and Z. Su, *Macromolecules*, 2013, **46**, 2733.

32 S. Kobayashi, T. Nishikawa, T. Takenobu, S. Mori, T. Shimoda, T. Mitani, H. Shimotani, N. Yoshimoto, S. Ogawa and Y. Iwasa, *Nat. Mater.*, 2004, **3**, 317.

33 M. F. Calhoun, J. Sanchez, D. Olaya, M. E. Gershenson and V. Podzorov, *Nat. Mater.*, 2008, **7**, 84.

34 S-H. Tan, R. Inai, M. Kotaki and S. Ramakrishna, *Polymer*, 2005, **46**, 6128.

35 K. H. K. Chan, T. Yamao, M. Kotaki and S. Hotta, *Synth. Met.*, 2010, **160**, 2587.

36 G. Heffner and D. S. Pearson, *Macromolecules*, 1991, **24**, 6295.

37 B. McCulloch, V. Ho, M. Hoarfrost, C. Stanley, C. Do, W. T. Heller and R. A. Segalman, *Macromolecules*, 2013, **46**, 1899.

38 S. Lee, G. D. Moon and U. Jeong, *J. Mater. Chem.,* 2009, **19**, 743.

39 M. Surin, P. Leclère, R. Lazzaroni, J. D. Yuen, G. Wang, D. Moses, J. Heeger, S. Cho and K. Lee, *J. Appl. Phys*., 2006, **100**, 033712.

40 X. Yang, J. Loos, S. C. Veenstra, W. J. H. Verhees, M. M. Wienk, J. M. Kroon, M. A. J. Michels and R. A. J. Janssen, *Nano Lett.*, 2005, **5**, 579.

41 S. S. van Bavel, E. Sourty, G. de With and J. Loos, *Nano Lett.,* 2009, **9**, 507.

42 J. A. Merlo and C. D. Frisbie, *J. Polym. Sci. B: Polym. Phys.*, 2003, **41**, 2674.

43 S. Samitsu, T. Shimomura, S. Heike, T. Hashizume and K. Ito, *Macromolecules*, 2010, **43**, 7891.

44 J. C. Bolsée, W. D. Oosterbaan, L. Lutsen, D. Vanderzande and J. Manca, *Org. Electron.*, 2011, **12**, 2084.

45 J. C. Bolsée, W. D. Oosterbaan, L. Lutsen, D. Vanderzande and J. Manca, *Adv. Funct. Mater.*, 2013, **23**, 862.

46 J. C. Bolsée and J. Manca, *Synth. Met.*, 2011, **161**, 789.

47 H. Liu, C. H. Reccius and H. G. Craighead, *Appl. Phys. Lett.*, 2005, **87**, 253106.

48 R. González and N. J. Pinto, *Synth. Met.*, 2005, **151**, 275.

49 H. Sirringhaus, N. Tessler and R. H. Friend, *Science*, 1998, **280**, 1741.

H. Sirringhaus, P. J. Brown, R. H. Friend, M. M. Nielsen, K. Bechgaard, B. M. W. Langeveldvoss, A. J. H. Spiering, R. A. J. Janssen, E. W. Meijer, P. Herwig, D. M. De Leeuw, *Nature*, 1999, **401**, 685.

50 S. W. Lee, H. J. Lee, J. H. Choi, W. G. Koh, J. M. Myoung, J. H. Hur, J. J. Park, J. H. Cho and U. Jeong, *Nano Lett.*, 2010, **10**, 347.

51 A. Manuelli, L Persano and D. Pisignano, *Org. Electron.*, 2014, **15**, 1056.

52 W. D. Oosterbaan, J. C. Bolsée, A. Gadisa, V. Vrindts, S. Bertho, J. D'Haen, T. J. Cleij, L. Lutsen, C. R. McNeill, L. Thomsen, J. V. Manca and D. Vanderzande, *Adv. Funct. Mater.*, 2010, **20**, 792.

53 F. C. Spano and C. Silva, *Annu. Rev. Phys. Chem.*, 2014, **65**, 477.

54 W. D. Oosterbaan, J. C. Bolsée, L. Wang, V. Vrindts, L. J. Lutsen, V. Lemaur, D. Beljonne, C. R. McNeill, L. Thomsen, J. V. Manca and D. J. M. Vanderzande, *Adv. Funct. Mater.*, 2014, **24**, 1994.

55 R. Noriega, J. Rivnay, K. Vandewal, F. P. V. Koch, N. Stingelin, P. Smith, M. F. Toney and A. Salleo, *Nat. Mater.*, 2013, **12**, 1038.

56 J. C. Bolsée, *PhD Thesis: Macroscopic and nanoscale charge transport in poly(3-alkylthiophene)s: from single nanofiber to semicrystalline thin films*, 2012, (Hasselt: University of Hasselt).

57 M. Arif, J. Liu, L. Zhai and S. I. Khondaker, *Appl. Phys. Lett.*, 2010, **96**, 243304.

58 T. Miki, Y. Murasawa, B. Aronggaowa, Y. Ota, S. Heike, T. Hashizume and T. Shimomura, *Synth. Met.*, 2013, **175**, 200.

59 U. Bielecka, P. Lutsyk, K. Janus, J. Sworakowski and W. Bartkowiak, *Org. Electron.*, 2011, **12**, 1768.

60 F. S. Kim and S. A. Jenekhe, *Macromolecules*, 2012, **45**, 7514.

61 G. Lu, H. Tang, Y. Qu, L. Li and X. Yang, *Macromolecules*, 2007, **40**, 6579.

62 J. M. Verilhac, G. LeBlevennec, D. Djurado, F. Rieutord, M. Chouiki, J. P. Travers and A. Pron, *Synth. Met.*, 2006, **156**, 815.

63 A. Babel and S. A. Jenekhe, *Macromolecules*, 2004, **37**, 9835.

64 G. Li, Y. Yao, H. Yang, V. Shrotriya, G. Yang and Y. Yang, *Adv. Funct. Mater.*, 2007, **17**, 1636.

65 Y. Zhao, G. Yuan and P. Roche, *Polymer*, 1995, **36**, 2211.

66 A. Swinnen, I. Haeldermans, P. Vanlaeke, J. D'Haen, J. Poortmans, M. D'Olieslager and J. V. Manca, *Eur. Phys. J. Appl. Phys.*, 2007, **36**, 251.

67 S. Miller, G. Fanchini, Y. Y. Lin, C. Li, C. W. Chen, W. F. Su and M. Chhowalla, *J. Mater. Chem.*, 2008, **18**, 306.

68 J. Jo, S.-S. Kim, S.-I. Na, B.-K. Yu and D.-Y. Kim, *Adv. Funct. Mater.*, 2009, **19**, 866.

69 S. Bertho, W. D. Oosterbaan, V. Vrindts, J. D'Haen, T. J. Cleij, L. Lutsen, J. Manca and D. Vanderzande, *Org. Electron.*, 2009, **10**, 1248.

70 D. Moerman, R. Lazzaroni and O. Douhéret, *Appl. Phys. Lett.*, 2011, **99**, 093303.

71 W. Ma, J. Y. Kim, K. Lee and A. J. Heeger, *Macromol. Rapid Commun.,* 2007, **28**, 1776.

72 K. Vandewal, W. D. Oosterbaan, S. Bertho, V. Vrindts, A. Gadisa, L. Lutsen, D. Vanderzande and J. V. Manca, *Appl. Phys. Lett.*, 2009, **95**, 123303.

73 K. Vandewal, A. Gadisa, W. D. Oosterbaan, S. Bertho, F. Banishoeib, I. Van Severen, L. Lutsen, T. J. Cleij, D. Vanderzande and J. V. Manca, *Adv. Funct. Mater.*, 2008, **18**, 2064.

74 J. S. Kim, J. H. Lee, J. H. Park, C. Shim, M. Sim and K. Cho, *Adv. Funct. Mater.*, 2011, **21**, 480.

75 X. Yang, J. K. J. van Duren, R. A. J. Janssen, M. A. J. Michels and J. Loos, *Macromolecules*, 2004, **37**, 2151.

76 L. Li, D. L. Jacobs, Y. Che, H. Huang, B. R. Bunes, X. Yang and L. Zang, *Org. Electron.*, 2013, **14**, 1383.

Chapter 3

Theory of organic phototransistors

This chapter deals with the theory of organic phototransistors (OPTs), starting with an introduction providing motivation for studying phototransistors (PTs) instead of photodiodes (PDs) as photodetectors. Followingly, the type of device structure used further on in this work is explained in detail. Finally, the chapter ends with explaining the operation principles of OPTs. A clear distinction is made between gate controlled transistor operation, for which the charge carrier concentration in the channel is controlled by a perpendicularly applied electric field, and the light controlled transistor operation, for which the charge carrier concentration is controlled by the amount of perpendicularly impinging light.

3.1 Introduction

While a PD embodies a photoactive material sandwiched in between two non-injecting metal-semiconductor contacts, a PT possesses injecting source and drain contacts for at least one of the two possible charge carriers, *i.e.* holes and electrons, and an additional third gate contact to apply an electric field perpendicular to the charge carrier channel, allowing one to tune the gain mechanism. As PDs are optimized to work with a reverse applied electric field, they exhibit small dark currents and short charge carrier transit times, which results in a large operating bandwidth, limited primarily by the RC delay[‡] of their equivalent circuit.[1] Unfortunately, due to the non-injecting nature of the PD contacts, the external quantum efficiency (*EQE*), which is the number of charge carriers collected devided by the number of incident photons, cannot be higher than 100%, limiting their light responsive properties. Yet, using the principle of avalanche breakdown, with the application of a large reverse bias, in combination with the photogeneration of charge carriers, *EQE*'s higher than 100% can be reached due to an internal gain mechanism. Nevertheless, this comes at the cost of a large dark current, *i.e.* increased noise level.[1] However, both an *EQE* over 100% and a low noise level can be reached using three-terminal PTs, albeit at the cost of a slightly reduced operation bandwidth due to larger electrode spacing as compared with PDs. Depending on the voltage applied to the gate contact, one can switch between either a photovoltaic or a photoconductive gain mechanism, of which the former allows a high *EQE* and fast switching and the latter allows low noise levels. With this in mind, PTs are more favourable with respect to PD for applications such as opto-isolators, light detectors, optoelectronic switches and organic memory devices, when ultrahigh switching speed is not crucial.[2–6]

At the moment, most practical applications still favour inorganic PTs because of their high performance level. However, the main drawback of inorganic devices comes from their high fabrication cost. In an attempt to reduce this cost, one switched to the vacuum deposition of organic materials to form the active PT layer, allowing the reduction in processing temperature. In spite of

great efforts, the fabrication cost was still high since high vacuum was still needed during the fabrication process.[5,7–10] With the objective of further reducing the fabrication cost, different research groups turned their attention to solution processed OPTs. However, although mechanical flexibility and the ease of coating large areas via solution deposition techniques, *i.e.* spin coating, drop casting, inkjet printing and blade coating, could effectively reduce the device fabrication cost, it is their low performance which limits the ability of solution processed OPTs to compete with inorganic PTs.[11–17] As such, OPTs still need a lot of research before they can become commercially competitive.

In the following sections the device structure and the working principle of the OPTs studied in this work will be introduced, together with the methods of extracting device parameters.

3.2 Device structure

The OPTs studied in this work were fabricated via solution spincoating on BGBC FET substrates (Figure 3.1), of which the dielectric surface was coated with a self-assembled monolayer of HMDS to passivate the bare SiO_2 dielectric by replacing the polar O-Si-OH groups with apolar O-Si-CH_3 groups. Because of its monolayer thickness, the SAM will not change the insulating dielectric properties and device capacitance, it will only change the nature of the semiconductor/dielectric interface in three ways. First, it reduces the concentration of trapped electrons.[18] Second, it promotes edge-on orientation of the thiophene rings along the P36T backbone close to the dielectric interface where the transistor channel is formed.[19,20] Third, it makes the substrate more hydrophobic and therefore less susceptible to environmental humidity. However, the influence of the HMDS monolayer is only significant when a solution of well-dissolved P36T is used to form the active layer. Whenever dispersions of pre-established organic nanostructures are used for OPT fabrication, the influence of HMDS on thiophene ring orientation is reduced, depending on the degree to which the nanostructures are pre-established. As

such, for fully equilibrated solutions, the influence of surface chemistry on device performance becomes negligible.[21]

Thanks to the specific BGBC OPT structure used here, the top side of the transistor is fully accessible. This was particularly interesting for this study since now the charge carrier density could be controlled either via applying a gate voltage to the bottom electrode or via illumination and photogeneration from the top. Both the gate and light or, differently stated, bottom and top control of charge carrier density will be addressed in the following parts of this chapter. Since the source and drain contact are made of gold, the workfunction of the contacts (5−5.2 eV) is close to the HOMO level of P36T (around 5.1 eV) and therefore the barrier for hole injection is negligibly small, enabling the formation of Ohmic contact for hole transport. On the other hand, as the LUMO level of P36T (3 eV) is much lower then the work function of gold, a large barrier, of around 2 eV, prevents the injection of electrons in the active layer.

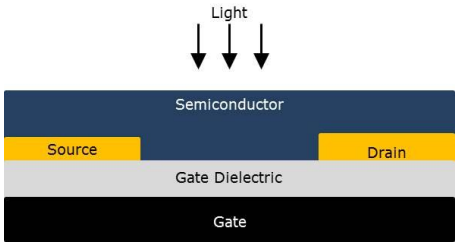

Figure 3.1. Schematic representation of a fiber-based OPT with top illumination as studied within this work. For clarity the HMDS monolayer which is present at the gate-semiconductor interface and the source/drain-semiconductor interface is not shown.

3.3 Phototransistor operation principle

3.3.1 Gate voltage controlled operation

For an organic transistor, the charge carrier concentration in the region close to the dielectric, and with it the current flowing between the Ohmic source and drain contacts, is controlled by the voltage applied to the gate contact. To

prevent short circuiting and obtain the build-up of a vertical electric field, the gate electrode needs to be electrically isolated from the source/drain contacts and the active device layer via the gate dielectric. Figure 3.2 illustrates FET operation with different voltage applied to the gate V_{GS} and drain V_{DS} and with the source grounded. With V_{DS} = 0 V, the device acts as a capacitor, for which the free charge carrier concentration in the region close to the dielectric is exclusively controlled by V_{GS} (Figure 3.2 (a) and (b)). When V_{GS} < 0 V, positive charge carriers will be attracted and wil start to fill up the charge trap states. Therefore, the free charge carrier density in the channel region remains rather low until V_{GS} becomes more negative then the threshold voltage V_T, which is defined as the V_{GS} at which a conduction channel is formed. From then on all the holes attracted to the dielectric interface contribute to the total free charge carrier density as the trap states are completely filled (Figure 3.2 (c) and (d)). The free hole density p per unit area in the channel is then given as:

$$p = C_0(V_{GS} - V_T) \tag{3.1}$$

Applying V_{DS} < 0 V, holes are injected at the source contact and collected at the drain contact. With $(V_{GS}\text{-}V_T)<V_{DS}<0$, the device operates in the linear regime, where the charge carrier concentration and the conductance are varying linearly with V_{GS}(Figure 3.2 (e)). The current I_D flowing through the device, can then be modelled according to:[22]

$$I_D = \mu_{FET,lin} C_0 \frac{W}{L}(V_{GS}\text{-}V_T)V_{DS} \tag{3.2}$$

With further reducing V_{DS} to $V_{DS}<(V_{GS}\text{-}V_T)< 0$ at fixed V_{GS}, the device enters the saturation regime with the formation of the a depletion zone near the drain contact which pinches off the channel (Figure 3.2 (f)). I_D becomes independent of V_{DS} and can be modelled according to:[22]

$$I_D = \mu_{FET,sat} C_0 \frac{W}{2L}(V_{GS}\text{-}V_T)^2 \tag{3.3}$$

In both the above equations W and L represent the device width and length, $\mu_{FET,lin}$ is the field-effect mobility measured in the linear regime, while $\mu_{FET,sat}$ represents the field-effect mobility measured in saturation. C_0 is the capacitance per unit area.

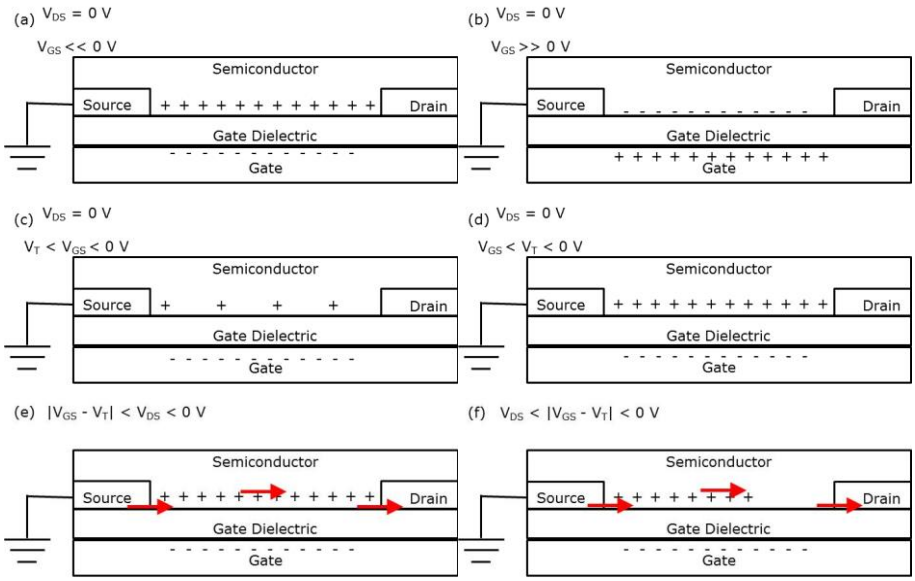

Figure 3.2. Illustration of FET operation. (a) and (b) Without any voltage applied to the drain, the device acts as a capacitor, with the charge carrier density in the channel region fully controlled by V_{GS}. (c) and (d) illustrate the physical meaning of V_T. (e) and (f) illustrate current conduction in the linear and saturation regime, respectively. + and – indicate free holes and electrons. To keep things clear and simple, trapped charges are not shown.

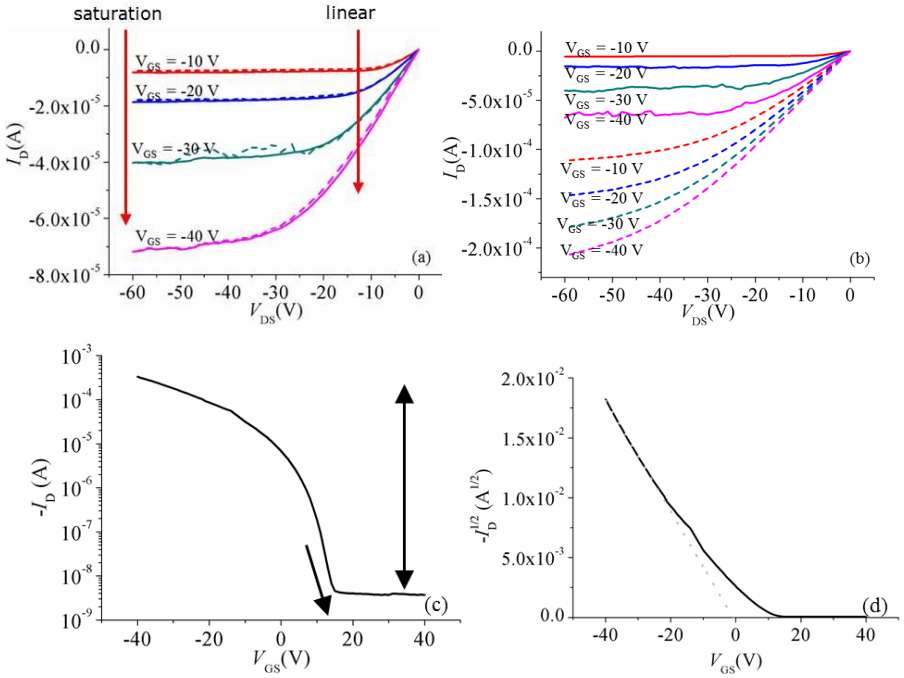

Figure 3.3. Output curves of a fiber-based OPT measured in the dark obtained at different applied gate voltages, both for V_{DS} swept from 0 V to -60 V (full curves) and from -60 V to 0 V(dashed curves). (b) Output curves of the same fiber-based OPT as in (a) measured under dark conditions (full curves) and under an impinging light intensity of 18 mW cm^{-2} (dashed curves), with V_{DS} swept from 0 V to -60 V. Saturation transfer characteristics of a fiber-based OPT measured in the dark with V_{DS} = -60 V and plotted as either $-I_D$ versus V_{GS} in (c) or $(-I_D)^{1/2}$ versus V_{GS} in (d). V_{on} and I_{on}/I_{off} are indicated in (c) with a single and double arrow, repectively. The dotted line in (d) represents the linear fit from which V_T and $\mu_{FET,sat}$ are extracted. The measured OPT had a length L = 10 µm and a width W = (20 mm x SC), with SC the surface coverage.

Both linear and saturation operation are demonstrated in the output characterics ($I_D - V_{DS}$) of a nanofiber-based transistor (Figure 3.3 (a)). When comparing forward (0 V to -60 V) and backward (-60 V to 0 V) V_{DS} sweeps, negligible hysteresis I observed and therefore trapping of holes can be neglected. Throughout this work, V_{DS} was set to -60 V, in order to operate our devices in saturation for which the drain current is maximized. Transistor saturation parameters, $\mu_{FET,sat}$ and V_T, were extracted by fitting the linear part of the saturation transfer characteristics ($I_D - V_{GS}$), plot as $(-I_D)^{1/2}$ versus V_{GS}

in Figure 3.3 (d). The transistor onset voltage V_{on}, defined as V_{GS} were I_D starts to increase, and the ratio of the on-state current to the off-state current I_{on}/I_{off} are determined from a plot of $-I_D$ versus V_{GS} (Figure 3.3 (c)). Good FET operation requires a high $\mu_{FET,sat}$ and I_{on}/I_{off}, V_{on} as close as possible to 0 V and a small $|V_T\text{-}V_{on}|$, resembling a small charge trap density.

3.3.2 Light controlled operation

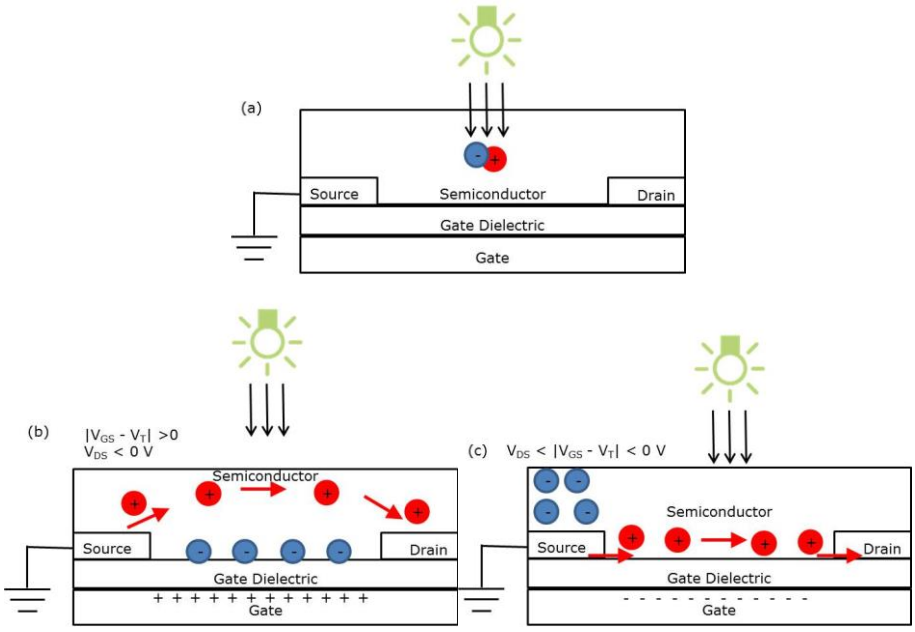

Figure 3.4. Illustration of OPT operation. (a) Charge carrier photogeneration in the active layer in absence of any applied voltages. Transport of photogenerated charge carriers in an OPT operated in its off-state (b), for which the photoconductive effect is dominant, and its saturation on-state (c), for which the photovoltaic effect is dominant. + and – indicate holes and electrons.

In the next part, the influence of an incident white light beam on the fiber OPT operation is considered. As already explained in section 1.4, the events taking place in organic semiconductors upon white light irradiation are photoabsorption, exciton photogeneration and exciton splitting in free charge carriers, of which the latter is largely controlled by the applied voltages in case

of a phototransistor. The creation of charge carriers upon light absorption in an OPT is illustrated in Figure 3.4 (a). Just like V_{GS}, an incident light beam can fully independently modulate I_D, as illustrated in Figure 3.5, showing clear saturation and linear regime operation for an OPT operated with V_{GS} = 0 V and an impinging light intensity of 18 mW cm^{-2}. Compared with Figure 3.3 (a), an impinging light intensity of 18 mW cm^{-2} can be considered as a gate voltage somewhat higher then -40 V applied in dark. The output curves of Figure 3.3 (a) with V_{DS} swept from 0 V to -60 V are given under dark conditions and under an impinging light intensity of 18 mW cm^{-2} in Figure 3.3 (b) showing that the influence of the impinging light beam is maintained under different applied V_{GS}. Depending on the applied gate voltage, different operation mechanisms dominate the photocurrent $I_{D,photo}$ generation in a phototransistor.[23–26] $I_{D,photo}$ is defined as the difference between $I_{D,light}$ and $I_{D,dark}$, the drain currents under light and dark conditions, respectively:

$$I_{D,photo} = I_{D,light} - I_{D,dark} \tag{3.4}$$

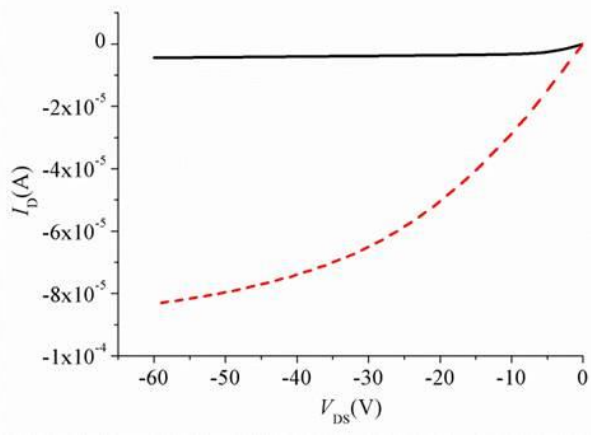

Figure 3.5. Output curves of a fiber-based OPT measured at a fixed gate voltage (V_{GS} = 0 V) obtained under dark conditions (full line) and under an impinging light intensity of 18 mW cm^{-2} (dashed line).

For inorganic transistors working in their on-state, *i.e.* $|V_{GS}|>|V_T|$, the photovoltaic effect dominates $I_{D,photo}$ generation and the following relation holds:[24]

$$I_{D,photo,pv} = G_M \Delta V_T = A \frac{k_B T}{q} \ln\left(1 + \frac{\eta q \lambda P_{inc}}{I_{e,Dark} \hbar c}\right) \quad (3.5)$$

for which, $G_M = dI_D/dV_{GS}$ represents the device transconductance, ΔV_T represents a V_T shift, A is a fitting parameter, k_B is the Boltzmann constant, T is the operating temperature, q is the elementary charge, λ is the wavelength of the incident light, which can here be assumed to be the center wavelength of the lamp spectrum λ_c, η is the external quantum efficiency, $I_{e,Dark}$ is the dark electron current, ħ denotes Planck's constant and P_{inc} indicates the incident light power, which is determined as the product of the incident light intensity I_{inc} and the active device area W x L. Throughout the rest of this work, $I_{D,photo}$ generated predominantly by the photovoltaic effect will be designated as $I_{D,photo,pv}$. Since source and drain contacts are designed to inject only majority carriers, the origin of the photovoltaic effect has been ascribed to the trapping of minority carriers in the active layer near the source contact.[3,4,27,28] Furthermore, following the first equality in (3.5), the minority carrier trapping is correlated with a shift in V_T as given by ΔV_T. The photovoltaic effect is illustrated for an OPT in Figure 3.4 (c).

For inorganic transistors working in their off-state, *i.e.* $|V_{GS}|<|V_T|$, the $I_{D,photo}$ generation is dominated by the photoconductive (PC) effect and the following relation was seen to hold:[29]

$$I_{D,photo,pc} = BP_{inc} = \left(q \mu_p p E\right) WD \quad (3.6)$$

In (3.6), B is a fitting parameter, μ_p represents the hole mobility which can in this work be set equal to $\mu_{FET,Sat}$, p is the hole concentration, $E = V_{DS}/L$ is the lateral electric field in the OPT and D the absorption depth of the active layer. The photocurrent predominantly generated by the PC effect will be referred to as $I_{D,photo,pc}$. Physically, this means that the majority of photogenerated holes are flowing in the bulk of the active layer, away from the channel region where the potential reaches a minimum. Compared with normal photoconductors, in a phototransistor the generation of charge carrier is largely assisted by the

splitting of photogenerated excitons under the influence of the applied perpendicular electric field, controlled by V_{GS}.[28,29] Figure 3.4 (b) illustrates the photoconductive effect for an OPT.

The figures of merit for a phototransistor are the photoresponsivity R and photosensitivity P:[28]

$$R = \frac{I_{D,photo}}{P_{inc}} = \frac{I_{D,light} - I_{D,dark}}{P_{inc}} \tag{3.7}$$

$$P = \frac{I_{D,photo}}{I_{D,dark}} = \frac{I_{D,light} - I_{D,dark}}{I_{D,dark}} = \frac{I_{D,light}}{I_{D,dark}} - 1 \tag{3.8}$$

$I_{D,photo}$ denotes the generated photocurrent under white light illumination, $I_{D,light}$ and $I_{D,dark}$ are the drain currents under light and dark conditions, respectively, and P_{inc} is the incident light power. The latter is determined by the product of I_{inc} and the active device area, defined as $W \times L$. Following their definition, P is actually the signal-to-noise ratio of an OPT and R is a measure of the electrical output $I_{D,photo}$ with respect to the optical input P_{inc}. Therefore, R is also referred to as the input−output gain of the OPT. According to its definition R depends on the wavelength-dependent external quantum efficiency $\eta(\lambda)$ for each wavelength λ in the emission spectrum of the light source. Good performing OPT require both a high R and P value. Since both are varying with V_{GS} for a specific V_{DS}, their maximum values at fixed V_{GS} and V_{DS} will be reported. As will be explained later on, R reaches a maximum when the OPT is operated in its on-state, while P reaches a maximum when the OPT is turned off.

3.4 Notes

‡ The resistive-capacitive delay (RC delay) of an electronic circuit refers to the delay experienced by the signal being processed by the circuit. The amount of delay is determined by the RC time constant, which is the product of the internal resistance R and capacitance C of the circuit.

3.5 References

1 a. J. M. Liu, *Photonic Devices*, 2005, (New York: Cambridge University Press), 926−1017.
b. B. E. A. Saleh and M. C. Teich, *Fundamentals of Photonics*, 1991, (New York: John Wiley & Sons, Inc), 644−696.

2 J. C. Campbell, *Semiconductors and Semimetal*, 1985, vol 22D, Ed W. T. Tsang (New York: Academic).

3 A. J. Seeds and A. A. A. de Salles, *IEEE Trans. Microwave Theory Tech.*, 1990, **38,** 577.

4 M. A. Romero., M. A. G. Martinez and P. R. Herczfeld, *IEEE Trans. Microwave Theory Tech.*, 1996, **44,** 2279.

5 T. P. I. Saragi, R. Pudzich, T. Fuhrmann and J. Salbeck, *J. Appl. Phys. Lett.*, 2004, **84**, 2334.

6 K. J. Baeg, M. Binda, D. Natali, M. Caironi and Y. Y. Noh, *Adv. Mater.*, 2013, **25**, 4267.

7 Y. Y. Noh, D. Y. Kim, Y. Yoshida, K. Yase, B. J. Jung , E. Lim and H. K. Shim, *Appl. Phys. Lett.*, 2005, **86**, 043501.

8 Y. Guo, C. Du, C. Di, J. Zheng, X. Sun, Y. Weng, L. Zhang, W. Wu, G. Yu and Y. Liu, *Appl. Phys. Lett.*, 2009, **94**, 143303.

9 Q. Tang, L. Li, Y. Song, Y. Liu, H. Li, W. Xu, Y. Liu, W. Hu and D. Zhu, *Adv. Mater.*, 2007, **19**, 2624.

10 T. P. I. Saragi, J. Londenberg and J. Salbeck, *J. Appl. Phys.*, 2007, **102**, 046104.

11 S. R. Forrest, *Nature*, 2004, **428**, 911.

12 A. J. Heeger, *Angew. Chem. Int. Ed.*, 2001, **40**, 2591.

13 A. Facchetti, M. H. Yoon and T. J. Marks, *Adv. Mater.*, 2005, **17**, 1705.

14 B. Crone, A. Dodabalapur, Y. Y. Lin, R. W. Filas, Z. Bao, A. LaDuca, R. Sarpeshkar, H. E. Katz and W. Li, *Nature*, 2000, **403**, 521.

15 Z. Bao, *Semiconductive Polymers*, 1999, Eds B. Hseih, Y. Wei and M. E. Galvin (Washington, DC: American Chemical Society).

16 R. M. Meixner, H. Göbel, Yildirim, W. Bauhofer and W. Krautschneider, *Appl. Phys. Lett.*, 2006, **89**, 092110.

17 N. Marjanovic, Th. B. Singh, G. Dennler, S. Gunes, H. Neugebauer, N. S. Sariciftci, R. Schwödiauer and S. Bauer, *Org. Electron.*, 2006, **7**, 188.

18 L. L. Chua, J. Zaumseil, J. F. Chang, E. C. W. Ou, P. K. H. Ho, H. Sirringhaus and R. H. Friend, *Nature*, 2005, **434**, 194.

19 H. Sirringhaus, N. Tessler and R.H. Friend, *Synth. Met.*, 1999, **102**, 857.

20 C. D. Dimitrakopoulos and P. R. L. Malenfant, *Adv. Mater.*, 2002, **14**, 99.

21 Y. Wu, P. Liu, B. S. Ong, T. Srikumar, N. Zhao, G. Botton and S. Zhu, *Appl. Phys. Lett.*, 2005, **86**, 142102.

22 S. M. Sze, *Physics of Semiconductor Devices*, 1981, (New York: Wiley), p 438.

23 G. Horowitz, R. Hajlaoui, R. Bourguiga and M. Hajlaoui, *Synth. Met.*, 1999, **101**, 401.

24 Y. Takanashi, K. Takahata and Y. Muramoto, *IEEE Trans. Electron Devices*, 1999, **46**, 2271.

25 H. Yamamoto, K. Taniguchi and C. Hamaguchi, *Jpn. J. Appl. Phys.*, *Part 1*, 1996, **35**, 1382.

26 W. Zhang, M. Chan and P. K. Ko, *IEEE Trans. Electron Devices*, 2001 **47**, 1375.

27 K. S. Narayan and N. Kumar, *Appl. Phys. Lett.*, 2001, **79**, 1891.

28 M. C. Hamilton, S. Martin and J. Kanicki, *IEEE Trans. Electron Devices*, 2004, **51**, 877.

29 S. M. Sze, *Physics of Semiconductor Devices*, 1981, (New York: Wiley), p 744.

Chapter 4

Poly(3-hexylthiophene) nanofiber-based phototransistors

This chapter deals with the production of P36T nanofiber containing solutions following the marginal solvent approach and the dimensional characterization of deposited P36T nanofibers used for the fabrication of OPT. First, the OPT were tested for their normal OFET performance, revealing an expected surface coverage (*SC*) dependent performance. With photoresponsivity *R* and photosensitivity *P* reaching, 250 A W^{-1} and 6.8 x 10^3 under white light illumination, respectively, the best nanofiber OPT outperform the OPT fabricated from a solution of P36T in chlorobenzene (CB) not containing any preformed fibers. The better performance is attributed to a longer exciton diffusion length, higher charge carrier mobility and an overall increase in the amount of light absorbed. Finally, inherent to an intrinsic gate-tuneable gain mechanism, changing the gate potential reveals an adjustability of the responsivity *R* according to the incident light intensity.

4.1 Introduction

Nowadays, the electronics industry is largely dominated by inorganic PTs because of their high performance level with *R* reaching 400 A W^{-1}.[1–4] Unfortunately, their high performance brings along a high fabrication cost and many research groups have tried to reduce this cost. First, one has switched to the vacuum deposition of organic materials to form the active PT layer, allowing the reduction in processing temperature. Despite great efforts, the fabrication cost was still high since high vacuum was still needed during the fabrication process.[5–9] Targetting a further reduction in the fabrication cost, different research groups turned their attention to solution processed OPTs. However, although mechanical flexibility and the ease of coating large areas via solution deposition techniques, *i.e.* spin coating, drop casting, inkjet printing and blade coating, favor the reduction in device fabrication cost, their low performance limits their ability to compete with inorganic PTs.[10–16] Narayan *et al.* reported $P \sim 100$ and $R \sim 1$ A W^{-1} for a P38T based OPT, while Hamilton *et al.* reported $P \sim 10^3$ and $R \sim 0.7$ A W^{-1} for an OPT based on a F8T2 ([poly(9,9-dioctylfluorene-*co*-bithiophene)]) copolymer.[17,18] While in both these reports the illumination of the devices was conducted with a white light source, Hamilton *et al.* succeeded in further increasing *R* up to ~10 A W^{-1} using a monochromatic light source at a wavelength corresponding to the maximum absorption of the copolymer used.[19] Xu *et al.* studied the light responsive properties of an OPT based on the photoluminescent conducting 2,5-bis(dibutylaminostyryl)-1,4-phenylene-*b*-alkyne-*b*-1,4-bis(2-ethylhexyl)-benzene terpolymer (BAS-PPE). With a 4 µW light beam shining from the top on a coplanar OFET structure, they calculated $P \sim 6000$ and $R = 5$ A W^{-1}.[20] In line with *P* and *R* reported by Narayan *et al.* for a P3OT based OPT, Deen *et al.* presented maximum values of 104 and 160 mA W^{-1} for respectively *P* and *R* under the influence of a 1.7 mW cm^{-2} incident white light beam.[21] An interesting approach towards better light responsive properties for OPTs was proposed by Marjanovic *et al.*, who exploited the concept of a bulk heterojunction to improve the photoresponsivity of their n-type OPT. As such, instead of using pure PCBM for their device active layer, they blended PCBM

with MDMO-PPV in a 1:4 ratio. Despite of having a built-in potential difference between the PCBM and the MDMO-PPV, which was expected to enhance light induced charge carrier generation, their obtained R = 5 A W^{-1} for an incident 100 mW cm^{-2} white light beam remained uncompetitive with respect to inorganic PTs.[16] Dong *et al.* studied OPT based on TA-PPE and found maximum values of R and P equal to 0.36 mA W^{-1} and 3300, respectively, for devices characterized in air without any bias applied to the gate and 5.76 mW cm^{-2} white light irradiation.[22] In their work Pal *et al.* described P36T-based OPTs with an active layer dropcasted from a 0.5 wt% solution of P36T in either *p*-xylene, ODCB or CF on an OTS modified SiO_2 substrate surface, followed by 15 min thermal annealing at 130 °C.[23] With P as high as 3.8 x 10^3 and R as high as 250 A W^{-1}, the *p*-xylene solution gave the best results under a low level of white light illumination (≤ 51 mW cm^{-2}). From the absorption spectra of the three different films the better performance was attributed to a higher level of layer crystallinity obtained when drop casting from the *p*-xylene solution.

In the following sections a systematic study of P36T nanofiber-based phototransistors is performed starting with the production of P36T nanofiber containing solutions and the subsequent dimensional characterization of individual nanofibers. Followingly, nanofiber-based OPT are fabricated using these solutions and their active layer morphology is studied with AFM. Next, the FET performance of the phototransistors was evaluated based on the values obtained for μ_{FET}, I_{on}/I_{off}, V_T and $|V_T-V_{on}|$. Finally, this section ends with evaluating the real photoFET performance based on their performance parameters, P and R. The performance of P36T nanofiber-based OPTs will be compared with reference OPTs made from a solution which did not contain any preformed fibers (solution 1 in Table 4.1) and previously reported OPT performances.

4.2 Nanofiber production and characterization

To start off the practical work, four different solutions of P36T (M_n = 32.3 kg mol^{-1}, PDI = 2.2, RR = 96%, Rieke Metals), in either chlorobenzene (CB) or *p*-

xylene as a solvent, were prepared. To obtain the solution in CB, 20 mg of P36T was added to 2 ml of CB and the solution was stirred overnight in a N_2 atmosphere at room temperature (25 °C). For the solution in *p*-xylene, the marginal solvent approach was applied to yield P36T nanofibers in coexistence with well-dissolved P36T.[24] In this approach, 0.25 wt% of P36T was first dissolved in *p*-xylene in a N_2 atmosphere at elevated temperature (65 °C) and then slowly cooled down to room temperature (25 °C) as to initiate nanofiber formation. Afterwards, the solution was stored for one week in a dark N_2 environment to let fiber growth proceed and reach completion.

The UV-Vis absorption spectra of the P36T solution in CB and *p*-xylene obtained after one week of storage in a dark N_2 environment are given in Figure 4.1 (a). As the spectra did not evolve anymore throughout further storage, both solutions had reached a stable equilibrium and fiber formation in the *p*-xylene solution was complete.[24] While the spectrum of the solution in CB was composed of only one single absorption peak at λ = 457 nm, typical for the π-π* transition of well-dissolved P36T chains, the spectrum of the solution in *p*-xylene, on the contrary, was composed of a single H-aggregate absorption band having a vibrational finestructure with three different absorption peaks, typically around λ = 525, 550 and 610 nm and an additional shoulder at λ = 457 nm. From these features it was concluded that, by comparing with previous studies,[24–30] the solution contained a large amount of crystalline nanofibers in coexistence with a smaller amount of well-dissolved P36T. AFM measurements revealing the presence of nanofibers after solution deposition additionally supported this conclusion (Figure 4.1 (b)).

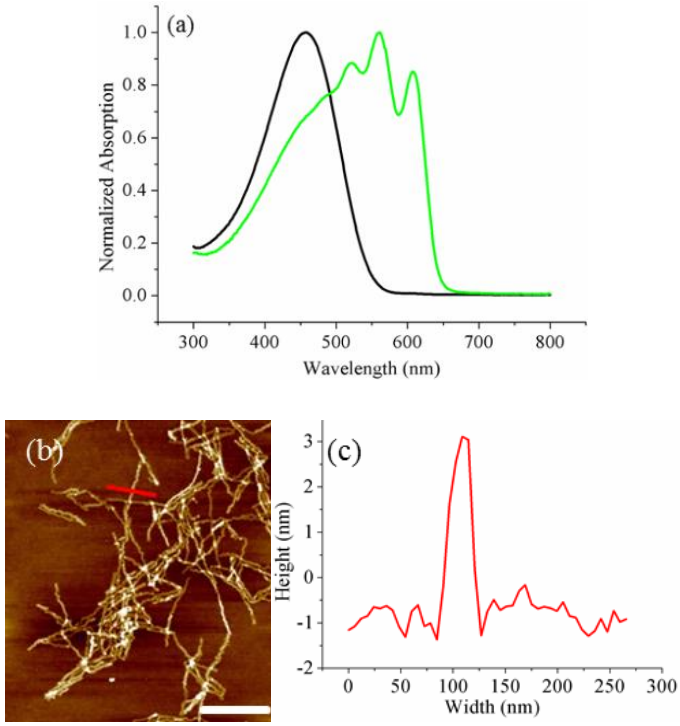

Figure 4.1. (a) Normalized UV-Vis absorption spectra of solutions 1 (black line) and 2 (green line) given in Table 4.1, after more than a week of storage in the dark under a N_2 atmosphere. (b) AFM topography image of preformed P36T nanofibers. The white scale bar in the bottom right corner denotes a length of 1 µm. (c) Nanofiber cross section along the red line in (b).

By fitting the UV-Vis absorption spectrum of this dispersion as the sum of spectra obtained from the pure fiber fraction and the well-dissolved polymer fraction, as described by Oosterbaan *et al.*,[24] the fiber-to-polymer weight fraction was estimated to be around 87%. Part of the stable fiber solution was further diluted to obtain solutions with a P36T concentration of either 0.05 or 0.005 wt%. A summary of the different solutions used can be found in Table 4.1 and for simplicity they will be referred to as solution 1, 2, 3 and 4.

AFM was used to characterize the dimensions of the preformed nanofibers after depositing via spincoating on a transistor substrate. Figure 4.1 (b) and (c) show an AFM topography image of preformed P36T nanofibers and a nanofiber cross section from which a height of 3–5 nm, a width of 23–28 nm

and a length of 3−4 µm, was inferred. These dimensions were in line with the ones measured by Samitsu *et al.*[26] and Oosterbaan *et al.*[24]

Solution	Solvent	Concentration	Preformed Fibers
1	chlorobenzene	0.90 wt%	No
2	*p*-xylene	0.25 wt%	Yes
3	*p*-xylene	0.05 wt%	Yes
4	*p*-xylene	0.005 wt%	Yes

Table 4.1. Summary of P36T solutions.

4.3 Organic transistor layers characterized with atomic force microscopy

After spincoating of the different solutions to fabricate OPTs, the active layer thickness, surface morphology and surface coverage were characterized with AFM. Figure 4.2 (b) and (c) illustrate that the films spun from the *p*-xylene solutions 2 and 3 consist of closely packed P36T nanofibers, forming an interconnected fiber network with *SC* 100% and 95%, respectively, and average film thicknesses of 70.3 nm and 20.2 nm, respectively. However, by ten times diluting solution 3 to obtain solution 4, the *SC* decreases tremendously to 17.4% and the film manifests itself as a web of nanofibers (Figure 4.2 (d)), rather than a close packing of nanofibers (Figure 4.2 (b)). Consequently, also the film thickness reduces to 4.2 nm, equal to the thickness of a single nanofiber. In contrast with the films from the *p*-xylene solutions, the film spun from the CB solution does not consist of an interconnected nanofiber network and reveals only some large nanofibers lying on top of it (Figure 4.2 (a)). Furthermore, the average thickness of this film was 56.0 nm. A summary of the film thickness and respective *SC* achieve for each solution is given in Table 4.2.

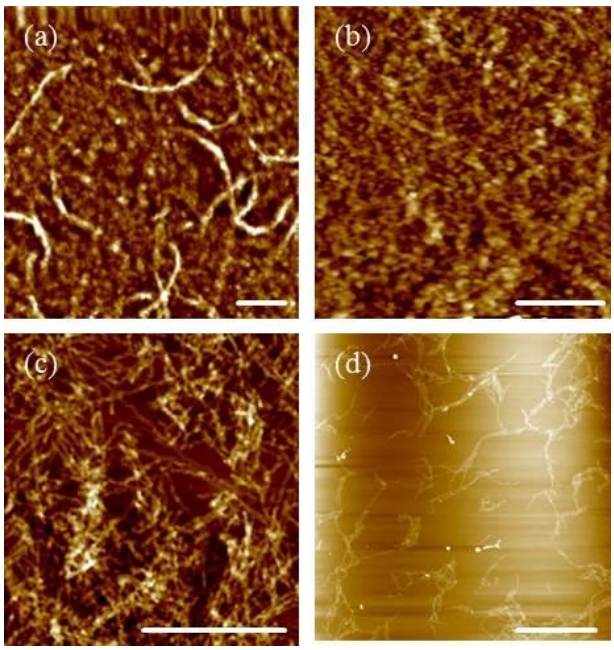

Figure 4.2. AFM topography after spincoating solution 1 (a), solution 2 (b), solution 3 (c) and solution 4 (d) on a FET substrate. The white scale bar in the bottom right corner of (a) – (d) is 2 µm long.

Solution	Layer	*d* (nm)	*R*q (nm)	*SC* *(%)*	d_{fiber} (nm)	L_{fiber} (µm))
1	P36T	56.0	5.5	100	/	/
2	P36T – fibers	70.3	18.0	100	3–5	3–4
3	P36T – fibers	20.2	4.9	95	3–5	3–4
4	P36T – fibers	4.2	2.5	17	3–5	3–4

Table 4.2. Summary of film thickness (*d*), rms roughness (*R*q), surface coverage (*SC*), fiber thickness (d_{fiber}) and fiber length (L_{fiber}), obtained after spincoating each of the solutions on a transistor substrate. The *d*, *R*q and *SC* values were obtained from 25 µm x 25 µm images. Data were averaged over ten different measurements for each solution.

4.4 Field-effect transistor analysis

Before conducting phototransistor measurements, a field-effect analysis was performed in the dark on OPTs made from each of the four different solutions. Figure 4.3 contains the transfer characteristics of a transistor made from each

of the four solutions. The results of the parameters extracted from the transfer characteristics like the ones given in Figure 4.3 are summarized in Table 4.3.

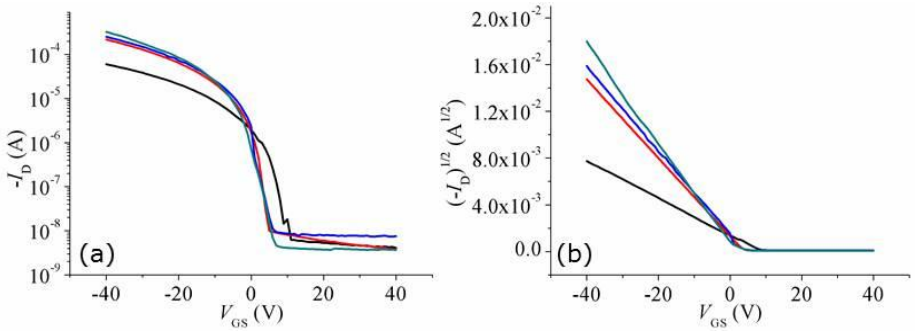

Figure 4.3. Transfers characteristics of transistors made from solution 1 (black line), solution 2 (red line), solution 3 (blue line) and solution 4 (green line), plot as $-I_D$ versus V_{GS} and as $(-I_D)^{1/2}$ versus V_{GS}. Transistors were operated in dark and in their saturation regim (V_{DS} = -60 V). Transistor length L = 10 μm and width W = (20 mm x SC), with SC the surface coverage to account for the incomplete surface coverage observed with solutions 3 and 4.

Solution	$\mu_{FET,Sat}$ (10^{-3} $cm^2V^{-1}s^{-1}$)	V_T (V)	$V_T - V_{on}$ (V)	I_{on}/I_{off}
1	1.5 ± 0.2	8.4 ± 5	4.6 ± 3	10^4
2	6.1 ± 0.7	3.4 ± 3.5	4.3 ± 3	10^4
3	7.9 ± 1	3.7 ± 2	4.5 ± 1.5	10^5
4	53 ± 8	1.0 ± 1	2.3 ± 1	10^5

Table 4.3. Summary of the FET parameters of each solution, measured in dark and in saturation (V_{DS} = -60 V). Transistor length L = 10 μm and width W = (20 mm x SC), with SC the surface coverage to account for the incomplete surface coverage observed with solutions 3 and 4. Data were averaged over at least five different transistors for each solution.

An increase in FET performance, due to an increase in $\mu_{FET,Sat}$ and a decrease in V_T, is observed when switching from solution 1 to solution 2. This improvement is achieved by introducing preformed nanofibers because within these fibers the thiophene rings along the P36T backbone adopt a more favourable, *i.e.* edge-on, orientation for charge carrier mobility.[31] In addition,

the preformed fibers increase the layer connectivity by acting as charge carrier transport highways and they also increase the crystallinity of the active FET layer. The latter can be deduced from the UV-Vis absorption spectra of films prepared from solutions 1 and 2 (Figure 4.4).

Both spectra consist of a single absorption band with a vibrational structure centered around 550 nm. For the film prepared from solution 2, however, the vibrational structure is much more pronounced. In addition, the vibrational transition at low energy (610 nm) is slightly red-shifted and has gained relative intensity at the cost of the transition at high energy (525 nm). This results in a red-shift of the absorption band maximum from 525 nm for the film from solution 1 to 550 nm for the film from solution 2. The red-shifted absorption together with the more pronounced vibrational structure is indicative of higher microstructural order, an observation supported by the work performed by Oosterbaan *et al.*[32] From the intensity ratio of the first and second vibronic transition (A_{0-0}/A_{0-1}) in the film absorption spectra, the interchain coupling energy W_{ic} for each film can be calculated. Taking the Huang-Rhys factor S to be 1 for P36T and setting the P36T thin film refractive index ratio $n_{0\text{-}1}/n_{0\text{-}0}$ equal to 1, A_{0-0}/A_{0-1} is related to W_{ic} as:[33,34]

$$\frac{A_{0\text{-}0}}{A_{0\text{-}1}} \approx \left(\frac{1 - 0.24 \, W_{ic} / E_p}{1 + 0.073 \, W_{ic} / E_p} \right)^2 \qquad (4.1)$$

For P36T the phonon energy of the main intramolecular vibration coupled to the electronic transfer Ep can be set to 0.18 eV 34, such that values for Wic are calculated to be 106 meV and 44 meV for the films from solutions 1 and 2, respectively.

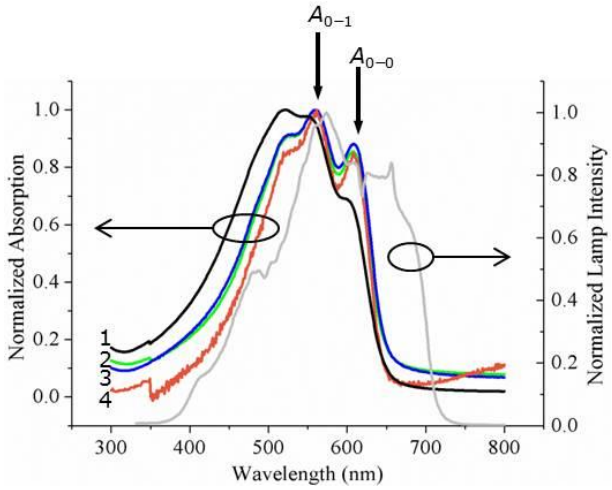

Figure 4.4. Normalized UV-Vis absorption spectra of films prepared from solution 1 (black line), solution 2 (green line), solution 3 (blue line) and solution 4 (orange line) after storing the solutions for more than a week. Additionally also the normalized lamp emission spectrum (grey line) is given. A_{0-0} and A_{0-0} indicate the position of the first and second vibronic transition, respectively

The lower value of W_{ic} found for the film spun from the nanofiber containing solution can now be related to an increase in polymer conjugation length within the film and therefore to an increase in microcrystalline order.[35] However, among the nanofiber containing solutions 2, 3 and 4, a further improvement in FET performance is observed upon decreasing the concentration and hence the *SC* of the spin-coated active FET layer, when going from solution 2 to solution 4. Since W_{ic} is slightly decreased from 44 meV to 36 meV and 35 meV for films prepared from solution 2, 3 and 4, respectively, this was related to a persisting small increase in overall film crystallinity, as was also proposed by Bolsée *et al.*[36] From a decrease in surface coverage when going from solution 2 to 4, they inferred a reduction in the parallel close packing of the fibers and with it a decrease in amorphous interfiber grain boundaries, formed from well-dissolved P3HT, coexisting in solution with the preformed nanofibers. Therefore, these boundaries inherently possess lower charge carrier mobility and higher deep charge carrier trap density, limiting the overall charge carrier mobility, shifting V_T to more positive

values and increasing $V_T - V_{on}$ by increasing the deep electron trap density of the active FET layer. Once and for all, if high FET performance is desired, the *SC* should be kept to a minimum, since then the number of interfiber boundaries is minimized. The ideal case would be the one for which several well-separated fibers bridge the gap between source and drain.

4.5 Phototransistor analysis

This section starts with the influence of an incident white light beam on the transfer characteristics and the electronic structure of the active layer of OPTs made from each of the four different solutions studied in this work. Figure 4.5 (a) reveals a clear positive shift in V_T and increase in $I_{D,off}$ with increasing I_{inc}. However, correcting for the former by plotting $(-I_D)^{1/2}$ versus $V_{GS} - V_T$ instead of V_{GS} as in Figure 4.5 (b), shows that the slope of the transfer curves is not altered, meaning that, according to (3.3), $\mu_{FET,Sat}$ is the same for every I_{inc}. Consequently, it can safely be assumed that also the electronic structure of the active layer is not altered under the incoming white light.[37,38] Next, Figure 4.5 (c) and (d) gather two plots of the generated photocurrent $I_{D,photo}$ as function of I_{inc}.

The plot in Figure 4.5 (c) is obtained from a fiber-based OPT working in the on-state ($|V_{GS}| > |V_T|$), showing a logarithmic behaviour which can be fit by (3.5). As this equation was developed for inorganic transistors for which the PV effect was dominating the on-state operation, it was concluded from the observed match between the experimental data and (3.5) that this was also the case for the fiber-based OPT studied here. Within this study, this refers to trapping of electrons near the source contact, which enhances the injection of holes in the channel and therefore increases the current flowing in the transistor channel. Furthermore, the first equality in (3.5) also links the trapping of electrons to the shift in V_T observed in Figure 4.5 (a). The plot in Figure 4.5 (d) gives the photocurrent of a fiber-based OPT in the off-state ($|V_{GS}| < |V_T|$) as function of I_{inc} together with a fit according to (3.6). The good match between the fit and measured data leads to the conclusion that

the PC effect dominates the photocurrent generation when a fiber-based OPT operates in its off-state.

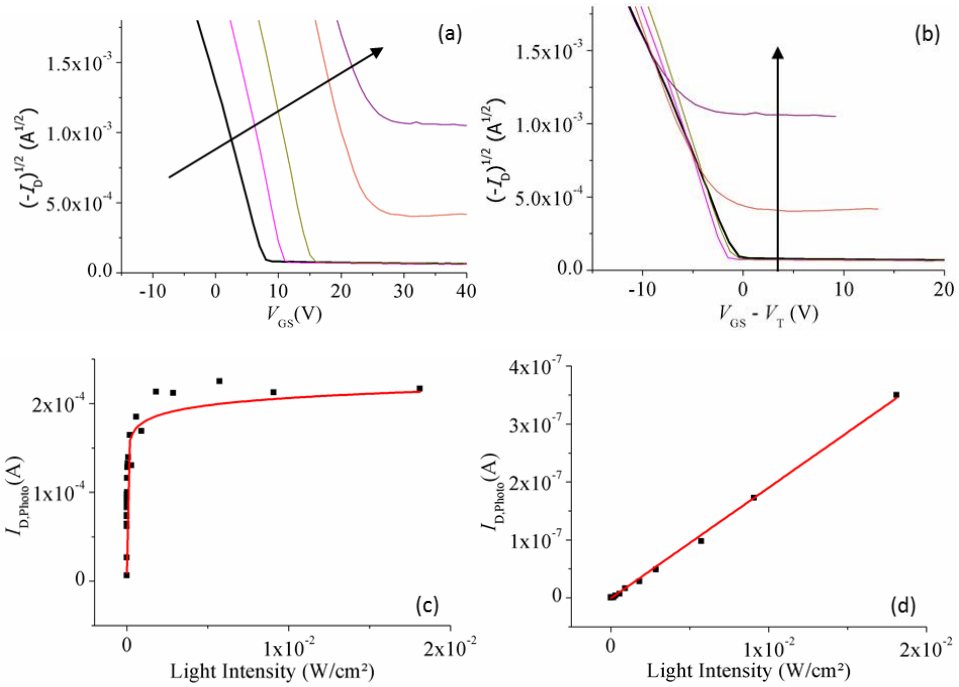

Figure 4.5. Characteristics of a fiber-based OPT fabricated using solution 3, reaching a surface coverage of 95%. Transfer curves obtained at different I_{inc} plotted as $(-I_D)^{1/2}$ versus V_{GS} (a) and $V_{GS} - V_T$ (b) for V_{DS} = -60 V. The arrow indicates the direction of increasing light intensity. The black curve in (a) and (b) was measured in dark, while the others were measured with I_{inc} = 0.018 mW cm^{-2}, 0.18 mW cm^{-2}, 1.8 mW cm^{-2} and 18 mW cm^{-2}, respectively. Photocurrent as function of the incident white light intensity for a fiber-based OPT working in the on-state (V_{GS} = -40 V) together with its fit according to (3.5) (c) and in the off-state (V_{GS} = 40 V) together with its fit according to (3.6) (d) for V_{DS} = -60 V. The square symbols in (c) and (d) represent the measured data for a fiber-based OPT and the red lines represent the fits by (3.5) and (3.6).

To estimate whether the devices studied in this work show promising OPT performance, P and R together with $\mu_{FET,Sat}$ for the different solutions are collected in Table 4.4. The OPT performance improvement of solutions 2 and 3 relative to solution 1 cannot solely be attributed to the increased $\mu_{FET,Sat}$ as observed in Table 4.3. One should also consider the better spectral overlap, as

observed in Figure 4.4, between the film absorption spectrum and the lamp emission spectrum when preformed nanofibers are introduced in the spincoating solution, as this leads to the formation of a red-shifted H-aggregate absorption band. Furthermore, the absorption is maximized because the polymer chains, having their π-π* transition dipole moment along their backbone, orient themselves along the FET substrate.[32] The improvements in charge carrier transport and light absorption combine into an improved η. According to (3.5) and (3.6), these improvements lead to an increase in $I_{D,photo,pv}$ and $I_{D,photo,pc}$. Thus, in general a higher $I_{D,photo}$ and therefore, according to (3.7) and (3.8), a higher R and P are obtained. From Table 4.2 and Table 4.3 the devices made from solutions 2 and 3 differ predominantly in active layer thickness. As such, it is inferred that this difference in layer thickness is responsible for the observed difference in OPT performance. Further reasoning proofs this must be the case, as from Table 4.4 one can deduce that while R is only doubled, P experiences a fivefold increase from solution 2 to solution 3. Therefore, the difference between the two solutions is dominated by a difference in P, which is measured in the off-state, *i.e.* when the photoconductive effect dominates $I_{D,photo}$. As the layer becomes thicker, many charges will be generated further away from the contacts and since the nanofibers, lying mainly parallel to the substrate surface, possess a low transversal mobility, their ability to efficiently transport these charges to the drain contact is rather low.[39] Hence, charges generated too far away from the contacts cannot contribute to $I_{D,photo}$. This explains why the thinner layer from solution 3 performs better than the thicker layer from solution 2.

Finally, a large decrease in OPT performance is observed when going from solution 3 to solution 4. Although the latter gave the best results concerning FET performance, the large *SC* reduction results in a large reduction in active layer material being present and therefore also in light absorbing capacity. Consequently, the generated $I_{D,photo}$ is less, such that R and P are reduced according to (3.7) and (3.8). Yet another argument comes from the reduction in deep trap density with lowering the *SC*, as found by Bolsée *et al.*[36] This will especially influence $I_{D,photo,pv}$, for which trapping of electrons near the source is

responsible for the observed gain mechanism. As such, $I_{D,photo,pv}$ and also $I_{D,photo}$ will decrease with decreasing *SC* and consequently *P* and *R* will become smaller.

Solution	$\mu_{FET,Sat}$ (10^{-3} $cm^2V^{-1}s^{-1}$)	*R* (A W^{-1})	*P* (10^3)
1	1.5 ± 0.2	50 ± 10	1.4 ± 0.2
2	6.1 ± 0.7	110 ± 18	1.3 ± 0.1
3	7.9 ± 1	250 ± 20	6.8 ± 0.8
4	53 ± 8	34 ± 6	11 ± 2

Table 4.4. Comparison of OPT performance for devices fabricated from four different solutions. The saturation charge carrier mobility $\mu_{FET,Sat}$ was extracted from transfer characteristics measured in dark with V_{DS} = -60 V, while photosensitivity *P* and photoresponsivity *R* were extracted under light conditions with V_{DS} = -60 V and I_{inc} = 0.91 mW cm^{-2}. *R* was measured in the on-state (V_{GS} = -40 V) and *P* in the off-state (V_{GS} = 10 V). Transistor length *L* = 10 µm and width *W* = (20 mm x *SC*), with *SC* the surface coverage to account for the incomplete surface coverage observed with solutions 3 and 4. Data were averaged over at least three different transistors for each solution.

The best performing OPT devices in this study were fabricated from solution 3, having a maximum *R* of about 250 A W^{-1} in the on-state (V_{GS} = -40 V) and a maximum *P* of 6.8 x 10^3 in the off-state (V_{GS} = 10 V) for I_{inc} = 0.91 mW cm^{-2} and V_{DS} = -60 V (Figure 4.6 (a)). The maximum value of *R* is reached when an OPT is turned fully on (V_{GS} = -40 V), because then the current handling capacity of the OPT is maximized. On the other hand, the value of *P* reaches a maximum at V_{GS} = 10 V, when the OPT is turned off. This is because, at V_{GS} = 10 V $I_{D,light}$ is almost maximum while $I_{D,dark}$ is still around its minimum, in which case the ratio of $I_{D,light}$ to $I_{D,dark}$ is maximized, as can be seen in Figure 4.6 (b), and according to equation 3.8, *P* is therefore also maximized. The values for *P* and *R* reported here are slightly better than the ones reported by Pal *et al.*, who reported maximum *R* and *P* of 245 A W^{-1} and 3.8 x 10^3, respectively.[23]. However, since their starting solution did not possess any preformed structures, their results could only be obtained with the help of a SAM of OTS, inducing favourable edge-on orientation of the thiophene rings along the P36T

backbone, and a post-deposition thermal annealing step of 15 min at 130 °C to enhance the orientation of polymer molecules and film crystallinity. As already highlighted by Oosterbaan *et al.*, solutions containing preformed fibers do not require any SAM or post-deposition annealing to reach the preferential polymer orientation and high layer crystallinity.[32,40] Even better, the SAM influence on device operation was neglibible and therefore these nanofiber containing solutions do not put a high demand on the type of substrate used, broadening the range of different device substrates that can be used. Additionally, Pal *et al.*[23] used transistors with a channel length of only 3 µm for which short channel effects have been observed for V_{DS} > -60 V, which may impede a correct OPT analysis as pointed out by Chabinyc *et al.*[41]

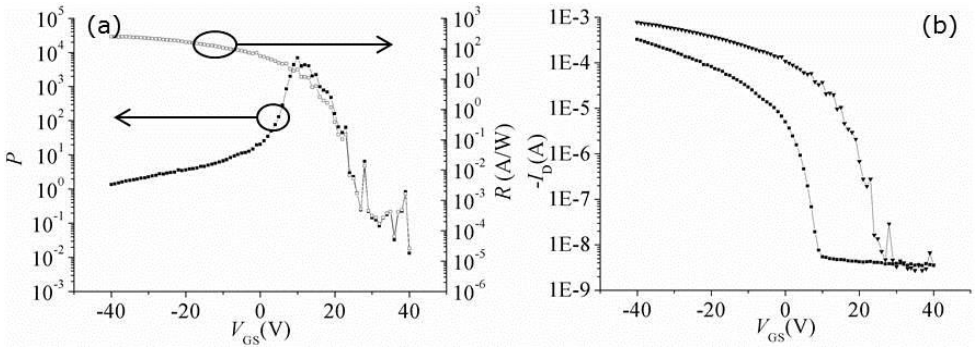

Figure 4.6. (a) Measured *P* (filled squares) and *R* (open squares) and (b) $-I_{D,dark}$ (squares) and $-I_{D,dark}$ (triangles) for an OPT fabricated from solution 3 with V_{DS} = -60 V and I_{inc} = 0.91 mW cm^{-2}.

Figure 4.7 illustrates an interesting property of the devices fabricated from solution 3. For a specific I_{inc}, R can be tuned over as much as five orders of magnitude by varying V_{GS}. For I_{inc} as low as 18 nW cm^{-2}, R varies from 4.8 A/W for V_{GS} = 40 V to 1.2 x 10^6 A/W for V_{GS} = -40 V. Since the incident light intensity is the same, the number of photogenerated excitons and the primary photocurrent remain the same. So what changes upon varying V_{GS} is the magnitude of the gain mechanism.[18] For V_{GS} = 40 V the OPT gain mechanism is dominated by the photoconductive effect, while for V_{GS} = -40 V the photovoltaic effect dominates. This is an interesting property, since this allows one to tune the photocurrent gain according to I_{inc}. Additionally, Figure 4.7

reveals a decreasing R for an increasing I_{inc}, which can be explained using equation 3.7. Following the relation, the increase in I_{inc} dominates the observed trend in Figure 4.7 and therefore photocurrent production is more efficient at lower I_{inc}.

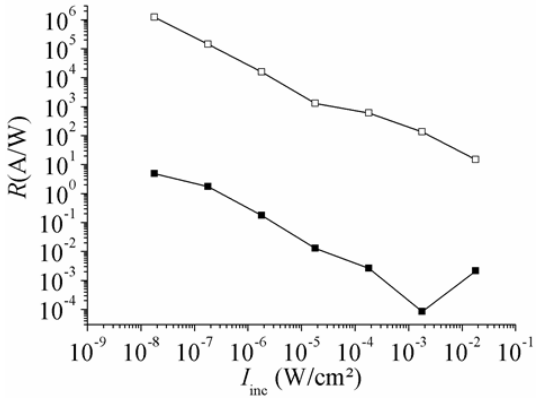

Figure 4.7. Responsivity *R* as function of incident white light intensity measured at different gate voltages, V_{GS} = 40 V (filled squares) and V_{GS} = -40 V (open squares).

4.6 Technical details

UV-Vis spectra. An Agilent Cary 500 UV-Vis-NIR spectrophotometer was used to measure the absorption spectra of solutions and films. Quartz cuvettes were used to measure solutions while films were fabricated via spincoating on quartz substrates using the same parameters as the ones used to prepare the OPTs.

Dimensional and morphological characterization. The dimensions of individual nanofibers were characterized using a Brüker Multimode 8 Atomic Force Microscope (AFM) with a Nanoscope V controller operated in peak force tapping mode. To take into account tip broadening effects due to the non-ideal AFM tip shape, the width of a nanofiber was estimated from the full width at half maximum of a nanofiber cross section. The same setup was later on used to determine layer thickness and surface morphology of each device. The transistor surface coverage was determined from analyzing the topography images using image analysis software.

Device substrates. Transistor substrates were obtained from Philips Innovation Services, and were built up of a 200 nm thick SiO_2 dielectric thermally grown on a highly n-doped Si wafer with metal contacts patterned on top of it. The patterning was done in such a way that device length *L* and width *W* were 10 µm and 20 mm, respectively. The dielectric capacitance per unit area was C_0 = 16.9 nF cm^{-2} and the metal contacts consisted of 100 nm gold on top of a 10 nm titanium adhesion layer. Finally the top surface of the substrates was coated with a self-assembled monolayer of HMDS to passivate the bare SiO_2 dielectric.

Transistor fabrication. Prior to film deposition the substrates were cleaned according to a standard procedure of 15 minutes ultrasonication in soap solution, rinsing with water, 15 minutes ultrasonication in acetone, rinsing with acetone, 15 minutes boiling in isopropanol and finally dry blowing with N_2. After cleaning, the substrates were transferred into a N_2 pressurized glovebox and preannealed for 15 minutes at 120 °C to remove residual oxygen and water from the hydrophilic SiO_2 dielectric. In a last step the different solutions were spin coated on top of the FET substrates, yielding devices as schematically illustrated in Figure 3.1. Spin coating parameters, speed, acceleration and time were 750 rpm, 500 rpm/s and 60 s and 1000 rpm, 3000 rpm/s and 60 s, for the fiber containing solutions 2, 3 and 4 and solution 1 with well-dissolved P36T, respectively.

FET measurements. To measure output (I_D – V_{DS}) and transfer (I_D – V_{GS}) characteristics of the fabricated OPTs, a wafer prober with three different mobile probes, one for each transistor contact, was used. With the source grounded, a Keithley 2400 SourceMeter connected to the drain probe allowed to apply a drain-source voltage V_{DS} and measure the drain-source current I_{DS} with the same device. Yet another Keithley 2400 SourceMeter was connected to the gate probe to control the gate-source voltage V_{GS} and continuously monitor the leakage current, I_{leak}, flowing through the gate dielectric, for which I_{DS} had to be corrected to give the average current flowing through the transistor channel I_D according to:[36]

$$I_D = I_{DS} + \frac{I_{leak}}{2} \quad (4.2)$$

The devices were first characterized for their transistor performance in the dark. Output characteristics (I_D–V_{DS}) for different V_{GS} were measured first to determine the linear and saturation regime of the OPT, afterwards the transfer characteristics (I_D–V_{GS}) were measured in saturation (V_{DS} = -60 V), for which the current flowing through the OPT channel is maximum without causing any damage to the active organic layer. From these transfer characteristics transistor parameters, $\mu_{FET,sat}$ and V_T, were extracted by fitting the linear part of the saturation transfer characteristics, plot as $(-I_D)^{1/2}$ versus V_{GS}, while the onset voltage V_{on}, defined as V_{GS} where I_D starts to increase, and the ratio of the on-state current to the off-state current I_{on}/I_{off} were determined from a plot of $-I_D$ versus V_{GS}. These parameters were averaged for each solution over at least five different devices having a channel length L = 10 μm and a width W = 20 mm multiplied by the surface coverage SC in order to account for incomplete surface coverage, observed with solutions 3 and 4.

Phototransistor measurements. Broadband white light from a 150 W halogen lamp was used to irradiate the OPT samples from the top. A silicon photodiode was used to set the intensity of the light reaching the OPT surface at 18 mW cm^{-2}. With the help of neutral density filters the incident white light intensity I_{inc} could be varied between 18 mW cm^{-2} and 18 nW cm^{-2}. Transfer characteristics were always measured from on-state (V_{GS} = -40 V) to off-state (V_{GS} = 0 V or V_{GS} = 40 V) with the device operating in saturation (V_{DS} = -60 V) and all reported data were averaged over at least three different devices. The devices studied did not suffer short channel effect as observed previously by Chabinyc *et al.*[41]

4.7 References

1 N. M. Johnson and A. Chiang, *Appl. Phys. Lett.*, 1984, **45**, 1102.

2 Y. Kaneko, N. Koike, K. Tsutsui and T. Tsukada, *Appl. Phys. Lett.*, 1990, **56**, 650.

3 C. S. Choi, H. S. Kang, W. Y. Choi, H. J. Kim, W. J. Choi, D. J. Kim, K. C. Jang and K. S. Seo, *IEEE Photon. Technol. Lett.*, 2003, **15**, 846.

4 H. S. Kang, C. S. Choi, W. Y. Choi, D. H. Kim and K. S. Seo, *Appl. Phys. Lett.*, 2004, **84**, 3780.

5 T. P. I. Saragi, R. Pudzich, T. Fuhrmann and J. Salbeck, *J. Appl. Phys. Lett.*, 2004, **84**, 2334.

6 Y. Y. Noh, D. Y. Kim, Y. Yoshida, K. Yase, B. J. Jung , E. Lim and H. K. Shim, *Appl. Phys. Lett.*, 2005, **86**, 043501.

7 Y. Guo, C. Du, C. Di, J. Zheng, X. Sun, Y. Weng, L. Zhang, W. Wu, G. Yu and Y. Liu, *Appl. Phys. Lett.*, 2009, **94**, 143303.

8 Q. Tang, L. Li, Y. Song, Y. Liu, H. Li, W. Xu, Y. Liu, W. Hu and D. Zhu, *Adv. Mater.*, 2007, **19**, 2624.

9 T. P. I. Saragi, J. Londenberg and J. Salbeck, *J. Appl. Phys.*, 2007, **102**, 046104.

10 S. R. Forrest, *Nature*, 2004, **428**, 911.

11 A. J. Heeger, *Angew. Chem. Int. Ed.*, 2001, **40**, 2591.

12 A. Facchetti, M. H. Yoon and T. J. Marks, *Adv. Mater.*, 2005, **17**, 1705.

13 B. Crone, A. Dodabalapur, Y. Y. Lin, R. W. Filas, Z. Bao, A. LaDuca, R. Sarpeshkar, H. E. Katz and W. Li, *Nature*, 2000, **403**, 521.

14 Z. Bao, *Semiconductive Polymers*, 1999, Ed B. Hseih, Y. Wei and M. E. Galvin (Washington, DC: American Chemical Society).

15 R. M. Meixner, H. Göbel, F. A. Yildirim, W. Bauhofer and W. Krautschneider, *Appl. Phys. Lett.*, 2006, **89**, 092110.

16 N. Marjanovic, Th. B. Singh, G. Dennler, S. Gunes, H. Neugebauer, N. S. Sariciftci, R. Schwödiauer and S. Bauer, *Org. Electron.*, 2006, **7**, 188.

17 K. S. Narayan and N. Kumar, *Appl. Phys. Lett.*, 2001, **79**, 1891.

18 M. C. Hamilton, S. Martin and J. Kanicki, *IEEE Trans. Electron Devices*, 2004, **51**, 877.

19 M. C. Hamilton and J. Kanicki, *IEEE J. Sel. Top. Quantum Electron.*, 2004, **10,** 840.

20 Y. Xu, P. R. Berger, J. N. Wilson and U. H. F. Bunz, *Appl. Phys. Lett.*, 2004, **85,** 4219.

21 M. Deen and M. H. Kazemeini, *Proc. IEEE.*, 2005, **93,** 7.

22 H. Dong, H. Li, E. Wang, H. Nakashima, K. Torimitsu and W. Hu, *J. Phys. Chem. C*, 2008, **112,** 19690.

23 T. Pal, M. Arif and S. I. Khondaker, *Nanotechnology*, 2010, **21**, 325201.

24 W. D. Oosterbaan, V. Vrindts, S. Berson, S. Guillerez, O. Douhéret, B. Ruttens, J. D'Haen, P. Adriaensens, J. Manca, L. Lutsen and D. Vanderzande, *J. Mater. Chem.*, 2009, **19**, 5424.

25 S. Berson, R. De Bettignies, S. Bailly and S. Guillerez, *Adv. Funct. Mater.*, 2007, **17**, 1377.

26 S. Samitsu, T. Shimomura, S. Heike, T. Hashizume and K. Ito, *Macromolecules*, 2008, **41**, 8000.

27 K. Zhao, L. Xue, J. Liu, X. Gao, S. Wu, Y. Han and Y. Geng, *Langmuir*, 2010, **26**, 471.

28 S. Sun, T. Salim, L. H. Wong, Y. L. Foo, F. Boey and Y. M. Lam, *J. Mater. Chem.*, 2011, **21**, 377.

29 Y. D. Park, S. G. Lee, H. S. Lee, D. Kwak, D. H. Lee and K. Cho, *J. Mater. Chem.*, 2011, **21**, 2338.

30 J. D. Roehling, I. Arslan and A. J. Moulé, *J. Mater. Chem.*, 2012, **22**, 2498.

31 C. D. Dimitrakopoulos, P. R. L. Malenfant, *Adv. Mater.*, 2002, **14**, 99.

32 W. D. Oosterbaan, J. C. Bolsée, A. Gadisa, V. Vrindts, S. Bertho, J. D'Haen, T. J. Cleij, L. Lutsen, C. R. McNeill, L. Thomsen, J. V. Manca and D. Vanderzande, *Adv. Funct. Mater.*, 2010, **20**, 792.

33 F. C. Spano, *J. Chem. Phys.*, 2005, **122**, 234701.

34 J. Clark, C. Silva, R. H. Friend and F. C. Spano, *Phys. Rev. Lett.*, 2007, **98**, 206406.

35 J. Clark, J. F. Chang, F. C. Spano, R. H. Friend and C. Silva, *Appl. Phys. Lett.*, 2009, **94**, 163306.

36 J. C. Bolsée, *PhD Thesis: Macroscopic and nanoscale charge transport in poly(3-alkylthiophene)s: from single nanofiber to semicrystalline thin films*, 2012, (Hasselt: University of Hasselt).

37 G. Horowitz, R. Hajlaoui, R. Bourguiga and M. Hajlaoui, *Synth. Met.*, 1999, **101,** 401.

38 A. R. Brown, C. P. Jarrett, D. M. deLeeuw and M. Matters, *Synth. Met.*, 1997, **88**,37.

39 J. C. Bolsée, W. D. Oosterbaan, L. Lutsen, D. Vanderzande and J. Manca, *Org. Electron.*, 2011, **12**, 2084.

40 W. D. Oosterbaan, J. C. Bolsée, L. Wang, V. Vrindts, L. J. Lutsen, V. Lemaur, D. Beljonne, C. R. McNeill, L. Thomsen, J. V. Manca and D. J. M. Vanderzande, *Adv. Funct. Mater.*, 2014, **24**, 1994.

41 M. L. Chabinyc, J. P. Lu, R. A. Street, Y. Wu, P. Liu and B. S. Ong, *J. Appl. Phys.*, 2004, **96**, 2063.

Chapter 5

Conclusions and outlook

This final chapter gathers the conclusions from the previous chapters and presents an outlook for future research.

5.1 Conclusions

The goal of this work was to boost OPT performance by incorporating preformed P36T nanofibers in the active OPT layer, eliminating the need of any post-production (thermal or solvent) or substrate surface treatment. A detailed review of the state-of-the-art nanofiber production methods available to date was given in chapter 2. All solution self-assembly approaches mentioned in this chapter take advantage of the strong π-π stacking interactions between the polymer chains to grow P3*A*T nanofibers with high hole mobility, originating from the π-π stacking direction and hence the hole delocalization along the nanofiber longitudinal axis. Furthermore, fiber formation in solution, prior to deposition, enables the polymer chains to obtain their lowest energy conformation, such that the nanofibers end up with a fully relaxed and therefore intrinsically stable internal structure. Although the production process is influenced by many different parameters, some very reliable fiber fabrication methods are available to date, which were given in section 2.1.1.

Having cross sections in the nanometer range and lengths of a few micrometers, different previous studies mentioned in chapter 2 show that P3*A*T nanofibers are well suited to be applied as preformed building blocks in organic electronics. Moreover, no post-deposition thermal annealing is necessary to reach high device performances, opening up the possibility for the use of PET substrates, as required for flexible organic electronics. The preformed nanofibers also render the layer morphology independent of the deposition technique, increasing reproducibility of the best device performance and inducing more consistency in device fabrication. Even more important, it increases the freedom to choose the most suitable deposition method for industrial applications.

Specifically related to FETs, since the nanofiber layers appear to be much less sensitive to the dielectric surface, some fundamental insights were obtained in the past. Single nanofiber FETs revealed large mobility anisotropy and provided an estimation of the maximum current density a single nanofiber can withstand. These results are surely interesting and important for device engineers. Due to the large mobility anisotropy, a film of nanofibers oriented parallel to the substrate could possess a high drain-to-source current with a limited undesired bulk current. This mobility anisotropy was also crucial in this study as it was seen to determine the difference in OPT operation between P36T nanofiber solution 2 and 3 in chapter 4. Further fundamental results were obtained by other research groups. Studying monolayers of nanofibers enabled the direct examination of the interfacial interaction between a dielectric and a nanofiber film. The extracted results could provide engineers with valuable information towards dielectric surface engineering for high performance organic FETs.

Because of their increased absorption relative to films deposited from well-dissolved P3*A*T solutions in combination with their insensitivity to dielectric surface treatment, P3*A*T nanofiber films are not only promising for implementation in OPV, but also in organic photodetectors and phototransistors, providing great motivation for this PhD thesis. As such, it is shown in chapter 4 that high performance OPTs with photoresponsivity *R* and photosensitivity *P* reaching 250 A W^{-1} and 6.8 x 10^3 under low level of white light illumination, respectively, can be obtained using preformed P36T nanofibers and carefully controlling the surface coverage. As such, our nanofiber-based OPTs outperform the ones fabricated from a solution of well-dissolved P36T in CB, not containing any preformed fibers. The better performance is partly attributed to a longer exciton diffusion length and higher charge carrier mobility due to a decreased interchain coupling resulting from the lamellar packing of the polymer chains within the nanofibers and a higher level of layer connectivity resulting from the extended nature of crystalline grains in the polymer nanofibers. Furthermore, because of a red-shifted H-

aggregate absorption band related to the preformed nanofibers in the active layer, a better spectral overlap between the white light emission spectrum and the active layer absorption spectrum was obtained. In combination with the maximized light absorption resulting from parallel orientation of the polymer chain transition dipole moment with respect to the FET substrate, the better spectral overlap results in an increased overall amount of light absorption. Additionally, inherent to an intrinsic gate tuneable gain mechanism, changing the gate potential allows one to tune the responsivity *R* over at least five orders of magnitude and adjust it according to the incident light intensity. Since no special dielectric surface treatment or post-deposition treatment of the active device layer was performed, similar high OPT performance is ought to be possible on a wide variety of different substrates, including flexible and light-weight PET substrates.

5.2 Outlook

As referred to in chapter 2, previous studies have shown that nanofibers incorporated in the active layer of BHJ OPVs can increase the thermal stability of the devices by providing a stable network that prevents PCBM from forming micrometer-sized clusters when exposed to high temperatures. This still requires further confirmation though, since it was not consistently observed. Another inconsistency concerns the addition of PCBM to the active blend before or after nanofiber growth, as this might influence the P36T chain mobility in solution.

So far, nanofibers of monolayer thickness have only been fabricated with P36T, so it might be worthwhile to try to produce fibers of monolayer thickness for a whole range of P3*A*T to study the possible alkyl-chain length dependency of the interfacial interactions. The monolayer fibers can also assist in the quest for the optimal dielectric surface treatment minimizing interfacial traps and other processes limiting the interfacial charge carrier mobility. For further improvement of FET performance,

work should also be conducted on the alignment of the nanofibers in the direction of the channel.

Incorporation of nanofibers in the device active layer opened up new areas for device-related research, since for a better understanding of the optoelectronic properties, structural models of P3AT nanofibers (like the coarse-grained model[1]) should be coupled with more sophisticated electronic models, enabling the active layer nanomorphology to be designed more target-specific. The nanomorphological influence on device performance has already been studied for OPV, linking OPV performance to the ratio of polymer fibers versus amorphous polymer in the solution prior to layer deposition. However, no such study has been conducted for OPTs, although also here this ratio is expected to influence the charge carrier trap density, regulating the photoresponsive performance of the devices in the on-state.

With respect to direct future applications, a particular concern should also be the improvement of the environmental stability of these devices by using insulating polymer layers to shield them from the detrimental influence of oxygen and moisture.

In the past some studies on the electrospinning of P3AT nanofibers have been conducted. The benefit of ths technique was that the produced fibers could be directly captured and aligned onto a device substrate in a controlled manner, revealing a way to straightforwardly produce organic field-effect transistors. Although some promising results were already achieved with electrospun nanofiber FETs, little efforts have been done so far to relate the electrical characteristics with the specific internal nanofiber morphology. Future studies should therefore aim at correlating electrical results obtained from FETs with the internal structure of the electrospun nanofibers, in the same way as it has been done for nanofibers produced via solution self-assembly. The development of a model for the internal fiber morphology is essential for a further in-depth discussion regarding the interpretation of the optoelectronic

data. Although fabrication of nanoelectronic devices might benefit from the high level of control over the number of deposited electrospun nanofibers, the diameter of the electrospun nanofibers is still at least one order of magnitude larger as compared to the solution self-assembled nanofibers. To compete with solution self-assembled nanofibers in the field of device size reduction, additional efforts should be undertaken to reduce the fiber diameter, while avoiding the loss of uniformity along the fiber length as has been observed in the past. In addition, one should aim at electrospinning in an inert or at least dark environment to limit the uptake of moisture and oxygen. Anyhow, to avoid working in dark, one might also aim at improving the environmental stability of the organic materials. In addition, encapsulation after device fabrication to shield the organic material from moisture and oxygen might seriously improve the environmental stability. For organic phototransistors based on P3AT fibers this might actually be the only way to improve the device lifetime, since the uptake of moisture and oxygen is only significant when operating under light conditions.

5.3 References

1 K. N. Schwarz, T. W. Kee and D. M. Huang, *Nanoscale*, 2013, **5**, 2017.

Abbreviations and symbols

A	Alkyl side-chain length
AFM	Atomic Force Microscope
AO	Atomic Orbital
Au	Gold
BAS-PPE	2,5-bis(dibutylaminostyryl)-1,4-phenylene-*b*-alkyne-*b*-1,4-bis(2-ethylhexyl)benzene terpolymer
BGBC	Bottom Gate Bottom Contact
BGTC	Bottom Gate Top Contact
δ	Hildebrand solubility parameters
C-AFM	Conducting Atomic Force Microscope
C_6F_{13}	trichloro(1*H*,1*H*,2*H*,2*H*-perfluorooctyl)silane
CB	Chlorobenzene
CF	Chloroform
DCM	Dichloromethane
ξ	Crystallite size
E_a	Activation energy
E_{CT}	Intermolecular charge transfer energy
EQE	External Quantum Efficiency
f	Mass fraction
FAS	Perfluorodecyltrimethoxysilane

FET	Field Effect Transistor
FF	Fill Factor
FT-IR	Fourier Transform Infrared Spectroscopy
FTPS	Fourier Transform Photocurrent Spectroscopy
FWHM	Full Width at Half Maximum
Ge	Germanium
GIXRD	Grazing Incidence X-Ray Diffraction
GPC	Gel Permeation Chromatography
HR-TEM	High-Resolution Transmission Electron Microscopy
HMDS	Hexamethyldisilazane
HOMO	Highest Occupied Molecular Orbital
IC	Integrated Circuit
I_{on}/I_{off}	Ratio of on-state current versus off-state current
$I_{D,photo}$	Photocurrent flowing in the transistor channel
$I_{D,photo,pc}$	Photocurrent predominantly generated by the photoconductive effect
$I_{D,photo,pv}$	Photocurrent predominantly generated by the photovoltaic effect
Ir	Irridium
J_{SC}	Short-Circuit Current
λ	Wavelength of irradiation

LUMO	Lowest Unoccupied Molecular Orbital
MDMO-PPV	Poly[2-methoxy-5-(3',7'-dimethyloctyloxy)]-1,4-phenylene vinylene
MeCN	Acetonitrile
MO	Molecular Orbital
MOSFET	Metal Oxide Semiconductor Field Effect Transistor
NEXAFS	Near Edge X-Ray Absorption Fine Structure Spectroscopy
ODCB	Ortho-dichlorobenzene
OFET	Organic Field Effect Transistor
OPT	Organic Phototransistor
OPV	Organic Photovoltaics
OTS	Octyltrichlorosilane
P	Photosensitivity
P3*A*T	Poly(3-alkylthiophene)
P34T	Poly(3-Butylthiophene)
P36T	Poly(3-hexylthiofeen) / Poly(3-hexylthiophene)
P38T	Poly(3-octylthiophene)
PC	Photoconductive
PCBM	[6,6]-phenyl-C_{61}-butyric acid methyl ester
PCE	Power Conversion Efficiency
PCL	Poly(ε-caprolactone)

PD	Photodiode
PEDOT:PSS	Poly(3,4-ethylenedioxythiophene):poly(styrene sulfonate)
PET	Poly(ethylene terephthalate)
PL	Photoluminescence
PMMA	Poly(methylmethacrylate)
PS	Poly(styrene)
PT	Phototransistor
Pt	Platinum
PTFE	Polytetrafluoroethylene
PV	Photovoltaic
R	Photoresponsivity
R_{bP}	Nanofiber bridging point resistance
RC delay	Resistive-Capacitive delay
R_g	Radius of gyration
rms	Root mean square
R_{nf}	Nanofiber charge carrier transport resistance
SAM	Self assembled monolayer
SAED	Selected Area Electron Diffraction
SCLC	Space Charge Limited Current
SEM	Scanning Electron Microscopy
Si	Silicon

SiO_2	Silicondioxide
TA-PPE	Poly(*para*-phenylene ethynylene) with thioacetyl end groups
TAS	Transient Absorption Spectroscopy
TEM	Transmission Electron Microscopy
TFE	Trifluoroethylene
TFT	Thin Film Transistor
Tet	Tetraline
Ti	Titanium
UV	Ultraviolet
μ_{FET}	Field effect transistor mobility
$\mu_{FET,Sat}$	Field effect transistor mobility measured in a transistor operating in the saturation regime
$\mu_{FET,Lin}$	Field effect transistor mobility measured in a transistor operating in the linear regime.
μ_L	Longitudinal charge carrier mobility
μ_T	Transversal charge carrier mobility
V_{OC}	Open circuit voltage
VRH	Variable range hopping
V_T	Threshold voltage
WAXD	Wide Angle X-Ray Diffraction
XRD	X-Ray Diffraction
Xyl	Xylene